A Converging Multilens for Refractive X-ray and Neutron Optics

V. A. Churikov

Tomsk State University, Tomsk, Russia
Received April 8, 2003; in final form, June 24, 2003

Abstract—It is suggested to create macroscopic lenses for X-ray and neutron wavelength range ($\lambda = 1$–30 Å) using systems of consistently operating microlenses and correcting microprisms. © *2003 MAIK "Nauka/Interperiodica".*

Previous investigations [1–6] showed the principal possibility to create refractive X-ray optics using component lenses of sufficiently small size (microlenses). If the refractive index of a lens material is $n = 1 + \delta$ (δ being the index increment), the curvature radius R, focal length f, and increment δ of a one-surface microlens are related as $f = R/\delta$. For X-ray radiation, $\delta < 0$ and the converging lens has to be concave.
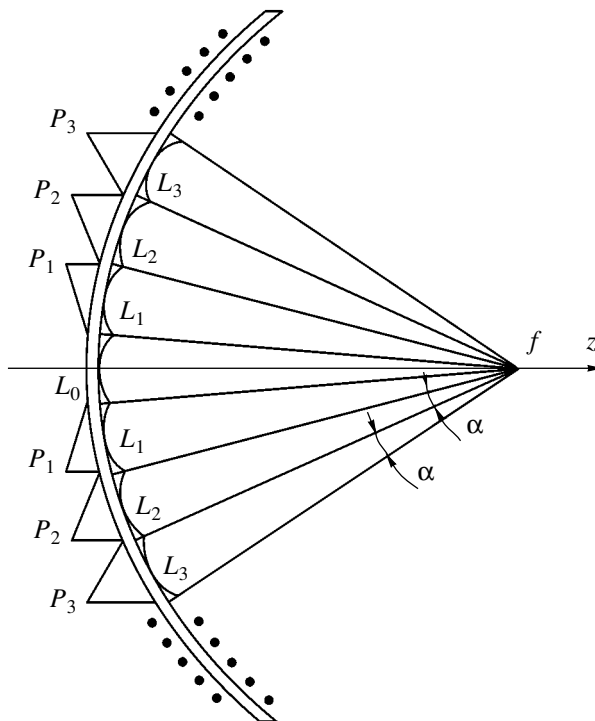
Recently [5, 6], the author suggested to create macroscopic lenses for X-rays by using a system of microlenses with matched focuses and correcting microprisms combined into one lens of required size. This system will be referred to as a multilens and the common focus is called a multifocus.

Multilenses can be created by combining microlenses in various ways. According to one of these (Fig. 1), the central microlens L_0 is perpendicular to the z axis coinciding with the optical axis of the multilens. Thus, the latter optical axis coincides with that of L_0 and passes through its center. The multifocus (f) of the multilens occurs on the optical axis and coincides with the focus of L_0. The circular lens L_1 surrounding the central microlens is tilted by a certain angle so that the rays focused by L_1 would also converge at multifocus f. The optical axes of L_1 form a cone called the focal cone of the circular microlens. The vertex of this cone coincides with multifocus f. Thus, any optical axis of the circular microlens is the generatrix of the focal cone and the symmetry axis of this cone coincides with the optical axis of the multilens.

By the same token, microlens L_1 is surrounded by another microlens, L_2, focusing the rays into multifocus f and so on. In order to ensure that all microlenses would possess a common focus f, it is necessary to tilt generatrices of the focal cones by angles α_n ($n = 1, 2, \dots, N$) relative to the optical axis of the multilens. To this end, the X-ray beam (initially parallel to the optical axis of the multilens) must be split into rays incident onto circular microlenses at various angles α_n. The X-ray beam can be split and deviated by means of cor-

recting microprisms situated on the flat sides of circular microlenses. As a result, all microlenses in the multilens will possess the same focal length (such multilenses will be called equifocal).

Let us find geometric relations for the parameters of a multilens composed of $N + 1$ microlenses with equal curvature radii R and halfwidths ρ (Figs. 1 and 2). The angle between the optical axes of the multilens and the nth microlens is $\alpha_n = \alpha n$, where $n = 0, 1, 2, \dots, N$ and $\alpha = 2\arctan(\rho\delta/R) = 2\arctan(\rho/f)$. The angles γ_n of the correcting prisms, necessary for rotating the initial

Fig. 1. Schematic diagram of a converging multilens composed of microlenses L_i and correcting microprisms P_i (see the text for explanations).

beam so as to provide the normal incidence of radiation onto the flat side of each microlens (Fig. 2), can be readily determined using the law of refraction, $\sin\varphi_1 = n'\sin\varphi_2$, where φ_1 is the angle of incidence onto the nth prism, φ_2 is the angle of refraction in the prism, and n' is the refractive index of the prism material. Assuming that $\varphi_1 = \gamma_n - \alpha n$ and $\varphi_2 = \gamma_n$, we obtain a relation,

$$\gamma_n = \arctan\left\{\frac{\sin(n\alpha)}{1 + \cos(n\alpha) - \delta}\right\},$$

from which it follows that the central microlens does not require a correcting prism because $\gamma_0 = 0$. The width t_n of the asperity BC (Fig. 2) of the nth correcting prism is

$$t_n = 2\rho\frac{\cos(n\alpha)\tan\gamma_n}{\cos(\gamma_n - n\alpha)},$$

and the width P_n of the prism face AB is

$$P_n = 2\rho\frac{\cos(n\alpha)}{\cos(\gamma_n - \alpha n)}.$$

The formation of images in a multilens possessing such a complicated structure is accompanied by various distortions and peculiarities, the number of which is greater than that in simple optical lenses. All these defects can be subdivided into three types:

(i) Defects equally inherent in both optical and X-ray lenses (chromatic and spherical aberrations, distortions, coma, etc.). In multilenses, these aberrations exhibit certain specific features because they arise simultaneously in many microlenses forming a system of ring geometry (e.g., only the central microlens introduces spherical aberrations) and in microprisms introducing their own contributions.

(ii) Defects related to the multilens geometry, deviations from a preset geometry, and inhomogeneity of the material.

(iii) Defects related to the quantum character of interactions between radiation and the multilens materials, which can possess a rather complicated character dependent on the wavelength and the material parameters.

These problems were partly considered in [7], but are worthy of a broader and deeper investigation. Let us analyze some features of multilenses in more detail.

In multilenses of the type under consideration, each circular microlens contains regions not featuring rays transmitted through the microlens. Indeed, the light beam incident onto a correcting prism is split into two rays at the corner (point B): one ray exhibits refraction in the prism, while the other is transmitted along BC without refraction. As a result, each microlens acquires a circular region (called the blind ring) transmitting no

Fig. 2. Schematic diagram of a microlens in combination with a correcting microprism for a converging multilens (see the text for explanations).

light quanta. The width ξ_n of a blind ring in the nth microlens is given by the formula

$$\xi_n = 2\rho\frac{\sin(n\alpha)\sin\gamma_n}{\cos(\gamma_n - \alpha n)}$$

from which it is seen that the central microlens L_0 has no blind ring (for $\gamma_0 = 0$) and that the relative width of a blind ring in the nth microlens, $\Theta_n = \xi_n/2\rho$, increases with the microlens number.

Thus, the presence of blind rings results in splitting of the total radiation flux passing through the multilens into separate fluxes converging at the multifocus. This feature of multilenses will be called mosaicity.

Radiation transmitted through a multilens is concentrated at the multifocus representing, in the ideal case, matched focuses of all individual microlenses. The area of the focus spot S_F^n for radiation passing through the nth microlens in the ideal case is determined by the maximum wavelength λ_M in this flux: $S_F^n \approx 2\pi\lambda_M^2$. In real multilenses, perfect focal matching cannot be achieved and, hence, the above concentration limit is never reached because of unavoidable defects of imaging in microlenses. In practice, the focus of each microlens is smeared to a radius of $r_f^n > \lambda_M$, so that the corresponding focal spot area is greater than S_F^n. Moreover, the focuses of microlenses are usually not matched perfectly (or even fully mismatched) and spread over a certain focusing region F characterizing a given multilens. The extent of the focus spread δ_F over all microlenses is determined by the formula

$$\delta_F = \max\left|\mathbf{f}_n - \mathbf{f}_j\right|,$$

where $\mathbf{f}_n$ and $\mathbf{f}_j$ are the coordinate vectors of the centers of focuses of the nth and jth microlenses, respectively.

Radiation transmitted through the multilens is focused within an area S_F that can be estimated as

$$S_F \approx \frac{\pi}{2}(\delta_F + \bar{r}_f)^2, \quad \bar{r}_f = \frac{1}{N}\sum_{i=0}^{N} r_f^n,$$

where $\bar{r}_f$ is the average focus radius of the component microlenses. The degree of focus spreading δ_F and the average radius $\bar{r}_f$ are determined primarily by deviations from the "ideal" multilens, that is by the manufacturing accuracy that depends on the technological facilities. The linear size of the multilens focus spot can be estimated as proportional to the microlens curvature radius,

$$\delta_F + \bar{r}_f \approx 2R.$$

Now let us consider the X-ray spectral range, in which multilenses are applicable, and estimate the properties of materials required for manufacturing such devices. The upper boundary of a spectral range of the X-ray optics is determined by the ability of X-ray photons to penetrate into a multilens. The maximum wavelength λ_{max} for the effective X-ray refractive optics can be estimated from the dependence of the radiation attenuation coefficient on the wavelength [8]:

$$\mu = \tau + \sigma \approx \frac{\eta N_A}{A}\left(CZ^4\lambda^3 + \frac{8\pi e^4 Z^2}{3m^2 c^2}\right).$$

Here, τ is the absorption coefficient related to a resonance interaction of X-ray photons with core-shell electrons (internal photoeffect) [8]; σ is the scattering coefficient; C is a coefficient dependent on the wavelength λ and the atomic structure parameters (see [8]); Z is the nuclear charge of the element from which the prism or lens is made; η—is the density of the prism; N_A is the Avogadro number; A is the atomic weight; e and m are the electron charge and mass, respectively; and c is the velocity of light.

As can be seen from the above formula, the most favorable materials for refractive X-ray optics are the substances with small nuclear charges, $Z = 3$–6. In particular, $\lambda_{max} \approx 30$ Å for $Z = 3$ (lithium) and $\lambda_{max} \approx 8$ Å for $Z = 6$ (carbon). The lower boundary for the radiation wavelength λ_{min} is determined by the dimensions of atoms (atomic radius r_a), so that $\lambda_{min} \approx r_a \approx 1$ Å. Thus, the spectral range of refractive X-ray optics is 1 Å $\leq l \leq$ 8–30 Å, which corresponds to 12 keV $\geq h\nu \geq 1.5$–0.4 keV on the energy scale. For $Z = 3$–6 and $\lambda = 1$–10 Å, the index increment falls within $10^{-4} \leq \delta \leq 10^{-6}$ and the focal length is on the order of $f = 10^3$–10 cm.

Besides the absorption and scattering losses, any radiation passing through a multilens exhibits losses for reflection and diffraction. Radiation passing from microprisms to microlenses will be partly reflected from face AB (Fig. 2). The angles of radiation incidence (equal to $\angle ABC$) on the correcting microprisms are acute, but always one to two orders of magnitude greater than the critical total reflection angle $\theta_c \approx \sqrt{2\delta}$. Therefore, no total external reflection from microprisms can take place. When the radiation is incident from the microlens side, the reflection coefficient is smaller than that for incidence from the side of a microprism (because the average angle of incidence in the former case is smaller). This asymmetry follows from the geometric asymmetry, which can be called the reflection asymmetry of a multilens. The diffraction losses in a multilens are small because the characteristic dimensions of microprisms and microlenses (close to the microlens curvature radius R) are 2–5 orders of magnitude greater than the radiation wavelength.

The total losses in a multilens can be expressed as

$$I = I_0 K_D K_R \exp(-\mu \bar{l}_{opt}) \approx I_0 K_D K_R (1 - \mu \bar{l}_{opt}),$$

where I_0 and I are the incident and transmitted radiation flux densities, respectively; K_D and K_R are the coefficients of diffraction and reflection losses, respectively; and $\bar{l}_{opt}$ is the average optical pathlength in the multilens. The latter quantity is described by a rather cumbersome expression [6], but it can be approximately estimated via the microlens curvature:

$$\bar{l}_{opt} \approx 2R.$$

The coefficient of radiation amplification by a multilens, k_{ml}, can be expressed via the multilens area S (representing a sum of the microlens areas s_n) and the coefficients of losses:

$$k_{ml} \approx \frac{S}{s_F} K_D K_R \exp(-2\mu R), \quad S = \sum_{i=0}^{N} s_n = 2\pi(nR)^2,$$

$$s_F \approx 2\pi R^2.$$

Here, the diffraction and reflection losses can be ignored in comparison to the absorption and scattering losses, which yields

$$k_{ml} \approx n^2(1 - 2\mu R).$$

For transmitting 1% of the incident radiation, an effective multilens must contain not less than 10 microlenses, but significant radiation concentration is possible only when the number of microlenses is two to three orders of magnitude greater.

The above considerations for X-ray multilenses are generally applicable to the neutron radiation as well, since the refractive indices for X-ray and neutron beams in the wavelength interval 1 Å $\leq \lambda \leq$ 30 Å (cold and thermal neutrons) are close. However, neutrons (in contrast to X-ray photons interacting with electron shells) interact with nuclei. For a neutron radiation in the above wavelength interval, materials are characterized by the index increments $10^{-4} \leq |\delta| \leq 10^{-6}$, which are of the same order of magnitude as those for X-rays. Note that, while $|\delta|$ for X-rays is always negative, the values for neutrons can be either negative or positive, depending on the particular nuclei [9–11]. For $\delta > 0$, the converging microlenses must be convex and the correcting microprisms are oriented in a different manner relative to the optical axis (with asperities *BC* closer to the optical axis). In the wavelength interval under consideration, neutrons are usually absorbed to a lower extent than X-rays. Therefore, multilenses can offer even a more effective solution for neutrons than for X-rays.

Finally, it should be noted that simplified multilenses created using a system of correcting microprisms (without microlenses) are analogous in many respects to the Fresnel lenses for the visible spectral range.

REFERENCES

1. A. Snigirev, V. Kohn, I. Snigireva, *et al.*, Nature **384** (7), 49 (1996).

2. A. Snigirev, V. Kohn, I. Snigireva, *et al.*, Appl. Opt. **37** (4), 653 (1998).

3. P. Elleaume, J. Synchrotron Radiat., No. 5, 1 (1998).

4. Yu. I. Dudchik, N. N. Kol'chevskiĭ, and F. F. Komarov, Pis'ma Zh. Tekh. Fiz. **24** (24), 19 (1998) [Tech. Phys. Lett. **24**, 954 (1998)].

5. V. A. Churikov, in *Proceedings of the Regional Conference for Students, Post-Graduates, and Young Scientists "Siberian School of Young Scientist," Tomsk, 1998* (Tomsk. Ped. Gos. Univ., Tomsk, 1999), Vol. 4: *Physics, Mathematics, Communication Technologies*.

6. V. A. Churikov, *Refracting X-ray Optics*, Available from VINITI, No. 3205-B00 (2000).

7. V. A. Churikov, in *Proceedings of the 7th International Regional Conference for Students, Post-Graduates, and Young Scientists "The 4th Siberian School of Young Scientists," Tomsk, 2001* (Tomsk. Ped. Gos. Univ., Tomsk, 2001), Vol. 4: *Natural and Exact Sciences*, pp. 313–316.

8. M. A. Blokhin, *Physics of X-rays* (GITTL, Moscow, 1957).

9. Yu. A. Alexandrov, *The Fundamental Properties of the Neutron* (Énergiya, Moscow, 1982; Clarendon Press, Oxford, 1992).

10. N. A. Vlasov, *Neutrons* (Nauka, Moscow, 1971).

11. *Physical Quantities. Handbook*, Ed. by I. S. Grigor'ev and E. Z. Meĭlikhov (Énergoatomizdat, Moscow, 1991).

Translated by P. Pozdeev

The Structure and Thermo EMF
of a Nanotubular Carbon Deposit
Formed in Electric Discharge Plasma

I. V. Zolotukhin*, I. M. Golev, E. K. Belonogov, V. P. Ievlev,
D. A. Derzhnev, and A. E. Markova

Voronezh State Technical University, Voronezh, Russia
* e-mail: paul@zolot.vrn.ru
Received May 27, 2003

Abstract—We have studied the structure and thermo emf of a nanotubular carbon deposit formed in electric arc discharge plasma. The deposit contains flocky granules with dimensions of 15–20 μm within a 20–60 μm-thick layer on the substrate surface. This deposit is characterized by a sufficiently high thermo emf (60 μV/K) and electric conductivity (600 Ω^{-1} m^{-1}). © *2003 MAIK "Nauka/Interperiodica".*

Presently, methods of obtaining carbon nanotubes are extensively developed and the properties of these objects are thoroughly studied, which is explained by the good prospects of using such materials in nanoelectronics. An established method for the synthesis of carbon nanotubes is based on the sputtering of graphite in an electric arc plasma. The evaporation of graphite from the anode and subsequent deposition onto the cathode leads to the formation of a deposit containing single- and/or multilayer nanotubes, as well as other carbon derivatives—amorphous carbon, graphite clusters and nanoparticles, fullerenes, etc.—frequently referred to in general as soot.

Here we report the results of investigations of the structure and thermo emf (S) of a carbon deposit obtained in electric arc plasma in the course of optimization of the technology of carbon nanotube formation.

The nanotube-containing deposit was obtained in the course of sputtering of a special purity grade (OSCh-7-3) graphite electrode in an electric arc. The arc discharge was generated in helium at a pressure of 500 Torr, a discharge current density of 65–75 A/cm², and a voltage of 21 V. The deposition time was varied from 180 to 300 s, after which the layer of carbon deposit (1 to 1.5-mm-thick) was separated from the graphite cathode surface. The surface structure of the samples was studied in a REM-300 scanning electron microscope (SEM). The typical SEM image of such a carbon deposit is presented in Fig. 1.

The central region of the deposit with a diameter of 3–5 mm exhibits numerous craters with walls having the form of protuberances [1]. This region is surrounded by the ring with an outer diameter of 10−12 mm composed of flocky formations (granules) with dimensions of 15–20 μm randomly arranged over the substrate surface and found to within a 20–60-μm-

thick surface layer. A peripheral region of the deposit, representing a 1–2-mm-wide ring, exhibits a columnar structure.

Figure 2a shows the general structure of flocky granules. Each granule comprises a disordered frame of filamentlike formations rather strongly connected to one another. The flocky granules were dispersed by ultrasound and examined in a transmission electron microscope (TEM). This study showed that the filamentlike formations have a diameter of 50–60 nm, a
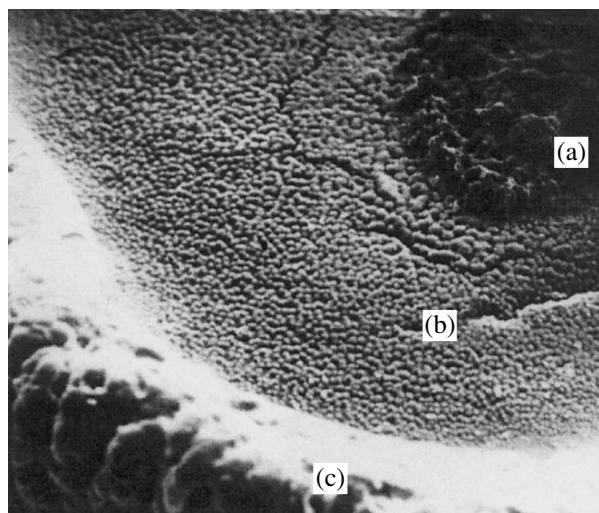
Fig. 1. A SEM image showing the surface structure of a carbon deposit containing carbon nanotubes (magnification, ×110): (a) a central region with the surface resembling "double" rose leaves (S = ~20 μV/K); (b) the region containing randomly arranged flocky granules (S = 55–60 μV/K); (c) a peripheral region of the deposit, possessing a columnar structure (S = 7–8 μV/K).

Fig. 3. The plots of (*1*) thermo emf *S* and (*2*) specific conductivity σ versus depth *x* of probe penetration into a flocculent structure of granules of the nanotubular carbon deposit.

Fig. 2. TEM images illustrating (a) the structure of flocky granules formed by the bundles of carbon nanotubes (×2400); (b) the bundles of carbon nanotubes (×30000); (c) a bundle of carbon nanotubes coated with amorphous carbon (×600000).

length of 0.5–2 μm, and are covered by a 20–30-nm-thick layer of amorphous carbon (Fig. 2b). Each filament contains 100–150 multilayer carbon nanotubes with a diameter of 2.5–4 nm, aligned parallel to the filament axis (Fig. 2c).

Figure 1 presents a map of thermo emf in various regions of the carbon deposit. The differential thermo emf (*S*) was measured using a method described previously [2]. All the *S* values were negative, the absolute value amounting to ~20 μV/K in the central region, reaching maximum values in the region of flocky granules (*S* ~ 55–60 μV/K), and decreasing to 7–8 μV/K in the peripheral region of the deposit.

Let us consider in more detail the structure of flocky granules characterized by the maximum values of *S*. In

this region, the thermo emf and specific conductivity were measured using a silver wire microprobe with a diameter of 0.3 mm. Possessing a flat edge and insulated side surface, the probe allowed the necessary temperature gradient to be created in the sample. The probe was indented into the sample and positioned to within $x = \pm 1$ μm using a special micrometric drive mechanism. The conductivity was estimated by the formula

$$\sigma = \frac{1}{R}\frac{\Delta x}{A}, \tag{1}$$

where *R* is the measured value of resistance, *A* is the probe edge surface area, and Δx is a distance between the probe and the base contact.

Figure 3 (curve *1*) shows a plot of *S* versus depth *x* of the hot probe edge surface indented into the flocculent carbon deposit. The initial contact between the probe and the surface of flocky granules (*x* = 0) gives *S* = 10 μV/K, the maximum (*S* ≈ 60 μV/K) being reached at a depth of *x* = 10 μm. Within a layer of *x* = 10–30 μm, the thermo emf is retained on a level of *S* ≈ 58 μV/K. Curve *2* in Fig. 3 shows variation of the specific conductivity σ(*x*) with the depth of probe indentation into the flocculent structure. This curve also exhibits a plateau on an average level of σ ≈ 500 Ω^{-1} m^{-1}. Penetrating down to a depth greater than 50 μm, the probe reaches the substrate characterized by *S* ≈ 27–35 μV/K and σ ≈ 2000 Ω^{-1} m^{-1}. With allowance of the substrate resistance, a specific conductivity of the flocculent structure amounts to 600 Ω^{-1} m^{-1}, being of the same order of magnitude as the conductivity reported for 7–17-μm-thick slabs of carbon nanotubes [3]. The results of *S* and σ measurements during withdrawal of the probe repeat the same profiles with a small hysteresis in *x*. These results indicate that the flocculent structure is quite rigid, admits elastic contraction, and exhib-

its almost complete restoration of the initial shape upon unloading.

The flocky formations comprising the bundles of carbon nanotubes are similar to the flocky coils of colloidal aggregates formed in various organic and inorganic materials, which are known to possess a fractal internal structure [4]. The fractal dimensions D of such structures falls within $D = 2.4$–2.7. The fractal structures of this type are characterized by high values of the specific internal surface area determined as

$$A = a\left(\frac{R}{r_0}\right)^D, \qquad (2)$$

where a is the surface area of a unit element (of which the fractal structure is composed), R is the radius of a flocky fractal coil, and r_0 is the radius of the unit element. In our case, the unit element is represented by a 1-μm-long bundle containing 100–120 nanotubes with a diameter of $r_0 = 0.05$ μm. Simple calculations for $D = 2.5$ show that 1 cm^3 of such flocky fractal coils composed of the bundles of carbon nanotubes has a surface area on the order of $(5$–$9) \times 10^2$ m^2 formed by the nanotube interfaces.

Once the fractal dimension is known, we can also estimate the average density of a flocky coil using the well-known relation [5]

$$\rho = \rho_0\left(\frac{r_0}{R}\right)^{3-D}. \qquad (3)$$

Assuming $\rho_0 = 2.2$ g/cm^3, $r_0 = 5 \times 10^{-6}$ cm, and $R = 10^{-3}$ cm, we obtain $\rho = 0.16$ g/cm^3. Such densities are characteristic of aerogels—porous media with hard frameworks formed by oxide molecules such as SiO_2, Al_2O_3, ZrO_2, etc.

In conclusion, the sputtering of a graphite anode in an electric arc discharge plasma is accompanied by the formation of a carbon deposit containing flocky granules with a rigid framework of the bundles of carbon nanotubes possessing a fractal structure. These flocky fractal coils form a multifractal structure characterized by sufficiently high thermo emf (S) and conductivity (σ) values, which can be considered to be a promising thermoelectric material.

REFERENCES

1. Yu. S. Grushko, V. M. Egorov, I. M. Zimkin, *et al.*, Fiz. Tverd. Tela (St. Petersburg) **37**, 1838 (1995) [Phys. Solid State **37**, 1001 (1995)].

2. I. V. Zolotukhin, I. M. Golev, A. A. Popov, and V. P. Ievlev, Pis'ma Zh. Tekh. Fiz. **28** (16), 32 (2002) [Tech. Phys. Lett. **28**, 678 (2002)].

3. Y. J. Yosida, Phys. Chem. Solids **60**, 1 (1999).

4. A. J. Marangoni, Phys. Rev. B **62**, 13951 (2000).

5. B. M. Smirnov, Usp. Fiz. Nauk **152**, 133 (1987) [Sov. Phys. Usp. **30**, 420 (1987)].

Translated by P. Pozdeev

The Optimum Characteristics of a Halogen Lamp Pumped by Transverse RF Discharge

A. K. Shuaibov, A. I. Dashchenko, I. V. Shevera*, and A. A. General

Uzhgorod National University, Uzhgorod, Ukraine
* e-mail: ishev@univ.uzhgorod.ua
Received June 2, 2003

Abstract—We report on the optimized characteristics of a small-size bactericidal lamp pumped by transverse RF (f = 1.76 MHz) discharge, operating on a system of the molecular emission bands of chlorine in a wavelength range of 195–310 nm. The spectral characteristics of the plasma emission were measured and the intensity of chlorine emission bands were studied as functions of the total pressure and partial composition of a helium–chlorine mixture. Oscillograms of the pumping current and output radiation intensity were measured and the total output radiation power was determined. It is established that the lamp radiates predominantly in a bactericidal wavelength interval on an electron-vibrational transition at 200 nm in Cl_2^{**} molecules. The optimum partial pressures of helium and chlorine are 100–300 and 90–120 Pa, respectively. The maximum output power of UV emission from the side cylindrical surface of the lamp reached 10 W. The lamp can be used in photochemistry, ecology, genetics, and medicine. © *2003 MAIK "Nauka/Interperiodica"*.

Powerful and highly effective sources of spontaneous radiation in the ultraviolet (UV) and vacuum ultraviolet (VUV) spectral range, operating on the electron-vibrational transitions in inert gas monohalides and halogen dimers, are widely used in microelectronics, high-energy chemistry, and medicine [1]. Simple bactericidal lamps with relatively inexpensive working media (not employing krypton and xenon) can be created using mixtures of light inert gases with chlorine molecules. Indeed, use of the highly reactive fluorine-containing media increases requirements to the materials for electrodes and discharge tube. On the other hand, gas mixtures based on iodine and bromine, while being less aggressive, tend to concentrate on the internal surface of the output aperture. At a certain concentration of iodine and bromine vapors in the discharge tube, this can reduce the output emission power because of excess UV–VUV absorption in the layer containing halogen molecules. As for the inert gas, the heat capacity of neon is significantly higher than that of helium and, hence, the latter is preferred in the lamps with air (natural or forced) cooling.

Previously, we have established that He–Cl lamps pumped with a longitudinal dc glow discharge [2] and confined discharge [3] are characterized by the emission spectrum expanded toward shorter wavelength (due to the emission at 200 nm [Cl_2^{**}]) and continuously covering the wavelength interval of 195–270 nm. For increasing the discharge stability in electronegative media, we have used a transverse RF discharge to form a plasma medium in an excimer–halogen lamp with a planar aperture [4].

Below we report the results of investigation and optimization of the working characteristics of a lamp employing longitudinal RF discharge in a helium–chlorine gas mixture.

A longitudinal RF discharge of the γ type was generated in a cylindrical quartz discharge tube with an inner diameter of 1.4 cm and an anode–cathode distance of 3 cm. The lamp employed a system of hollow nickel sheet electrodes with a length of 1.5 cm and a diameter of 1.4 cm. The discharge was initiated by an amplitude-modulated (modulation frequency, $f \leq$ 50 Hz) RF voltage (pumping frequency, F = 1.76 MHz) generator of the EN-57M type with an average power not exceeding 250 W. The voltage was applied to the electrodes via a decoupling capacitor (C_0 = 200 pF). The RF voltage amplitude reached 5–6 kV. The discharge tube with open ends was mounted in a 10-liter buffer chamber. In the regime of slow circulation of the working medium, a He–Cl_2 mixture was pumped through the buffer chamber with the discharge tube at a flow rate of 0.1–0.3 l/min. The method and instrumentation used for the measurement of emission characteristics of the discharge plasma were described elsewhere [5, 6].

Figure 1 shows the most typical spectrum of emission from the plasma of a longitudinal RF discharge in a He–Cl_2 gas mixture (the spectrum is normalized to a relative sensitivity of the monochromator and photomultiplier). As can be seen, the main emission is concentrated within the emission bands at 200 nm [Cl_2^{**}] and 257 nm [$Cl_2(D' - A')$], covering the spectral interval

I/k_λ, a.u.
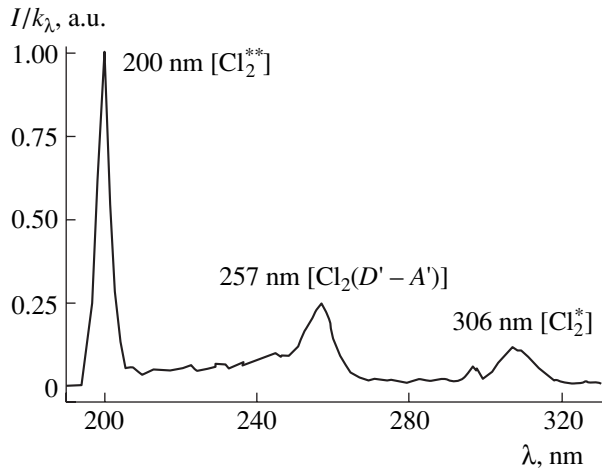
Fig. 1. The typical spectrum of UV emission from the plasma of a longitudinal RF discharge in a He–Cl$_2$ mixture with $P(\text{He})/P(\text{Cl}_2) = 160/40$ Pa.

P_{rad}, a.u.
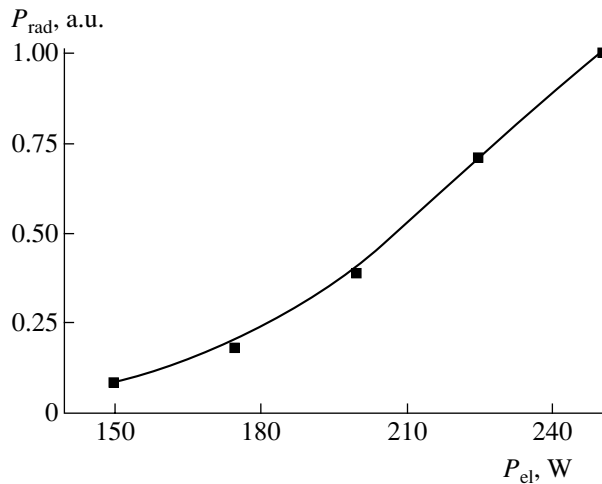
Fig. 2. A plot of the total output power versus pumping power for UV emission from the plasma of a longitudinal RF discharge in a He–Cl$_2$ mixture with $P(\text{He})/P(\text{Cl}_2) = 160/40$ Pa.

from 195 to 260 nm. The emission in the band at 306 nm [Cl$_2^*$] was relatively less intense.

We have studied the intensity of emission in the molecular bands of chlorine as a function of the total pressure and partial composition of a helium–chlorine mixture. It was found that the maximum UV emission power is reached for the partial pressures of helium and

chlorine within 250–300 and 80–100 Pa intervals, respectively. The intensity of emission at 306 nm [Cl$_2^*$] was least sensitive to variations in the chlorine pressure $P(\text{Cl}_2)$.

Figure 2 shows the total output power of UV emission from the plasma of a longitudinal RF discharge in a He–Cl$_2$ mixture as a function of the pumping source power. The RF initiation threshold corresponds to a source power of 150 W. As the pumping power is increased from 180 to 250 W, the total output power of UV emission from the entire working aperture also exhibits a linear growth. The absolute total UV power maximum reached 10 W.

Thus, we have studied the characteristics of optical emission from the plasma of a longitudinal RF discharge in a He–Cl$_2$ mixture at medium pressures and demonstrated that this system offers a source of bactericidal radiation concentrated predominantly within the [Cl$_2^{**}$] emission band at 200 nm. The optimum partial pressures of helium and chlorine are within 100–300 and 90–120 Pa, respectively. The average UV output power of UV emission is ≤10 W. The discharge can be employed in small-size bactericidal lamps, with good prospects for applications in photochemistry, biotechnology, and medicine.

REFERENCES

1. M. I. Lomaev, V. S. Skakun, É. A. Sosnin, *et al.*, Usp. Fiz. Nauk **171**, 201 (2003).

2. A. K. Shuaibov, A. I. Dashchenko, and I. V. Shevera, Teplofiz. Vys. Temp. **39**, 833 (2001).

3. A. K. Shuaibov, A. I. Dashchenko, and I. V. Shevera, Pis'ma Zh. Tekh. Fiz. **28** (6), 23 (2002) [Tech. Phys. Lett. **28**, 226 (2002)].

4. A. K. Shuaibov, L. Shimon, A. Dashchenko, and I. Shevera, in *Proceedings of the 3rd International Young Scientists Conference "Problems of Optics and High Technology Material Science SPO-2002"* (Kiev, 2002), DP 6, p. 219.

5. A. K. Shuaibov, L. L. Shimon, A. I. Dashchenko, and I. V. Shevera, Prib. Tekh. Éksp., No. 1, 104 (2002).

6. A. Shuaibov, L. Shimon, A. Dashenko, and I. Shevera, Proc. SPIE **4747**, 409 (2002).

7. A. K. Shuaibov, A. I. Dashchenko, and I. V. Shevera, Zh. Tekh. Fiz. **72** (4), 32 (2002) [Tech. Phys. **47**, 406 (2002)].

Translated by P. Pozdeev

The Nature of Particles Yielded during Electron-Stimulated Desorption of Samarium from Oxidized Tungsten Surface

V. N. Ageev and Yu. A. Kuznetsov*

Ioffe Physicotechnical Institute, Russian Academy of Sciences, St. Petersburg, 194021 Russia
* e-mail: kuznets@ms.ioffe.rssi.ru
Received June 30, 2003

Abstract—It is established for the first time that the yield resonances related to excitation of the core electron levels of samarium (Sm) and tungsten (W) during the electron-stimulated desorption of samarium from the surface of oxidized tungsten represent neutral particles differing in the chemical nature. Most probably, the excitation of samarium levels leads to desorption of Sm atoms, while the excitation of tungsten levels causes desorption of SmO molecules. © *2003 MAIK "Nauka/Interperiodica"*.

Our previous investigations [1–4] showed that the yield of neutral particles during electron-stimulated desorption (ESD) of europium (Eu) and samarium (Sm) layers adsorbed on the surface of oxidized tungsten (W) exhibit a resonance character depending on the energy of bombarding electrons. The positions of peaks in the ESD yield is well correlated to the energies of excitation of the $5p$ and $5s$ core electron levels of Eu, Sm, or W. The intensities of the ESD peaks arising during excitation of the core levels of rare-earth metal (REM) atoms and W, studied as functions of the substrate temperature and the REM coverage, exhibit qualitatively different behavior indicative of a dissimilar chemical nature of these peaks [5, 6].

The fluxes of desorbed neutrals in the aforementioned experiments were monitored using detectors of the surface ionization (SI) type with an emitter representing a heated tungsten ribbon. This technique is not capable of separating the yield of Eu and Sm atoms from that of EuO and SmO species. It was suggested that ESD peaks related to the excitation of REM levels represent Eu and Sm atoms, while the peaks related to excitation of the core levels of tungsten are due to the desorption of EuO and SmO molecules. This assumption agrees with the results of calculations performed with allowance of the fact that the rate of dissociation of EuO molecules is greater than the rate of thermodesorption of Eu$^+$ ions from a heated surface of tungsten [7]. In addition, this hypothesis eliminates difficulties encountered in attempts to explain the excitation transfer from W to Sm via an intermediate oxygen atom.

This study was aimed at demonstrating that the excitation of Sm and W atoms in the course of ESD of a samarium film adsorbed on oxidized tungsten leads to the desorption of neutral particles differing in their chemical nature. To solve this task, it was necessary to reduce the rate of dissociation of SmO molecules on the emitter of the SI detector. This is usually achieved by depositing a nonmetal film onto the metal emitter surface. For example, the rate of dissociation of CsCl molecules on an Ir(111) single crystal face decreased by a factor of 10^6 when this surface was covered with a graphite film [8]. Our choice of emitter for the SI detector—a tungsten ribbon covered with a monolayer of oxygen—was explained by the following reasons:

(i) a monolayer of oxygen adsorbed on tungsten is thermally stable at temperatures up to $T \sim 2000$ K [9];

(ii) the electron work function of an oxygen-covered tungsten surface is 0.75 eV higher than that of a clean tungsten surface [10];

(iii) the probability of further oxidation reactions involving SmO molecules on a W–O surface is very low. These factors gave us hope to obtain a current of nondissociated SmO molecules in the SI detector.

The current of surface-ionized particles generated during the ESD of samarium adsorbed on the surface of oxidized tungsten was measured in a setup described in detail elsewhere [11]. In this system, intended for the investigation of yields and energy distributions of neutrals during ESD, the SI detector had an emitter in the form of a tungsten ribbon with the dimensions $70 \times 2 \times 0.01$ mm. The emitter temperature was determined with the aid of an optical micropyrometer. A monolayer oxygen coverage on the emitter was obtained by exposure to oxygen at a pressure of 10^{-6} Torr and a temperature of 1600 K for 300 s [9].

The target substrates were textured tungsten ribbons with (100)W crystal face predominantly emerging at the surface, which were preliminarily cleaned and then oxidized to various degrees. Samarium was deposited onto the oxidized substrate surface at $T = 300$ K from a straight-channel evaporator representing a tantalum

i, a.u.
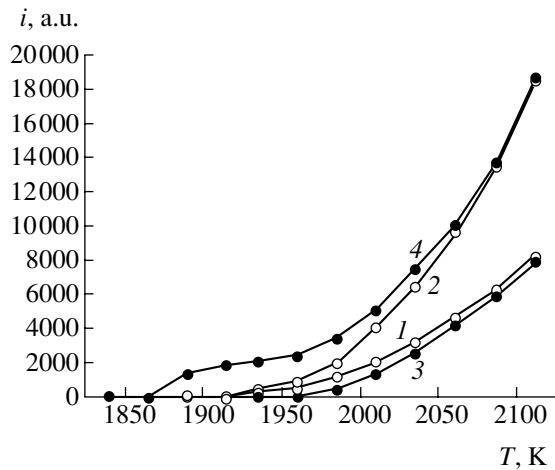
Plots of the SI detector current versus emitter temperature for a tungsten emitter (*1, 2*) without and (*3, 4*) with a monolayer coverage of oxygen. The emitter produces surface ionization of the particles desorbed from a samarium layer on oxidized tungsten surface during ESD at an electron energy of $E_e = 34$ eV (*1, 3*) and 42 eV (*2, 4*). The surface coverage of samarium is $\theta = 0.10$ (*1, 3*) and 1.0 (*2, 4*).

tube charged with metallic samarium prior to evacuation of the setup. The tube, placed near a substrate and oriented along the ribbon, had several output holes ensuring homogeneous distribution of the flux of Sm atoms over the substrate surface. The electron emitter was a tungsten filament oriented parallel to the substrate ribbon and producing a total current of $\sim 5 \times 10^{-6}$ A. The flux of desorbed Sm atoms was generated at an electron energy of ~ 34 eV, while the flux of (supposedly) SmO molecules was observed at an electron energy of ~ 42 eV. These electron energy values are given with a correction for the electron work function of the emitter [12]. The pressure of residual gases in the setup was below 10^{-10} Torr.

The results of the ESD measurements presented in the figure show the temperature dependences of the SI detector current obtained with a tungsten emitter uncovered (curves *1* and *2*) and covered (curves *3* and *4*) with a monolayer of oxygen. In these experiments, the detector monitored the fluxes of particles formed during ESD at an electron energy of $E_e = 34$ eV (curves *1* and *3*) from a samarium layer adsorbed on tungsten oxidized to an oxygen coverage of $\theta = 0.10$ and at $E_e = 42$ eV (curves *2* and *4*) from a layer adsorbed on tungsten oxidized to $\theta = 1.0$. Thus, curves *1* and *3* correspond to excitation of the Sm $5p$ core electron level, while curves *2* and *4* correspond to excitation of the W $5p$ level.

As can be seen from data obtained with the uncovered tungsten emitter (curves *1* and *2*), the surface ionization current due to excitation of the Sm $5p$ core electron level is lower than that related to the W $5p$ level. However, the shapes of the temperature dependence of the SI detector current in these cases are similar, exhib-

iting the same temperature threshold followed by exponential growth of the current with the temperature. Therefore, the surface ionization current from the uncovered tungsten emitter represents particles of the same chemical nature despite the fact that the ESD is initiated by the electrons of different energies.

A different pattern was observed for the SI detector with a tungsten emitter covered with a monolayer of oxygen (see figure, curves *3* and *4*). Here, a threshold temperature for the appearance of the surface ionization current upon excitation of the Sm $5p$ electron level (curve *3*) is greater as compared to that for the uncovered tungsten emitter (curve *1*), but, as the temperature increases, curve *3* asymptotically approaches curve *1*. At the same time, the current due to excitation of the W $5p$ electron level (curve *4*) appears at a much lower threshold temperature as compared to that for the uncovered emitter (curve *2*). Moreover, the shape of the temperature dependence of the current for the SI detector with the oxygen-covered emitter (curve *4*) significantly differs from the exponential curve observed with the oxygen-free emitter (curve *2*). In curve *4*, the current first rapidly grows with the temperature *T*, exhibits a plateau, and eventually asymptotically approaches curve *2*.

The different behavior of the temperature dependences of currents in the oxygen-covered SI detector observed during ESD with the excitation of Sm $5p$ and W $5p$ core electron levels is evidence of the dissimilar nature of the particles formed in the two cases. It was reasonable to suggest that particles desorbed upon excitation of the Sm $5p$ level are Sm atoms and their current of surface ionization on tungsten (see figure, curve *1*) obeys the Saha–Langmuir formula [13]. Then, an increase in the threshold temperature observed for the emitter with a monolayer oxygen coverage (curve *3*) indicates that this oxygen monolayer, while increasing the electron work function of the metal surface, hinders the establishment of a charge equilibrium between samarium and tungsten. The appearance of the SI detector current probably corresponds to the onset of oxygen evaporation from tungsten as a result of samarium oxidation.

On the other hand, we may suggest that particles related to the excitation of the W $5p$ level are SmO molecules. The presence of an oxygen monolayer on the tungsten surface hinders dissociation of SmO molecules and increases the electron work function of this surface. Since the ionization potential of SmO molecules is ~ 0.1 eV higher than that of Sm atoms [14], the temperature threshold for the appearance of SmO$^+$ ions is ~ 100 K lower than a threshold for the appearance of Sm$^+$ ions. When the temperature grows, SmO molecules begin to dissociate and the yield of SmO$^+$ ions exhibits a maximum that is frequently observed for the surface ionization of molecules [15].

The shape of the temperature dependence of the SI detector current observed with the oxygen-free emitter

(see figure, curves *1* and *2*) confirms the assumption that SmO molecules dissociate on the tungsten surface fasted than Sm$^+$ ions desorb from this surface [3]. The mutual arrangement of these curves indicates that SmO molecules predominate over Sm atoms in the ESD yield from a samarium layer adsorbed on the oxidized tungsten surface.

Thus, we have demonstrated that electron bombardment of a layer of samarium adsorbed on oxidized tungsten leads to the desorption of Sm atoms, related to excitation of the Sm 5*p* core electron level, and of SmO molecules due to excitation of the W 5*p* level.

REFERENCES

1. V. N. Ageev and Yu. A. Kuznetsov, Pis'ma Zh. Tekh. Fiz. **26** (13), 86 (2000) [Tech. Phys. Lett. **26**, 579 (2000)].

2. V. N. Ageev, Yu. A. Kuznetsov, and T. E. Madey, J. Vac. Sci. Technol. A **19**, 1481 (2001).

3. V. N. Ageev, Yu. A. Kuznetsov, and N. D. Potekhina, Fiz. Tverd. Tela (St. Petersburg) **45** (5), 157 (2003) [Phys. Solid State **45**, 976 (2003)].

4. V. N. Ageev, Yu. A. Kuznetsov, and T. E. Madey, Surf. Sci. **528** (1–3), 47 (2003).

5. V. N. Ageev and Yu. A. Kuznetsov, Fiz. Tverd. Tela (St. Petersburg) **44**, 1121 (2002) [Phys. Solid State **44**, 1171 (2002)].

6. V. N. Ageev, Yu. A. Kuznetsov, and T. E. Madey, J. Electron Spectrosc. Relat. Phenom. **128** (2–3), 223 (2003).

7. V. N. Ageev, Yu. A. Kuznetsov, and N. D. Potekhina, Fiz. Tverd. Tela (St. Petersburg) **43**, 1894 (2001) [Phys. Solid State **43**, 1972 (2001)].

8. E. Ya. Zandberg, A. Ya. Tontegode, and F. K. Yusifov, Zh. Tekh. Fiz. **41**, 2420 (1971) [Sov. Phys. Tech. Phys. **16**, 1920 (1971)].

9. V. N. Ageev and N. I. Ionov, Fiz. Tverd. Tela (Leningrad) **11**, 3200 (1969) [Sov. Phys. Solid State **11**, 2593 (1969)].

10. V. A. Ishchuk, Candidate's Dissertation (Inst. Fiz. Akad. Nauk USSR, Kiev, 1971).

11. V. N. Ageev, O. P. Burmistrova, and Yu. A. Kuznetsov, Fiz. Tverd. Tela (Leningrad) **29**, 1740 (1987) [Sov. Phys. Solid State **29**, 1000 (1987)].

12. M. L. Knotek, Springer Ser. Chem. Phys. **24**, 139 (1983).

13. E. Ya. Zandberg and N. I. Ionov, *Surface Ionization* (Nauka, Moscow, 1969).

14. R. D. Levin and S. G. Lias, Natl. Stand. Ref. Data Ser. **71**, 526 (1982).

15. N. M. Blashenkov, N. I. Ionov, and G. Ya. Lavrent'ev, Pis'ma Zh. Tekh. Fiz. **13**, 392 (1987) [Sov. Tech. Phys. Lett. **13**, 160 (1987)].

Translated by P. Pozdeev

An Exact Analytical Solution of the Inverse Problem for a Plasma Cylinder Expanding in a Compressible Medium

V. S. Krutikov

Institute of Pulsed Processes and Technologies, National Academy of Sciences of Ukraine, Kiev, Ukraine
Revised manuscript received June 10, 2003

Abstract—A strict analytical solution of the wave equation with cylindrical symmetry in a region with mobile boundaries was obtained by the method of inverse problems with allowance for the interaction of nonlinear arguments. The proposed method is universal and applicable to solving both inverse and direct problems for arbitrary values of the initial radius and displacements. The solution describes the near wave field of an expanding plasma piston, including the field formed in the initial moments of a pulsed expansion process. The solution gives exact values of a given pressure and velocity wave profile at a fixed point of the wave zone in the initial moment, as well as particular finite values of the pressure and velocity at a mobile boundary of the expanding plasma piston at the moments of time approaching zero. The solution is obtained with allowance for additional nonlinear conditions. © 2003 MAIK "Nauka/Interperiodica".

In modeling the breakdown of an interelectrode gap (which presents an independent complicated problem) and numerically realizing the expansion of a plasma cylinder, it is usually assumed that the plasma channel with a radius r_0 and a temperature T_0 already exists at the initial time instant. The initial r_0 and T_0 values are selected within certain intervals, based on the experimental data available for the pulsed processes in air [1–3] and in water [4, 5]. Variation of the initial conditions within the range of their values determined experimentally produces no significant changes in the results of calculations. The corresponding solutions rapidly attain close regimes.

It should be noted that this approach rules out the possibility of considering changes in the functions of pressure, particle velocities, etc., within the very first moments of the process. However, with this stage missing, it is hardly possible to understand and model the breakdown development in an interelectrode gap, as well as many other physical processes involved in the pre- and post-breakdown stages.

This paper presents an attempt to estimate the kinematic and dynamic parameters for the development of expanding cylindrical plasma piston in a compressible medium, including the very first moments of the pulsed process.

Previously [6, 7], analytical solutions of the wave equation were obtained for the regions with mobile boundaries in the general case. For an additional condition set at a given point r_1 of the wave zone in the class of Bessel's functions (in images), exact analytical solutions obtained for the inverse problems exhibited singularities at the point r_1 of the wave zone and on the mobile boundary at $t \longrightarrow 0$. Obtaining exact analytical solutions for the wave problems with mobile bound-

aries of cylindrical symmetry encounters extremely large difficulties, which previously led to the need of using approximate methods for finding the values of indeterminate forms [8, 9]. An attempt to find an exact analytical solution of these problems is presented below.

The wave equation with cylindrical symmetry can be written as follows,

$$\varphi_{tt} - a^2 \varphi_{rr} - a^2 r^{-1} \varphi_r = 0, \tag{1}$$

where φ is the velocity potential, r is the coordinate, t is the time, and a is the velocity of the perturbation propagation in the initially unperturbed liquid medium. Considering zero initial conditions and applying unilateral Laplace's transformation, we obtain the operator equation

$$r\overline{\varphi}_{rr}(r, s) + \overline{\varphi}_r(r, s) - \frac{s^2}{a^2} r\overline{\varphi}(r, s) = 0. \tag{2}$$

Substituting $x = \dfrac{s}{a} r$, we arrive at

$$\Phi_{xx} + \frac{1}{x}\Phi_x - \Phi = 0.$$

A solution of this equation is

$$\Phi = C_1 I_0\!\left(\frac{s}{a}r\right) + C_2 K_0\!\left(\frac{s}{a}r\right), \tag{3}$$

where I_0, K_0, and K_1 are the modified Bessel's functions. For an infinite medium, we have $C_1 = 0$. Taking into account that the functions under consideration have to be finite at $r \longrightarrow \infty$, we obtain in the case when

an arbitrary law of the pressure variation $P = f(r_1, t)$ is set (in images) at a fixed point r_1 of the wave zone (i.e., the inverse problem is solved) [4],

$$\bar{\varphi} = -\frac{\bar{f}(r_1, s) K_0(\mu, r)}{s \rho K_0(\mu, r_1)}, \quad \bar{\varphi}_r = \frac{\bar{f}(r_1, s) K_1(\mu, r)}{a \rho K_0(\mu, r_1)},$$

$$s\bar{\varphi} = -\frac{\bar{f}(r_1, s) K_0(\mu, r)}{\rho K_0(\mu, r_1)}, \tag{4}$$

where $\mu = s/a$, s is the Laplace transformation parameter, ρ is the density of the medium, $P = -\rho \varphi_t$, and $v = -\varphi_r$. The passage to originals (inverse transformation) in Eqs. (4) in each particular case can be performed in a rational way depending on the form of function f.

For the pressure function $P(r_1, t)$ set at in the class of Bessel's functions, we have to take into account two circumstances: first, the existence of an initial radius r_0 (the time when the wave appears at r_1 will depend on r_0), and second, the finiteness of the pressure and velocity functions (these quantities have to be finite at any time moment). Then, the additional condition for the inverse problem is as follows:

$$P(r_1, t) = \frac{A}{\sqrt{\left(t + \alpha + \dfrac{r_0}{a}\right)^2 - \dfrac{r_1^2}{a^2}}}.$$

Omitting transformations (generally analogous to those presented in [7]), we eventually arrive at the formulas describing the functions studied at any point:

$$P(r, t) = \frac{A}{\omega}, \quad v(r, t) = \frac{A(t + \beta)}{r \rho \omega},$$

$$\omega = \sqrt{(t + \beta)^2 - \frac{r^2}{a^2}}. \tag{5}$$

For the mobile boundary, we obtain

$$P(R(t), t) = \frac{A}{\omega} - \frac{1}{2} \rho v^2(R(t), t),$$

$$v(R(t), t) = \frac{A(t + \beta)}{R(t) \rho \omega}, \tag{6}$$

$$R(t) = \left\{ r_0^2 + \frac{2A}{\rho}[\omega - \omega_1] \right.$$

$$\left. + \frac{2A^2}{\rho^2 a^2} \left[\ln\left| \omega - \frac{A}{\rho a^2} \right| - \ln\left| \omega_1 - \frac{A}{a^2 \rho} \right| \right] \right\}^{1/2}, \tag{7}$$

where

$$\omega = \sqrt{(t + \beta)^2 - \frac{R^2(t)}{a^2}}, \quad \omega_1 = \sqrt{\beta^2 - \frac{r_0^2}{a^2}},$$

$$\beta = \alpha + \frac{r_0}{a}, \quad A, a, \rho, r_0, \alpha = \text{const.}$$

In particular, for $t \longrightarrow 0$,

$$P(R(t), t) = \frac{A}{\sqrt{\left(\alpha + \dfrac{r_0}{a}\right)^2 - \dfrac{r_0^2}{a^2}}} - \frac{1}{2} \rho v^2(R(t), t), \tag{8}$$

$$v(R(t), t) = \frac{A\left(\alpha + \dfrac{r_0}{a}\right)}{r_0 \rho \sqrt{\left(\alpha + \dfrac{r_0}{a}\right)^2 - \dfrac{r_0^2}{a^2}}}, \tag{9}$$

and for $a \longrightarrow \infty$,

$$R(t) = \sqrt{r_0^2 + \frac{2At}{\rho}}. \tag{10}$$

Note that, for $\alpha, r_0 \longrightarrow 0$, formulas (5)–(10) transform into expressions obtained previously [7]. The calculation of $R(t)$ can be performed as in [7, 11], a good approximation for $a \longrightarrow \infty$ being offered by formula (10).

The above exact analytical solutions of the inverse and direct problems give exact profiles of the pressure P and velocity v at a fixed point r_1 of the wave zone at the moment of appearance, as well as particular finite values of $P(R(t), t)$ and $v(R(t), t)$ on the mobile boundary of the plasma piston at $t \longrightarrow 0$ at the very beginning of the process. In the case of arbitrary laws of variation of the plasma piston boundary velocity v and the pressure $P = f(r_1, t)$, the solutions are presented in [6, 7].

Equation (7) clearly demonstrates an essentially nonlinear character of the relationship between the law of variation of the mobile boundary radius and the functions under consideration. In the general case [7], this relationship can be exactly determined only by solving inverse problems with allowance for the interaction of nonlinear arguments [11].

Nonlinear additional conditions of the type

$$P(r_1, t) = -\rho\left(\varphi_t + \frac{1}{2}\varphi_r^2\right) \tag{11}$$

are used in cases when it is necessary, for example, to provide for a preset form of the pressure function near or on a moving surface. The velocities of particles in the

$P(r_1, t)/P_0$
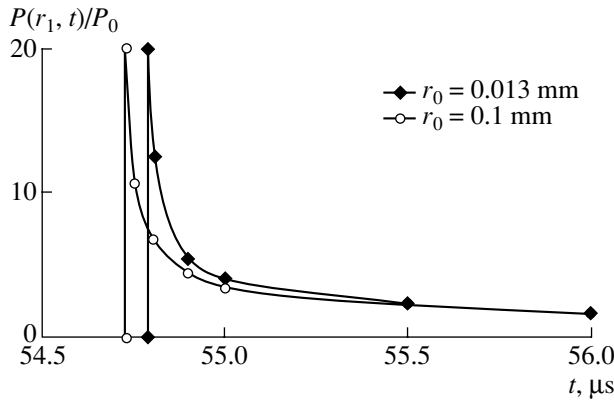
Fig. 1. Initial data used for reconstructing the pressure kinetics at a given point in the wave zone for two values of the initial radius.

$R(t)$, mm
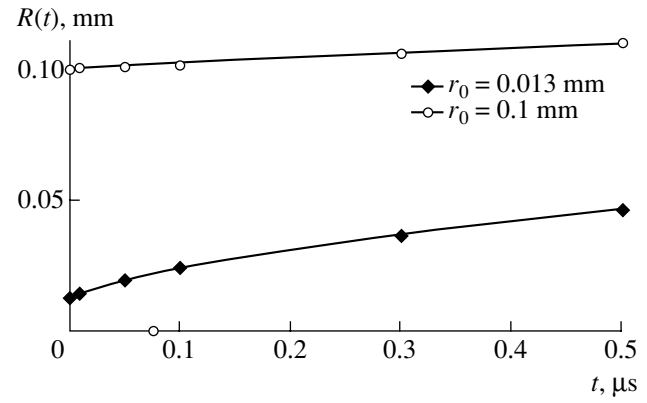
Fig. 2. Reconstructed time variation of the radius of the expanding plasma piston boundary for two values of the initial radius.

$v(R(t), t)$, m/s
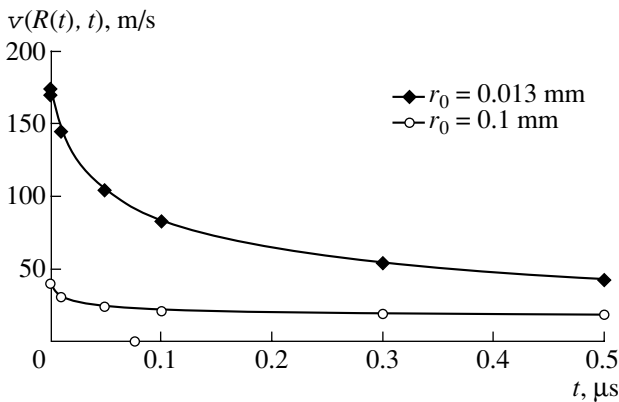
Fig. 3. Reconstructed time variation of the velocity of a mobile plasma boundary for two values of the initial radius.

$P(R(t), t)/P_0$
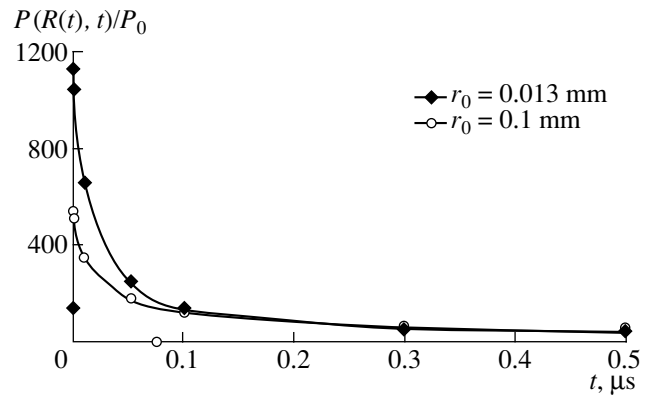
Fig. 4. Reconstructed kinetics of the pressure variation on the expanding plasma piston boundary, calculated taking into account a nonlinear term in the Cauchy–Lagrange integral [12] for a preset pressure at a given point of the wave zone (Fig. 1) and two values of the initial radius.

medium are comparable with or equal to the velocity of a moving boundary, so that a nonlinear term in the Cauchy–Lagrange integral cannot be ignored [10, 11]. Using condition (11) and taking into account (5), we obtain

$$A^2 a - Ab + c = 0, \qquad (12)$$

where

$$a = \frac{1}{2}\rho\left(\frac{t+\beta}{r\rho\omega}\right)^2; \quad b = \frac{1}{\omega}; \quad c = P(r_1, t).$$

Once $P(r_1, t)$, ρ, r_1, and β are known, the A value can be found from Eq. (12) and, using Eqs. (5)–(7), the functions at other points and on the moving boundary can be determined. These exact analytical solutions of the inverse problem with mobile boundaries and non-linear additional condition are of considerable signifi-

cance for both basic science and applications, providing a means of obtaining various estimates, including the maximum values and jumps of the functions under consideration.

The fact that the values of indeterminate forms in solving Eq. (1) for $P(r_1, t)$ set in the class of Bessel's functions (in images) were previously found by approximate methods [8, 9] met some objections [12]. Now, the exact analytical solutions obtained for the first time for both inverse and direct wave problems with cylindrical symmetry in the regions with mobile boundaries and nonlinear boundary conditions make these objections inessential.

Figures 1–4 show the results of calculations performed by formulas (5)–(10) for $A = 20 \times 10^6$ (kgf s)/cm²; $\rho = 102$ (kgf s)/m⁴; $a = 1460$ m/s; two values of the initial radius, $r_0 = 0.013$ and 0.1 mm; and $r_1 = 0.08$ m; the values of pressures and velocities on the mobile plasma cavity boundary at $t \longrightarrow 0$ were determined by formu-

las (8) and (9). The value of α was determined from the relation

$$1 \times 10^{-6} = \sqrt{\left(t^0 + \alpha + \frac{r_0}{a}\right)^2 - \frac{r_1^2}{a^2}},$$

where $t^0 = \dfrac{r_1 - r_0}{a}$ is the time of the wave arrival at point r_1.

As seen in Figs. 3 and 4, the pressures and velocities on the mobile plasma piston boundary in the initial stage ($t = 0$–0.1 μs) differ significantly (sometimes, by one order of magnitude) from the values for $t > 0.1$ μs. In addition, the functions $P(R(t), t)$ and $v(R(t), t)$ markedly depend on the initial radius r_0: the pressures and velocities reached in the initial stage may differ several times for the r_0 values indicated above. For $t > 0.1$ μs, the pressure at the mobile boundary is virtually independent of the initial radius r_0 for the problem parameters selected, while the velocities $v(R(t), t)$ at $t = 0.5$ μs still differ by a factor of almost two.

The obtained results can be used for investigating the near wave field in the expanding plasma cavity, solving the problems of controlled pulsed processes, modeling breakdowns in electrode gaps, and studying plasma channels and the influence of the initial radius on the functions under consideration.

REFERENCES

1. N. G. Basov, B. P. Borovich, V. S. Stoĭlov, *et al.*, Zh. Tekh. Fiz. **40**, 516 (1970) [Sov. Phys. Tech. Phys. **15**, 399 (1970)].
2. A. F. Aleksandrov, V. V. Zosimov, S. P. Kurdyumov, *et al.*, Zh. Éksp. Teor. Fiz. **61**, 1841 (1971) [Sov. Phys. JETP **34**, 979 (1971)].
3. V. K. Dubovenko, Élektron. Obrab. Mater., No. 2, 62 (1990).
4. K. A. Naugol'nykh and N. A. Roĭ, *Electric Discharges in Water* (Nauka, Moscow, 1971).
5. L. M. Lyamshev, Usp. Fiz. Nauk **151**, 479 (1987) [Sov. Phys. Usp. **30**, 252 (1987)].
6. V. S. Krutikov, Pis'ma Zh. Tekh. Fiz. **14**, 510 (1988) [Sov. Tech. Phys. Lett. **14**, 226 (1988)].
7. V. S. Krutikov, Dokl. Akad. Nauk **368**, 755 (1999) [Dokl. Phys. **44**, 674 (1999)].
8. V. S. Krutikov and A. G. Lopatnev, Pis'ma Zh. Tekh. Fiz. **25** (14), 34 (1999) [Tech. Phys. Lett. **25**, 564 (1999)].
9. V. S. Krutikov and A. G. Lopatnev, Pis'ma Zh. Tekh. Fiz. **26** (17), 17 (2000) [Tech. Phys. Lett. **26**, 760 (2000)].
10. L. I. Slepyan, Dokl. Akad. Nauk SSSR **282**, 809 (1985) [Sov. Phys. Dokl. **30**, 448 (1985)].
11. V. S. Krutikov, Akust. Zh. **42**, 534 (1996) [Acoust. Phys. **42**, 471 (1996)].
12. A. I. Vovchenko, V. G. Kovalev, and V. A. Pozdeev, Prikl. Gidromekh. **3(45)** (3), 19 (2001).

Translated by P. Pozdeev

The Commutation Quality Factor
of Electrically Controlled Microwave Device Components

V. V. Pleskachev and I. B. Vendik

St. Petersburg State Electrotechnical University, St. Petersburg, 197376 Russia
e-mail: mwlab@eltech.ru
Revised manuscript received June 26, 2003

Abstract—Various circuit components based on electrically controlled capacitors can be compared using an integral criterion, called the commutation quality factor and determined by the efficiency of capacitance tuning and the losses in the control device. The value of commutation quality factor is independent of the physical nature of controlled components, which ensures objective comparative analysis of the efficiency of electrically tunable capacitive components operating in the microwave frequency range: *p–i–n* diodes, microelectromechanical switches, diodes with variable *p–n* junction capacitance (varactors), and ferroelectric capacitors. © 2003 MAIK "Nauka/Interperiodica".

Introduction. The development of tunable microwave devices (adjustable filters, phase shifters, etc.) encounters the problem of selecting optimum electrically controlled components for a particular device so as to obtain the required characteristics. This paper addresses the class of tunable microwave device components that can be presented as an equivalent electrically controlled capacitance. There are two principal modes of controlling the capacitance of such components: switching and smooth tuning. Switchable components possess two states characterized by different capacitances, whereas the capacitance of tunable components can be smoothly varied over a certain range. The group of switching capacitive devices includes semiconductor *p–i–n* diodes and microelectromechanical (MEM) capacitors, while tunable devices include semiconductor diodes with variable *p–n* junction capacitance (varactors) and ferroelectric (FE) capacitors.

A forward-biased *p–i–n* diode represents a semiconductor structure occurring in the state of small resistance (short circuit) due to injection of charge carriers from strongly doped *p* and *n* regions into the central high-ohmic (intrinsic) base region. In the reverse-biased state, the *p–i–n* diode is a capacitor with the base region performing the function of a dielectric [1]. MEM capacitors are miniature mechanical systems comprising microelectrodes spaced by air gap. The width of this gap can vary under the action of the Coulomb attraction forces between the electrodes bearing opposite charges induced by an applied control voltage [2]. In a semiconductor varactor controlled by a reverse bias voltage, the barrier capacitance of the *p–n* junction varies together with the width of a depleted region [3]. In a tunable FE capacitor, the capacitance depends on the control voltage because the applied electric field influences the dielectric permittivity of the ferroelectric material [4].

For comparing the properties of the aforementioned tunable capacitive components, it is expedient to use a universal parameter, the commutation quality factor that depends on the capacitance and losses in the two extreme states of the interval of switching or smooth tuning [5].

The commutation quality factor of an electrically controlled capacitor. Equivalent schemes of an electrically controlled capacitive component in two states are presented in Fig. 1. In terms of this model, the commutation quality factor is defined by the expression [5]

$$K = \frac{(X_1 - X_2)^2}{R_1 R_2}, \qquad (1)$$

where $Z_1 = R_1 + jX_1$ and $Z_2 = R_2 + jX_2$ are the component impedances in the two states corresponding to different bias voltages. Now let us determine the commutation quality factor for various tunable capacitive components.

(i) *p–i–n* diode. The equivalent scheme of a *p–i–n* diode is characterized by three parameters: the resis-
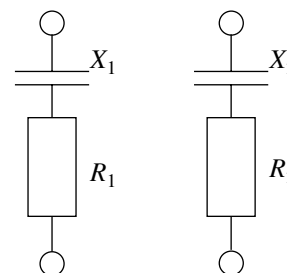
Fig. 1. Equivalent schemes of an electrically controlled capacitive component in two states.

tance (r_+) of the forward-biased diode and the resistance (r_-) connected in series with the capacitance (C) of the reverse-biased diode. Using expression (1), we obtain for this component

$$K = \frac{1}{(\omega C)^2 r_+ r_-}. \tag{2}$$

For a $p–i–n$ diode with the typical parameters [1] $C = 0.3$ pF, $r_+ = r_- = 0.7\ \Omega$ (at 10 GHz), this yields $K = 5.7 \times 10^3$.

(ii) MEM capacitor. A MEM capacitor comprises a mobile electrode spaced by an air gap from the immobile electrode coated by a dielectric film with a permittivity of ε_r. When a bias voltage is applied, the mobile electrode is attracted to the immobile one. In this state, the MEM capacitor (comprising two electrodes separated by the dielectric film) has a capacitance of C_1 and a reactance of $X_1 = \dfrac{1}{\omega C_1}$. The total resistance of this capacitor is $R_1 = R + \dfrac{\tan\delta}{\omega C_1}$, where R is the resistance of electrodes and $\tan\delta$ is the dielectric loss tangent. At a zero bias, the mobile electrode occurs in the initial state, whereby the gaps are separated both by the air gap and by the dielectric film. In this state, the capacitance is $C_2 < C_1$ and the reactance is $X_2 = \dfrac{1}{\omega C_2}$, while the active resistance is determined only by that of the electrodes: $R_2 = R$.

According to definition (1), the commutation quality factor of this capacitor is

$$K = \frac{\left(\dfrac{1}{\omega C_1} - \dfrac{1}{\omega C_2}\right)^2}{R_1 R_2}. \tag{3}$$

For a MEM capacitor with the typical parameters [2] $C_1 = 3.4$ pF, $C_2 = 0.04$ pF, $R = 0.2\ \Omega$, and $\tan\delta = 0.001$ (at 10 GHz), this yields $K = 3.8 \times 10^6$.

(iii) FE capacitor. The equivalent scheme of an FE capacitor is characterized by four parameters: the resistance (r_1) and capacitance (C_1) in the state of zero bias, and the analogous values (r_2 and C_2) for a certain nonzero bias voltage. According to expression (1), this yields

$$K = \frac{\left(\dfrac{C_1}{C_2} - 1\right)^2}{(\omega C_2)^2 r_1 r_2}. \tag{4}$$

This expression is usually written as [5]

$$K = \frac{(n-1)^2}{n \tan\delta_1 \tan\delta_2}, \tag{5}$$
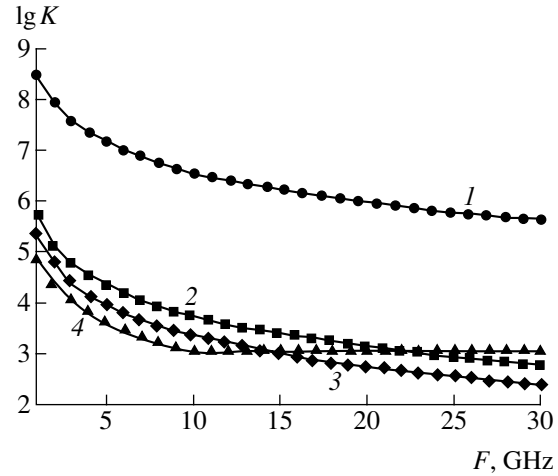
Fig. 2. The frequency dependence of the commutation quality factor calculated for various tunable capacitive components: (*1*) MEM capacitor; (*2*) $p–i–n$ diode; (*3*) varactor; (*4*) FE capacitor.

where $n = C_1/C_2$ is the tunability factor; $\tan\delta_1$ and $\tan\delta_2$ are the loss tangents in the corresponding states. The commutation quality factor of an FE capacitor is equal to that of the ferroelectric film, being independent of the capacitor dimensions. A high-quality ferroelectric film is typically characterized by $n = 2$, $\tan\delta_1 = 0.015$, and $\tan\delta_2 = 0.007$ [6]. The loss tangent of such a film exhibits no pronounced dependence on the frequency in the interval from 10 to 30 GHz [7]. Therefore, the commutation quality factor of a high-quality FE capacitor at 10 GHz is estimated using formula (5) as $K = 5 \times 10^3$.

(iv) Semiconductor diode with tunable $p–n$ junction capacitance (varactor). The equivalent scheme of a varactor is also characterized by four parameters: the capacitance (C_1) in the state of unbiased junction, the capacitance (C_2) at a certain nonzero reverse bias voltage, and the serial (r) and parallel (R) resistances of contacts in both states (with allowance of the losses in the $p–n$ junction). The parameters of the equivalent scheme of Fig. 1 for a varactor are related to these four quantities by the formulas

$$R_1 = r + \frac{1}{(\omega C_1)^2 R}, \quad R_2 = r + \frac{1}{(\omega C_2)^2 R}, \tag{6}$$

where the R value depends (albeit slightly) on the applied voltage. The typical varactor parameters are as follows [5]: $C_1 = 0.5$ pF, $C_2 = 0.17$ pF, $R = 1$ MΩ, and $r = 0.8\ \Omega$. Here, R is an average value: small variations of this quantity with the bias voltage relatively weakly influence the commutation quality factor in the frequency range under consideration. For these parameters, the commutation quality factor of a varactor at 10 GHz is estimated using the formula (1) as $K = 3 \times 10^3$.

Characteristics of tunable capacitive components

	p–i–n diode	MEM capacitor	FE capacitor	Varactor
Tunability $n = C_1/C_2$	–	100	1.5–2	2–4
Commutation quality factor	Medium	High	Medium	Medium
Switching time, s	10^{-6}	10^{-5}	10^{-10}	10^{-6}
Power consumption	High	Low	Low	Low
Cost	High	Medium	Low	High
Technological effectiveness*	Medium	High	High	Medium
Reliability	Medium	Low	High	Medium

* Technological properties of a planar microwave device incorporating a given tunable capacitive component.

A comparison of the commutation quality factor for the tunable capacitive components in the 1–30 GHz frequency range. Figure 2 shows the frequency dependences of the commutation quality factor calculated in the 1–30 GHz range for the electrically tunable capacitive components of the four types considered above. The calculation was performed using the parameters of equivalent schemes of the capacitive components presented in the previous section. For the FE capacitor, we used the frequency dependence of $\tan\delta$ reported in [7]. The results of a comparative analysis of the four tunable capacitive components are summarized in the table.

Conclusion. We have studied the commutation quality factor of various tunable capacitive components for microwave frequency range (1–30 GHz) and performed a comparative analysis of the characteristics of these components.

REFERENCES

1. G. S. Khizha, I. B. Vendik, and E. A. Serebryakova, *Microwave Switches and Phase Shifters* (Radio i Svyaz', Moscow, 1984).

2. D. Peroulis, S. P. Pacheco, K. Sarabandi, and L. P. B. Katehi, IEEE Trans. Microwave Theory Tech. **51**, 259 (2003).

3. O. G. Vendik and S. P. Zubko, Integr. Ferroelectr. **34**, 215 (2001).

4. I. B. Vendik, O. G. Vendik, and E. L. Kollberg, in *Proceedings of the 29th European Microwave Conference, Munich, 1999*, Vol. 3, pp. 187–190.

5. I. B. Vendik, O. G. Vendik, and E. L. Kollberg, IEEE Trans. Microwave Theory Tech. **48**, 802 (2000).

6. J. S. Horwitz, W. Chang, A. C. Carter, *et al.*, Integr. Ferroelectr. **22** (1–4), 278 (1998).

7. O. G. Vendik, S. P. Zubko, and M. A. Nikol'ski, J. Appl. Phys. (2003, in press).

Translated by P. Pozdeev

The Pressure of Light on Gas Bubbles: Compensation of the Buoyancy Force

G. V. Belokopytov* and A. V. Zhuravlev

Moscow State University, Moscow, 119899 Russia
* e-mail: gvb@phys.msu.su
Received March 25, 2003

Abstract—We have calculated the pressure of light on a gas bubble in a liquid medium. The conditions of optical immersion are analyzed, under which the bubble in the liquid occurs in the state of a stable equilibrium. Peculiarities and the possible applications of the optical immersion effect are considered. © *2003 MAIK "Nauka/Interperiodica".*

As is known, the pressure of light developed by a laser beam of moderate intensity (below 10^5 W/cm²) is sufficient to compensate for the gravity force acting upon particles with dimensions from a few to several hundred microns. The laser-induced levitation of small particles is widely used in physical experiment (see, e.g., [1]). This study was aimed at demonstrating that the pressure of light illuminating a gas bubble in a liquid medium is capable of compensating for the Archimedean (buoyancy) force acting upon this bubble, so as to allow the bubble to occur in a stable equilibrium in the liquid.

The theory allows us to calculate $\overline{C}_{pr}$, the efficiency of a pressure acting upon a spherical particle illuminated by light. According to [2], this quantity is proportional to the force acting upon the particle due to the pressure of light:

$$F_{pr} = \pi a_0^2 p \overline{C}_{pr}, \tag{1}$$

where a_0 is the particle radius and p is the momentum flux density. It should be noted, however, that the formulas for $\overline{C}_{pr}$ (including that in [2]) are frequently written with errors. We have calculated $\overline{C}_{pr}$ using the relations [3] that provide good agreement between calculated [4] and experimental [5] data on the optical levitation. According to [3],

$$\overline{C}_{pr} = \overline{C}_{ext} - \langle \cos(\theta) \rangle \overline{C}_{sca}, \tag{2}$$

where

$$\overline{C}_{ext} = \frac{2}{|\alpha|^2} \sum_{n=1}^{\infty} (2n+1)\mathrm{Re}(a_n + b_n), \tag{3}$$

$$\langle \cos\theta \rangle \overline{C}_{sca} = \frac{4}{|\alpha|^2} \sum_{n=1}^{\infty} \left\{ \frac{n(n+2)}{n+1}\mathrm{Re}(a_n a_{n+1}^* + b_n b_{n+1}^*) \right. $$
$$\left. + \frac{2n+1}{n(n+1)}\mathrm{Re}(a_n b_n^*) \right\}, \tag{4}$$

and a_n, b_n are the partial amplitudes of the field of the scattered wave given by the formulas

$$a_n = \frac{m\psi_n(\beta)\psi_n'(\alpha) - \psi_n'(\beta)\psi_n(\alpha)}{m\psi_n(\beta)\xi_n'(\alpha) - \xi_n(\alpha)\psi_n'(\beta)},$$
$$b_n = \frac{\psi_n(\beta)\psi_n'(\alpha) - m\psi_n'(\beta)\psi_n(\alpha)}{\psi_n(\beta)\xi_n'(\alpha) - m\xi_n(\alpha)\psi_n'(\beta)}. \tag{5}$$

Here, $\beta = m_1 q$, $\alpha = m_2 q$, $q = 2\pi a/\lambda_0$ is the diffraction parameter, $m = m_1/m_2$ (m_1 and m_2 being the refractive indices inside and outside the bubble, respectively), λ_0 is the light wavelength in vacuum, and ψ_n, ξ_n are the Riccati–Bessel functions [3]. In the calculations for $q < 100$, the sums in expressions (3) and (4) were calculated taking into account the terms with $n \leq 150$.

The results of calculations of the pressure efficiency for a bubble in water ($m_2 = 1.33$) and glycerin ($m_2 = 1.47$) are presented in the figure as the plots of $1/\overline{C}_{pr}$ directly proportional to the energy flux density S_0 of a laser beam compensating the Archimedean buoyancy force $F_{arc} = \frac{4}{3}\pi a_0^3 \rho g$. Since the momentum flux density in a light beam is $p = S_0 m_2/c$, the equilibrium condition $F_{pr} = F_{arc}$ together with relation (1) yield

$$S_0 = \frac{4}{3} a_0 \rho g \frac{c}{m_2} \frac{1}{\overline{C}_{pr}}. \tag{6}$$

$l/\overline{C}_{\mathrm{pr}}$
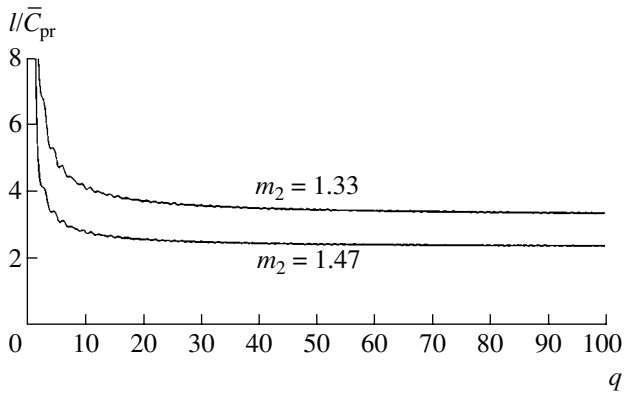
Plots of the normalized power necessary for the optical immersion of a bubble versus the diffraction parameter ($m_1 = 1$).

Taking $a_0 = 10\ \mu\mathrm{m}$, $\rho = 1 \times 10^3\ \mathrm{kg/m^3}$, $g = 9.8\ \mathrm{m/s^2}$, and assuming that $1/\overline{C}_{\mathrm{pr}} = 4$, we obtain $S_0 \approx 1.2 \times 10^4\ \mathrm{W/cm^2}$. For a levitating water droplet of the same size, rough estimates are of the same order of magnitude: $S_0 \approx 0.8 \times 10^4\ \mathrm{W/cm^2}$.

The function $\overline{C}_{\mathrm{pr}}(q)$ for a gas bubble is much smoother than the analogous dependence for a drop [4, 5]: the former curve exhibits no resonance peaks and shows rather weakly pronounced small-scale features (ripples). The different behavior of $\overline{C}_{\mathrm{pr}}(q)$ in the two cases is explained by the fact that the scattering from drops contains a significant contribution from the high-Q oscillations known as the whispering gallery modes or morphological resonances. In the case of bubbles, the Q values of the resonance modes are relatively small ($Q < 2 \times 10^2$) while the density of resonances is approximately the same as that for drops [6]. As a result, the adding of resonance responses in the sums entering into expressions (3) and (4) leads to smoothening of $\overline{C}_{\mathrm{pr}}$ as a function of the diffraction parameter.

In contrast to the case of liquid drops or solid microresonators, immersed gas bubbles are characterized by a significant compressibility that has to be taken into account in the analysis of equilibrium under the action of a light beam. Let a gas bubble occur in the field of a Gaussian beam incident downward along a vertical line. If the beam diameter in the focal plane $z = 0$ is W_0 and the beam divergence angle is θ, the energy flux density S_0 and, hence, the corresponding force of pressure depends on the coordinate as

$$F_{\mathrm{pr}} = F_0\left(1 + \left(\frac{2\tan\theta}{W_0}\right)^2 z^2\right)^{-1}. \qquad (7)$$

The buoyancy force also varies with the coordinate z

because the equilibrium radius of the bubble depends on the depth of immersion as

$$a = a_0\left(1 + \frac{z}{H}\right)^{-1/3}, \qquad (8)$$

where H is the height of a liquid column under the focal plane. Considering the condition $F_{\mathrm{pr}} = F_{\mathrm{arc}}$ and taking in to account formulas (7) and (8), it is easy to check that a stable equilibrium takes place for $z > 0$ (under the focal plane), while the equilibrium at $z < 0$ (above the focal plane) is unstable.

In addition to the condition of longitudinal stability, the optical levitation and immersion require that the particles would possess the transverse stability in the inhomogeneous light beam. Roosen showed (see, e.g., [7]) that the transverse stability can be studied to the first approximation within the framework of the geometrical optics. Since a light ray striking the bubble deviates from the axis of symmetry upon refraction, it is also easy to check that the transverse stability is ensured for a bubble occurring at the minimum of intensity (e.g., on the axis of the TEM^*_{01} mode).

The power density level (on the order of $10^5\ \mathrm{W/cm^2}$) required for the optical immersion can be achieved with widely used lasers, in which the light beam power can be readily controlled by varying the pumping power.

By monitoring the optical immersion state under the action of a controlled light source and a feedback system, it is possible to trace changes in the bubble size dynamics under the action of various factors. The information gained in these experiments (e.g., about the growth of bubbles) refers to the conditions of heat and mass transfer different from those in the experiments with drops [1, 8]. In particular, the radiant power absorbed in and near the bubbles, as well as the convective forces, is much lower than that in the case of drops.

Bubbles occurring under optical immersion conditions can be used for determining forces acting upon these objects. Such bubbles offer convenient probes for monitoring the hydrodynamic flows and acoustic waves in liquid media.

The optical immersion provides convenient conditions for the investigation of nonlinear optical effects on individual bubbles, including those involving acoustic and capillary oscillations (such as induced Mandelshtam–Brillouin scattering and induced surface scattering). These phenomena take place under special conditions, whereby the resonance is provided by elec-

tromagnetic modes of a bubble while a nonlinear condensed medium is outside the resonator.

REFERENCES

1. A. Ashkin, Science **210** (4744), 1081 (1980).

2. H. C. van de Hulst, *Light Scattering by Small Particles* (Wiley, New York, 1957; Inostrannaya Literatura, Moscow, 1961).

3. C. F. Bohren and D. R. Huffman, *Absorption and Scattering of Light by Small Particles* (Wiley, New York, 1983; Mir, Moscow, 1986).

4. P. Chylek, J. T. Kiehl, and M. K. W. Ko, Phys. Rev. A **18**, 2229 (1978).

5. A. Ashkin and J. M. Dziedzic, Appl. Opt. **20**, 1803 (1981).

6. G. V. Belokopytov, A. V. Zhuravlev, and A. I. Sokolov, Preprint No. 1/2003 Fiz. Fak. MGU (Department of Physics, Moscow State University, Moscow, 2003).

7. G. Roosen, Can. J. Phys. **57**, 1260 (1979).

8. J. Popp, M. Lankers, K. Schaschek, *et al.*, Appl. Opt. **34**, 2380 (1995).

Translated by P. Pozdeev

On the Possibility of Eliminating the Energy Threshold for Electron Detection in Semiconductor Detectors

I. V. Eremin, S. G. Konnikov, and K. Yu. Pogrebitskiĭ

Ioffe Physicotechnical Institute, Russian Academy of Sciences, St. Petersburg, 194021 Russia

Received February 26, 2003

Abstract—A method of eliminating the energy threshold for electron detection in semiconductor devices is described. The class of devices used for the detection and measurement of electron emission is sufficiently large, including electrostatic analyzers, gas-filled devices, microchannel plates, etc. An alternative to these types of devices for electron detection is offered by semiconductor radiation detectors based on the *p–n* junctions, which are widely used in the spectrometry of nuclear particles including medium- and high-energy electrons (10^2 keV and above). These detectors are obviously advantageous in comparison to the devices of other types, but there are several factors hindering the use of semiconductor detectors for the detection and analysis of low-energy electrons (in the kiloelectronvolt range). We propose an approach that allows the energy threshold for electron detection in semiconductor detectors to be eliminated by means of preliminary acceleration of the detected particles in an electrostatic field created between the emitter and the detector. This approach removes the basic factor limiting the use of semiconductor detectors in a number of diagnostic methods based on the analysis of electron emission, such as the extended X-ray absorption fine structure (EXAFS), surface EXAFS, and X-ray absorption near-edge structure (XANES) techniques. © *2003 MAIK "Nauka/Interperiodica".*

Introduction. Among the analytical tools used for studying the basic properties of various samples, from solids to biological objects, on the atomic level, an important position is occupied by methods based on the phenomenon of electron emission from the sample surface, for example, upon X-ray excitation. It is important not only to detect the electrons emitted from a sample, but to measure their spectrum as well.

The electron emission spectra are usually measured using electrostatic and magnetic analyzers based on the fact that electrons possessing different energies move along different trajectories in the external fields. Possessing record energy resolutions, energy analyzers of the aforementioned types are relatively large and difficult to manufacture, adjust, and operate. The energy range of high-resolution analysis in these instruments is usually rather narrow, which significantly limits their application. Gas-filled proportional electron energy analyzers possess better transmission characteristics, smaller dimensions, and simpler design. Unfortunately, these detectors have to be mounted inside the gas chambers, which is unacceptable in many applications. Widely used as electron detectors are the microchannel plates, which also possess small dimensions, simple design, and high sensitivity. Unfortunately, these devices are energy-dispersive only in a rather narrow energy interval of electron energies and are used mostly for measurements of the quantum yield of electron emission.

An alternative to the aforementioned types of electron detectors is offered by semiconductor radiation detectors based on the *p–n* junctions, which are widely used in the spectrometry of nuclear particles including medium- and high-energy electrons (10^2 keV and above). The main advantages of these detectors are as follows:

(i) The possibility of simultaneously detecting particles in a broad energy range, which reduces the time necessary for accumulating statistically reliable information.

(ii) A broad range of dimensions (from 10 μm^2 to 100 cm^2) and configurations of the working area of detectors.

(iii) The possibility of one- and two-dimensional matrix design, which allows position-sensitive detectors to be obtained.

(iv) High technological properties facilitating the manufacture of detectors and related electronics.

(v) Small dimensions and low weight of semiconductor detectors.

Unfortunately, there are several factors limiting the possibility of using semiconductor detectors in the analyzers of low-energy electrons (in the kiloelectronvolt range). The main negative factors are (i) the existence of an energy threshold for detection, below which reliable measurement of the energy spectrum is impossible or the sensitivity is lost and (ii) spectral noises of the detector and related electronics, which interfere with the electron energy spectrum in the range below several kiloelectronvolts. From the standpoint of photo-

electron spectrometry in the energy range from a few electronvolts, these disadvantages are principal and their removal is vital for expanding the field of application of semiconductor detectors.

In this paper, we propose an approach that allows the energy threshold for electron detection in semiconductor detectors to be eliminated, which removes the basic factor limiting the use of semiconductor detectors in a number of diagnostic methods based on the analysis of electron emission, such as the extended X-ray absorption fine structure (EXAFS), surface EXAFS, and X-ray absorption near-edge structure (XANES) techniques.

Detection principle and its implementation. During the analysis of the structure and composition of solids by methods based on the photoelectron emission, the samples are exposed to a radiation inducing the emission of electrons. For example, the surface of a sample studied by the EXAFS technique is irradiated by X-ray photons with energies on the order of several kiloelectronvolts, which are absorbed with ionization of the core electron levels [1]. This leads to the production of the so-called primary electrons (photoelectrons, Auger electrons) with energies ranging, depending on the atomic composition of the sample, from a few electronvolts up to several kiloelectronvolts. A part of these electrons can escape from the sample surface, thus accounting for the phenomenon of X-ray induced electron emission [1]. Therefore, the energy spectrum of electrons emitted from solids under the action of X-ray radiation extends from zero to a maximum energy of the X-ray photons incident onto the sample.

Apparently, the process of transformation of the electron energy into an output signal in any detector is accompanied by a certain distortion of information concerning the true energy spectrum. In the case of semiconductor detectors, one of the main factors distorting the electron spectrum is related to the presence of a "dead" layer on the detector surface, or the input window insensitive to electrons [2, 3]. The thickness of this input window ranges from several hundred ångströms to several microns, depending both on the thickness of a heavily doped semiconductor layer forming the p^+–n junction and on the electric field distribution in the near-surface region of this junction [4]. As a result, the energy of a detected electron, that is, the energy deposited in a sensitive volume of the detector and proportionally converted into the output electric signal is smaller than the true energy by an amount lost during passage through the input window:

$$\Delta_w = \varepsilon W,$$

where ε is the specific energy loss in the input window and W is the effective thickness of the input window.

Thus, electrons with energies below Δ_w will not be detected, while the spectrum of electrons with energies $E > \Delta_w$ will shift toward lower energies,

$$E^* = E - \Delta_w,$$

where E^* is the energy in the measured spectrum. For ε on the order of 1 keV/μm, the anticipated detection threshold is $\Delta_w \geq 1$ keV [5].

Figures 1(a1) and 1(a2) present an example of the true electron energy distribution, while Fig. 1(b1) shows the effect of the input window of the detector (a part to the left of the ordinate axis is lost).

Another factor limiting the energy range of detected electrons from below is the presence of noises related to the dark current of the semiconductor detector and the process of amplification of the detector signal. The intensity of noise pulses increases with decreasing amplitude (Fig. 1(c1)), which results in the appearance of a background that masks the electron spectrum or even completely suppresses this spectrum if the count rate of noise pulses exceeds that of the useful signal [3]. Figure 1(d1) shows a true spectrum and its part (to the right of the dotted line) reliably detected.

With allowance of the above limiting factors, a reliable energy spectrum cannot be obtained in the energy interval 0–$\Delta_w + \Delta_n$, where Δ_n is the equivalent energy of the noise pulses counted at a rate equal to the electron count rate.

In order to eliminate the aforementioned restrictions, we suggest to use preliminary acceleration of the detected particles in an electrostatic field created between a sample emitting electrons and the semiconductor detector. This solution is partly analogous to the principle employed in various photomultipliers and photoelectron image converters, where the photoelectrons emitted from a cathode are accelerated in an electrostatic field and detected on the anode. However, the detection of photoelectrons in these devices is not accompanied by spectrometry, so that the useful information is restricted to the emission intensity.

Figure 2 shows a possible configuration of the accelerating system adapted to EXAFS measurements. By virtue of the cylindrical geometry, the angular distribution of emitted electrons is retained, while their energies are additively increased by $q\varphi$, where q is the electron charge and φ is the potential difference between the sample and the sensitive surface of the detector (Fig. 1(b2)). If $q\varphi$ is greater than $\Delta_w + \Delta_n$, all electrons emitted from the sample surface will be detected (Fig. 1(d1)) and their spectrum will have no distortions related to the input window and the background of noise pulses. It is important to note that, by subtracting the constant component $q\varphi$, the true energy spectrum of the emitted electrons can be restored.

The choice of the accelerating potential φ depends on the detector characteristics, input window thickness, and noise level. From a practical standpoint, the poten-
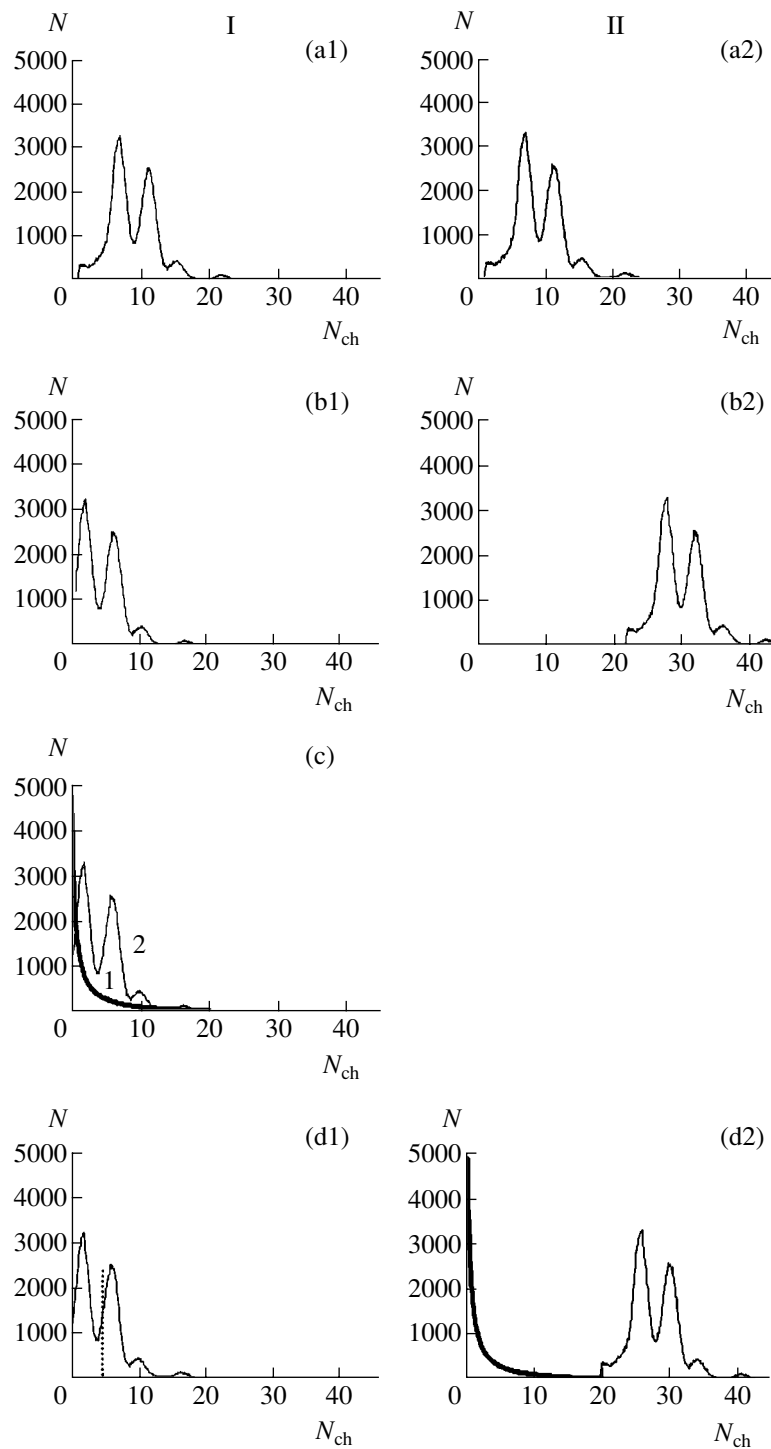
Fig. 1. Typical electron spectrum detected (I) by existing detectors and (II) using the proposed approach: (1) noise; (2) useful signal; (N_{ch}) channel number.

tial φ should be minimized. This can be achieved by reducing the input window thickness and the noise level. In addition, the electron scattering on the input window gives rise to fluctuations in the energy absorbed in the sensitive volume of the detector and converted into a useful output signal. Therefore, a decrease in the input window thickness is of funda-

mental importance for the obtaining of high energy resolution.

Thus, the proposed approach allows the electron energy spectrum to be measured in the entire range, begging with zero energy, and eliminates the influence of both the input window and the noise of the semicon-
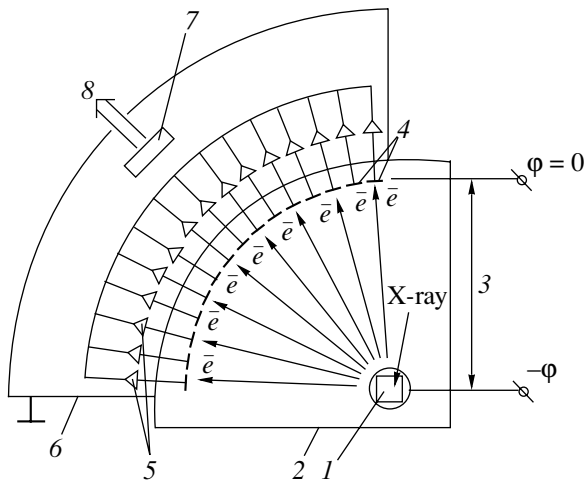
Fig. 2. Schematic diagram of an electron spectrometer with preliminary acceleration: (*1*) sample; (*2*) vacuum chamber; (*3*) acceleration region; (*4*) individual detectors; (*5*) charge-sensitive preamplifiers; (*6*) screen; (*7*) multiplicator; (*8*) to spectrometric amplifier.

ductor detector as factors determining the energy threshold for detecting low-energy electrons (Fig. 1(d2)).

In X-ray photoelectron spectroscopy, the development of spectrometers with preliminary acceleration of photoelectrons will increase the volume and quality of useful information and, hence, will expand the analytical possibilities of related techniques.

In addition to the use in analytical methods involving the analysis of the electron emission spectrum, the proposed approach to electron detection can be implemented for (i) the detection of reflected electrons in electron microscopy and (ii) the detection of radioactive elements (e.t., tritium) emitting low-energy electrons.

REFERENCES

1. *X-Ray Absorption: Principles, Applications, Techniques of EXAFS, SEXAFS and XANES*, Ed. by D. C. Koningsberger and R. Prins (Wiley, New York, 1988).

2. C. Grupen, *Particle Detectors* (Cambridge Univ. Press, Cambridge, 2001; Novosibirsk, 1999).

3. *Semiconductor Detectors in Experimental Physics,* Ed. by Yu. K. Akimov (Énergoatomizdat, Moscow, 1989).

4. J. Kemmer, Nucl. Instrum. Methods **169**, 499 (1980).

5. M. Landolt and J. Börnstein, *Numerical Data and Functional Relationships in Science and Technology,* Vol. 17: *Semiconductors*, Ed. by O. Madelung, M. Schulz, and H. Weiss (Heidelberg, New York, 1982).

Translated by P. Pozdeev

The Structure and Properties of a Cr_3C_2–Ni Coating Deposited by a High-Velocity Plasma Jet onto a Copper Substrate

A. D. Pogrebnyak[a],*, M. V. Il'yashenko[a], V. S. Kshnyakin[a],
V. V. Ponaryadov[b], Sh. M. Ruzimov[c], and Yu. N. Tyurin[d]

[a] *Institute of Surface Modification, Sumy, Ukraine*
[b] *Belarus State University, Minsk, Belarus*
[c] *National University, Tashkent, Uzbekistan*
[d] *Paton Institute of Electric Welding, National Academy of Sciences of Ukraine, Kiev, Ukraine*
* e-mail: apogrebnjak@simp.sumy.ua
Revised manuscript received June 6, 2003

Abstract—Chromium carbide–nickel coatings were deposited onto a technical grade copper substrate by means of a high-velocity plasma jet of a plasmatron operating in specially selected regimes. An analysis of the coatings showed evidence of the formation of a Ni-based solid solution, a complex chromium carbide (Cr_7C_3), and an fcc crystal phase with a lattice parameter of 3.614 Å. The surface of the coatings exhibits a characteristic relief resulting from a dynamic interaction between melted and fused particles of the initial powder. The local hardness on some areas of the surface and in depth of the coating reaches 66 ± 4.5 HRC, while the coating adhesion strength varies from 25 to 300 MPa. © *2003 MAIK "Nauka/Interperiodica".*

In recent years, effective methods based on the metal and alloy surface processing by particle, plasma, and radiation beams have been developed for increasing the reliability and durability of articles, tools, and structures. The most widely employed methods of surface hardening are based on the formation of various films and coatings. A new technology for the surface modification of structural materials and the formation of coatings performing protective and other functions is offered by the plasma-detonation spraying (PDS) [1–4]. The PDS technology is based on the surface treatment with a pulsed plasma jet transferred by a detonation wave in the form of a plasma pulse.

As is known, a dense coating with good adhesion to the substrate surface can be obtained (even without heating) provided that metal alloy particles in the jet possess a velocity in the range from 100 to 1000 m/s [2, 3]. Recently, new coating devices have been developed that employ lateral powder supply and gasdynamic control systems [1, 4]. In these devices, gases and metal powders are periodically injected into the system at a reduced pressure in the combustion chamber, immediately after emission of a preceding high-velocity jet of combustion products. It has been suggested [4] to perform the mixing of components and produce detonation of the working gas mixture in a special chamber *1* (Fig. 1) separated from a pulsed plasmatron unit. The plasmatron [5, 6] comprises the inner cone anode *2* and the outer cathode *3* spaced by the interelectrode gap *4* of length *L* in which an electric field *E* is generated by a high-voltage source *5*. A consumable metal rod *6* built into the central electrode is usually made of refractory

metal (W, Mo, Ta, Hf, etc.). The plasmatron has a trunk *7* in which the powdered material is accelerated and heated. The optimum trunk length *H* depends on the powder composition and the degree of dispersion. In particular, the *H* value for depositing oxides is about 380 mm. The powder is injected into the trunk via a special pipe [7].

The sample coatings were obtained in the following regime: pulse repetition rate, 4 Hz; capacitance, $C =$
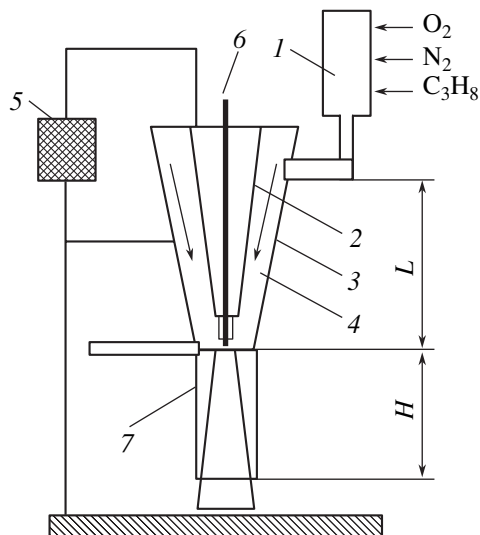
Fig. 1. A schematic diagram of the setup for pulsed plasma-detonation spraying of coatings onto metal substrates (see the text for explanations).
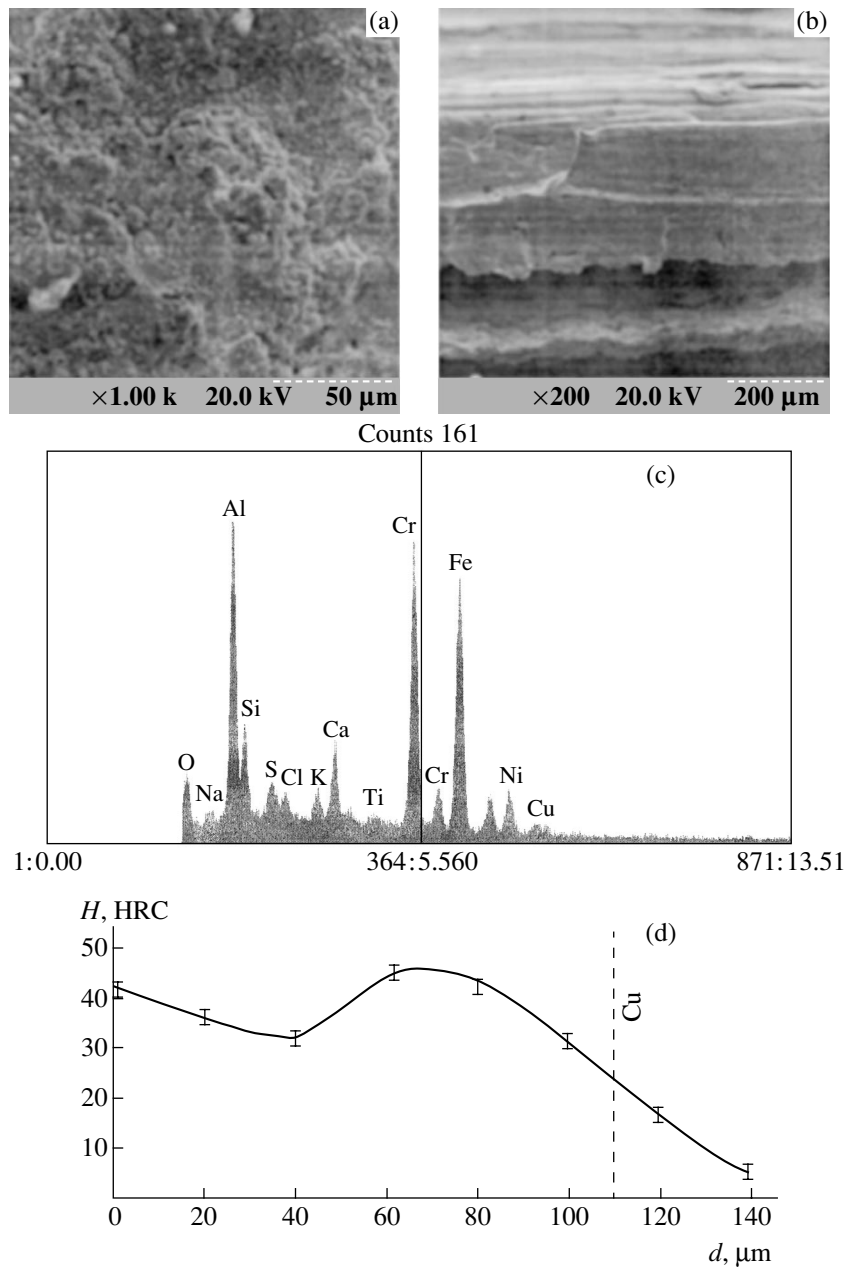
Fig. 2. Characteristics of a Cr_3C_2 + 30 wt % Ni coatings on a copper substrate: (a, b) SEM micrographs of the surface and cross section, respectively; (c) EDX microprobe spectrum measured in a gray area (mixed composition); (d) hardness–depth profile measured in an oblique cross section at a Rockwell pyramid load of 50 g.

600 µF; sample to plasmatron nozzle distance $H = 380$ mm; substrate velocity, $V = 0.6$ cm/s; number of scans, 1 to 4; chromium carbide–nickel powder, KKhN-30 (Cr_3C_2 + 30 wt % Ni); powder particle size, 25–56 µm. The KKhN-30 powder composition was specially developed for the coating on articles working in oxidative and abrasive media at elevated temperatures (300–800°C). Therefore, investigation of the properties of such coatings is of interest for both basic knowledge and applications.

The phase composition of coatings was studied by X-ray diffraction in a DRON-2 diffractometer using CoK_α radiation. The surface morphology was studied in a scanning electron microscope (SEM) of the REMMA-2M type equipped with an energy-dispersive X-ray (EDX) microprobe (Jeol CXA-733). The elemental analysis was performed by secondary-ion mass spectrometry (SIMS) on an MS-7201M system using a primary beam of Ar+ ions with an energy of up to 20 keV. The hardness was determined according to Rockwell (in HRC units). The adhesion strength was evaluated by the diamond pyramid scribing technique on both transverse and oblique sections.

The results of Rockwell hardness measurements at various loads applied to the pyramid

Test no.	Load, g	Hardness, HRC	Area
1–4	50	58 ± 1	Gray
	100	51 ± 3	
	200	48 ± 5	
6, 8, 9, 12	50	62 ± 4	Homogeneous gray
	100	56 ± 1	
	200	50 ± 1	
10, 11, 13	50	27 ± 7	Light
	100	35 ± 3	
	200	50 ± 12	

An analysis of the X-ray diffractograms from the sample coatings showed the presence of three phases: (i) a Ni-based solid solution with a lattice period of $a = 3.525$ Å (cf. tabulated data for Ni, $a = 3.524$ Å); (ii) a chromium carbide with the composition Cr_7C_3; and (iii) a face-centered cubic (fcc) crystal phase with a lattice parameter of 3.614 Å.

Figure 2 shows SEM micrographs of the (a) surface and (b) transverse cross section of the typical coating. The structure and morphology of the coating exhibited significant variations with depth: light areas characteristic of chromium carbide are alternating with dark areas corresponding to the metallic nickel-based inclusions and with gray areas representing a mixed composition. The local EDX microanalysis performed in these areas (Fig. 2c) showed the presence of Cr, Ni, O, Cu, and Fe. The bright-metal areas contained only Ni with a small admixture of Cr and Cu (about 96% Ni and 4% Cu). The latter regions probably represent nickel grains or powder particles with a small content of Cr appearing as a result of fusion and partial melting of Ni grains and chromium oxide particles and their mixing in the liquid state or in the plasma jet. In the light (gray) areas, the atomic concentration of Cr reaches 61%, the other elements being Ni (about 8.5%), oxygen (~5.6%), copper (~13.3%), iron (~2.6%), and aluminum (above 5%), while sulfur, calcium, and silicon amount on the whole to less than 1%. We may suggest that copper is transferred from s substrate as a result of the dynamic and thermal action of the plasma jet. For this reason, the fcc phase with a lattice parameter of 3.614 Å is assigned to copper.

The results of the local hardness measurements performed using a Rockwell pyramid in the transverse section showed a maximum value of 66 ± 4.5 HRC in the light areas (where Cr_7C_3 is the main phase) and 45 ± 1.5 HRC in the dark metal-bright areas (where a Ni-based solid solution predominates). The adhesion strength measured by the diamond pyramid scribing in the transverse and oblique sections gave significantly different values ranging from 25 to 300 MPa.

The results of hardness measurements at various loads applied to the Rockwell pyramid are summarized in the table. These measurements showed that the pyramid indentation depth amounted to tens of microns and was approximately equal to the mark size. An analysis of the hardness as a function of the applied load suggests that the grain size is on the same order of magnitude over the entire coating. Figure 2d shows a plot of the hardness versus depth in a coating obtained by the PDS method. The profile was measured in an oblique section at a constant load on the pyramid. In order to obtain more reliable information about hardness variation in depth of the coating, the measurements were performed only in the gray areas.

In conclusion, we have demonstrated that PDS of chromium carbide containing 30 wt % Ni in optimum regimes allows obtaining coatings of sufficiently good quality, possessing a high hardness (up to 66 HRC) and a good adhesion strength (up to 300 MPa). The coating consists of a Ni-based solid solution, a complex chromium carbide (Cr_7C_3), and a copper-based fcc crystal phase with a lattice parameter of 3.614 Å. The results of testing of the parts of equipment for thermal power plants, such impeller blades and tube linings working in an oxidizing medium (air) or slag at elevated temperatures (300–800°C) showed that Cr_3C_2 + Ni coatings obtained by plasma-jet PDS method ensure higher stability and longer working life.

REFERENCES

1. A. D. Pogrebnyak, M. V. Il'yashenko, O. P. Kul'ment'eva, *et al.*, Zh. Tekh. Fiz. **71** (7), 111 (2001) [Tech. Phys. **46**, 897 (2001)].

2. S. Kuroda, in *Proceedings of the 10th International Conference on Thermal Spray, France, 1999*, p. 539.

3. A. I. Zverev, S. Yu. Sharivker, and E. A. Astakhov, *Detonation Deposition of Coatings* (Sudostroenie, Moscow, 1979).

4. Yu. N. Tyurin and A. D. Pogrebnjak, Surf. Coat. Technol. **111**, 269 (1999).

5. A. D. Pogrebnyak, M. V. Il'yashenko, V. S. Kshnyakin, *et al.*, Pis'ma Zh. Tekh. Fiz. **27** (17), 82 (2001) [Tech. Phys. Lett. **27**, 749 (2001)].

6. A. D. Pogrebnyak, Yu. N. Tyurin, Yu. F. Ivanov, *et al.*, Pis'ma Zh. Tekh. Fiz. **26** (21), 58 (2000) [Tech. Phys. Lett. **26**, 960 (2000)].

7. A. D. Pogrebnjak, M. V. Il'jashenko, O. P. Kul'ment'eva, *et al.*, Vacuum **62**, 21 (2001).

Translated by P. Pozdeev

Nonlinear Corrections to the Frequency of Capillary-Gravitational Waves and to the Critical Conditions for Instability Development on the Charged Surface of a Liquid

D. F. Belonozhko, A. V. Klimov, and A. I. Grigor'ev*

Yaroslavl State University, Yaroslavl, Russia
* e-mail: grig@uniyar.ac.ru
Received April 15, 2003

Abstract—Analytical expressions for the profile of a plane capillary-gravitational wave traveling over a homogeneously charged flat surface of the ideal incompressible liquid and for a nonlinear wave frequency correction are obtained in the third order of smallness with respect to wave amplitude. A nonlinear analysis of the critical conditions for the development of instability on the charged liquid surface with allowance for the virtual wave frequency correction shows that the real value of the critical surface charge density and the wavenumber of the most unstable wave decrease with increasing wave amplitude, instead of being constant as in the linear theory. © 2003 MAIK "Nauka/Interperiodica".

Introduction. Investigation into the laws of instability development on the flat charged surface of a liquid is of considerable interest both for the basic knowledge and for the numerous technological applications (see, e.g., [1, 2] and references therein). Most of the previous theoretical studies were performed within the framework of linear models and only some of the recent works in this field were performed with allowance for the real nonlinearity of the phenomena under consideration [3–6].

While nonlinear capillary-gravitational waves on the uncharged ideal liquid surface were rather extensively studied [7–10], nonlinear corrections to the frequency of traveling capillary waves and to the critical conditions for the development of instability on the flat charged liquid surface (Tonks–Frenkel instability) appearing in the third order of smallness with respect to the wave amplitude have not been obtained so far. The aim of this study was to fill this gap.

Formulation of the problem. Consider the ideal, incompressible electrically conducting liquid with the density ρ and the surface charge density σ, occupying the half-space $z \le 0$ in a Cartesian coordinate system with $\mathbf{n}_z$ unit vector of the z axis and occurring under the action of a gravitational field $\mathbf{g} \parallel -\mathbf{n}_z$. The profile of nonlinear periodic capillary-gravitational waves traveling over the free liquid surface is described by the following system of equations:

$$z \le \xi: \ \Delta\varphi = 0; \quad p = -\rho g z - \rho\frac{\partial\Phi}{\partial t} - \frac{\rho}{2}(\text{grad}\varphi)^2;$$

$$z > 0: \ \Delta\Phi = 0;$$

$$z = \xi: \ \frac{\partial\xi}{\partial t} + \frac{\partial\varphi}{\partial x}\frac{\partial\xi}{\partial x} = \frac{\partial\varphi}{\partial z};$$

$$p + \frac{(\nabla\Phi)^2}{8\pi} = -\gamma\frac{\partial^2\xi}{\partial x^2}\Big(1 + \Big(\frac{\partial\xi}{\partial x}\Big)\Big)^{-3/2}; \quad \Phi = 0;$$

$$z \longrightarrow \infty: \ \text{grad}\Phi = -4\pi\sigma \cdot \mathbf{n}_z;$$

$$z \longrightarrow -\infty: \ \text{grad}\varphi = 0.$$

Here, $\xi = \xi(x, t)$ represents deviation of the free liquid surface from the equilibrium shape $z = 0$, $\varphi(\mathbf{r}, t)$ is the liquid velocity field potential, $\Phi(\mathbf{r}, t)$ is the electric potential over the liquid surface, and γ is the surface tension.

Solution of the problem. By solving the above problem using the multiscale method (see, e.g., [8, 9]) in the third order of smallness with respect to the wave amplitude a (assumed to be small relative to a natural linear scale represented by the capillary constant) we determine the shape of a nonlinear capillary-gravitational wave traveling over the liquid surface:

$$\xi = a\cos[(\omega - a^2\delta)t - kx] + a^2\Lambda\cos[2(\omega t - kx)]$$
$$+ a^3\chi\cos[3(\omega t - kx)];$$

$$\omega^2 \equiv gk(1 + \alpha^2 k^2 - \alpha kW); \quad W \equiv \frac{4\pi\sigma}{\sqrt{\rho g\gamma}}; \quad \alpha \equiv \sqrt{\frac{\gamma}{\rho g}}; \quad (1)$$

$$\Lambda \equiv k\frac{1 + \alpha^2 k^2 - 2\alpha kW}{2(1 - 2\alpha^2 k^2)};$$

$$\chi \equiv k^2 \frac{32\alpha^2 k^2 W^2 - 32\alpha k W(\alpha^2 k^2 + 1) + (6\alpha^4 k^4 + 21\alpha^2 k^2 + 6)}{16(1 - 2\alpha^2 k^2)(1 - 3\alpha^2 k^2)};$$

$$\delta \equiv g k^3 \frac{16\alpha^2 k^2 W^2 - 16\alpha k W(\alpha^2 k^2 + 1) + 2\alpha^4 k^4 + \alpha^2 k^2 + 8}{16\omega(2\alpha^2 k^2 - 1)};$$

where α is the capillary constant, k is the wavenumber, and W is the Tonks–Frenkel parameter characterizing stability of the flat homogeneously charged surface of the electrically conducting liquid.

Discussion. The expression obtained in the third order of smallness for the nonlinear wave profile on the free charged surface of the ideal liquid coincides, in the limit of $W \longrightarrow 0$ ($\sigma \longrightarrow 0$), with the known solution (see [8, 9, 11]) for the profile of a nonlinear capillary-gravitational wave on the uncharged surface of the ideal liquid. As can be seen, the amplitude coefficient Λ of the second-order correction shows a resonance growth at $k = k_2 \equiv 1/(\alpha 2^{1/2})$. The amplitude coefficient χ of the third-order correction exhibits two resonances: at $k = k_2$ and $k = k_3 \equiv 1/(\alpha 3^{1/2})$.

It was demonstrated in the quadratic approximation [12] (with a single resonance at $k = k_2$) that the resonance interaction leads to the energy pumping from longer waves (with the wavenumber $k = k_2$) to shorter waves (with $k = 2k_2$). As can be seen from Eqs. (1), the energy pumping in the same direction takes place in the region of $k = k_3$, whereby the energy is transferred from longer waves with $k = k_3$ to shorter waves with $k = 3k_3$, but the effect has a higher order of smallness.

In addition, Eq. (1) shows that the nonlinear frequency correction is proportional to the squared wave amplitude a and has a negative sign (in the region of wavelengths $k > k_2$ that is of interest from the standpoint of an analysis of the stability of the charged liquid surface). Note that the effect proper is of the third order of smallness: this becomes evident when the term with $\cos[(\omega - a^2\delta)t]$ in (1) is expanded in the powers of $a^2\delta$. It is also interesting to note that the nonlinear frequency correction, as well as the amplitude factors Λ and χ, exhibits a resonance behavior. This implies restricted applicability of the solution (1) in the vicinity of wavenumbers $k = k_2$ and $k = k_3$, since both the amplitude factors and the frequency correction have to be small as compared to the first-order corrections.

Now let us take into account that the critical conditions for the development of the Tonks–Frenkel instability are determined by the conditions that (i) the squared frequency of the virtual wave passes through zero and (ii) the first derivative of the frequency with respect to the wavenumber is zero (the latter condition determines the wavenumber of the capillary wave possessing a maximum instability increment) [13, 14]. In the linear approximation, the critical values of the

Tonks–Frenkel parameter ($W = W_*$) and the wavenumber ($k = k_*$) are as follows [12]:

$$W_* = k_* + \frac{1}{k_*}; \quad k_* = 1.$$

In the nonlinear situation under consideration, the system of algebraic equations with respect to W and k is very cumbersome. Since we are only interested in estimating corrections by the order of magnitude, the critical values of the Tonks–Frenkel parameter and the wavenumber can be represented as expansions in terms of the squared wave amplitude:

$$W_* \approx 2 - wa^2; \quad k_* \approx 1 - \kappa a^2.$$

Substituting these expressions into the system of equations for determining the critical conditions for the development of instability, one can readily obtain $w = 11/8$ and $\kappa = 23/16$.

Thus, the nonlinear analysis shows that the values of the surface charge density and the wavenumber, critical from the standpoint of the instability development on the charged liquid surface, are reduced as compared to analogous values predicted by the linear theory.

The results of calculations performed using the multiscale method in the fourth order of smallness with respect to the wave amplitude show that the nonlinear frequency correction contains no contribution proportional to the third power of the amplitude. Whether the correction proportional to the fourth power of this amplitude is nonzero can be only established by calculations in the fifth-order of smallness. Such a calculation would be useful in order to elucidate the trends in nonlinear corrections to the critical conditions for the development of instability on a charged liquid surface.

Conclusion. A nonlinear correction to the frequency of a plane wave traveling on the surface of a homogeneously charged free flat surface of the ideal liquid was calculated in the third-order of smallness with respect to a small wave amplitude. The correction depends on the squared wave amplitude, exhibits a resonance behavior, and gives rise to nonlinear corrections to the conditions of instability with respect to the charge of the free liquid surface. In the third-order calculation, the critical surface charge density and the wavenumber of the most unstable wave decrease in proportion to the squared wave amplitude.

REFERENCES

1. M. D. Gabovich, Usp. Fiz. Nauk **140**, 137 (1983) [Sov. Phys. Usp. **26**, 447 (1983)].
2. A. I. Grigor'ev and S. O. Shiryaeva, Izv. Ross. Akad. Nauk, Mekh. Zhidk. Gaza, No. 3, 3 (1994).
3. A. I. Zhakin, Izv. Akad. Nauk SSSR, Mekh. Zhidk. Gaza, No. 3, 94 (1984).
4. A. Gonzalez and A. Castellanos, Phys. Rev. E **49**, 2935 (1994).
5. N. M. Zubarev, Zh. Éksp. Teor. Fiz. **116**, 1990 (1999) [JETP **89**, 1078 (1999)].
6. N. M. Zubarev and O. V. Zubareva, Zh. Tekh. Fiz. **71** (7), 21 (2001) [Tech. Phys. **46**, 806 (2001)].
7. J. R. Wilton, Philos. Mag. **29**, 688 (1995).
8. A. H. Nayfeh, J. Fluid Mech. **40**, 671 (1970).
9. A. H. Nayfeh, J. Fluid Mech. **48**, 385 (1971).
10. N. Kim and L. Debnath, Int. J. Non-Linear Mech. **34**, 197 (1999).
11. A. H. Nayfeh, Phys. Fluids **13**, 545 (1970).
12. D. F. Belonozhko and A. I. Grigor'ev, Pis'ma Zh. Tekh. Fiz. **29** (8), 1 (2003) [Tech. Phys. Lett. **29**, 309 (2003)].
13. Ya. I. Frenkel', Zh. Éksp. Teor. Fiz. **6**, 348 (1936).
14. D. F. Belonozhko and A. I. Grigor'ev, Zh. Tekh. Fiz. **73** (11), 37 (2003) [Tech. Phys. **48**, 1396 (2003)].

Translated by P. Pozdeev

Ferromagnetic Resonance in Multilayer Structures with Bilinear and Biquadratic Exchange Coupling

A. M. Shutyĭ and D. I. Sementsov

Ul'yanovsk State University, Ul'yanovsk, Russia
Received June 18, 2003

Abstract—The resonance magnetization dynamics in multilayer nanostructures exposed to transverse and longitudinal magnetic fields is investigated with allowance for biquadratic exchange coupling between the magnetic moments of neighboring layers. It is found that the crystallographic magnetic anisotropy leads to the appearance of a minimum on the field dependence of the resonance frequency for the "acoustic" mode and the accompanying maximum in the magnetic susceptibility. © 2003 MAIK "Nauka/Interperiodica".

Introduction. The unique statistical and dynamic properties of multilayer periodic structures consisting of thin layers of a magnetic metal separated by nonmagnetic metal films are determined primarily by the character of interaction between magnetic moments of these layers [1–3]. This interaction results from the strong indirect exchange coupling and may give rise to ferromagnetic, antiferromagnetic, or noncollinear ordering of the magnetic moments of the neighboring layers [4–6]. The noncollinear ordering is caused by the biquadratic exchange coupling discovered in multilayered structures. The nature of this coupling and its influence on the properties of the above structures have been extensively studied both experimentally and theoretically [7–10]. In particular, it was established that the character of magnetic coupling considerably influences the resonance properties of these structures. Therefore, a thorough study of these properties is necessary both from the standpoint of practical applications of such multiplayer structures and for the extension and refinement of our notions about mechanisms behind the biquadratic coupling.

Previously, the features of the ferromagnetic resonance in $(Fe/Cr)_n$ structures were investigated without considering the cubic crystallographic anisotropy [8, 9]. However, in the nanostructures under consideration, the manifestation of the crystallographic anisotropy may be significant. It is known [11] that the effect of the crystallographic anisotropy field in ferromagnetic single crystal films leads to new features in the resonance dynamics of magnetic moments. Averaging the resonance characteristics over all grains in polycrystalline films of a nanostructure can only slightly weaken the manifestations of these features. In this study, we investigate the ferromagnetic resonance in multilayer nanostructures with a cubic crystallographic anisotropy and the induced uniaxial magnetic anisotropy with allowance for the bilinear and biquadratic exchange coupling between the magnetic moments of the neighboring layers.

Theory. Consider a structure consisting of a sufficiently large number ($n \gg 1$) of layers of a magnetic metal with a magnetization $\mathbf{M}_i$ and a thickness d_i (i is the magnetic layer number). The magnetic layers are separated by nonmagnetic films with thickness corresponding to the initial antiferromagnetic ordering of magnetic moments of the neighboring layers. In accordance with the available experimental data for the structures of this kind (for example, $(Fe/Cr)_n$ [12]), the magnetic anisotropy of Fe layers is a combination of the uniaxial induced anisotropy (of the "easy axis" type) and the crystallographic cubic anisotropy. The crystallographic [100] and [010] axes lie in the plane of the layers and the easy magnetization axis of the induced anisotropy is oriented perpendicularly to these layers.

For the multiplayer system under consideration, the free energy per unit area is given by the expression

$$E = \sum_{i=1}^{n} d_i \left[-\mathbf{H}\mathbf{M}_i + \frac{K_{1i}}{4}(\sin^2 2\psi_i + \cos^4 \psi_i \sin^2 2\varphi_i) \right.$$

$$\left. + (K_{ui} - 2\pi M_i^2)\cos^2 \psi_i \right] + \sum_{i=1}^{n} \mathbf{m}_i \mathbf{m}_{i+1}(J_1 + J_2 \mathbf{m}_i \mathbf{m}_{i+1}), \quad (1)$$

where $\mathbf{m}_i = \mathbf{M}_i/M_i$ and J_1 and J_2 are the constants of the bilinear and biquadratic coupling, respectively, caused by the indirect exchange coupling of magnetic moments of the adjacent layers and dependent, in the general case, on the thickness, material type, and structural characteristics of the intermediate films; K_{1i} and K_{ui} are the constants of the cubic and growth-induced anisotropy, respectively; $\mathbf{H}$ is the static bias field; φ_i is the azimuth angle measured from the [100] axis and determining the plane orientation of the magnetic moment of the films; and ψ_i is the angle of the vector $\mathbf{M_i}$ relative to the film plane.

All the magnetic layers are assumed to be identical, that is, $M_i = M$, $d_i = d$, $K_{ui} = K_u$, and $K_{1i} = K_1$. In this case, the entire system of the magnetic layers can be divided into two subsystems ($j = 1, 2$) so that the layers in each subsystem behave identically. With allowance for high demagnetizing fields in the structures realized in practice ($4\pi M \gg 2K_u/M$, $J_{1,2}M$), the magnetic moments in the case of a plane bias field **H** lie in the plane of the layers; therefore, the equilibrium angles $\psi_{0j} = 0$. To find the equilibrium azimuth angles $\varphi_{0j}(H)$, we use the equilibrium conditions $\partial E/\partial\varphi_j = 0$ and $\partial^2 E/\partial\varphi_j^2 > 0$ that, in view of Eq. (1), lead to the system of equations:

$$2HM\sin(\varphi_{0j} - \varphi_H) + K_1\sin 4\varphi_{0j} - 2\bar{J}_1\sin(\varphi_{0j} - \varphi_{03-j})$$
$$- 2\bar{J}_2\sin 2(\varphi_{0j} - \varphi_{03-j}) = 0,$$
$$HM\cos(\varphi_{0j} - \varphi_H) + 2K_1\cos 4\varphi_{0j} - \bar{J}_1\cos(\varphi_{0j} - \varphi_{03-j})$$
$$- 2\bar{J}_2\cos 2(\varphi_{0j} - \varphi_{03-j}) > 0,$$
$$(2)$$

where $j = 1, 2$; φ_H is the azimuth angle measured from the [100] axis and determining the plane direction of the field **H**; and $\bar{J}_{1,2} = 2J_{1,2}/d$.

The equations of motion for the magnetization vectors **M**$_i$ in each of the layers are chosen in the Landau–Lifshitz form. In a spherical coordinate system, these equations can be written as follows:

$$\dot{\varphi}_j Md\cos\psi_j = \gamma\frac{\partial E}{\partial\psi_j} + \frac{\lambda}{M}\frac{1}{\cos\psi_j}\frac{\partial E}{\partial\varphi_j},$$
$$\dot{\psi}_j Md = \frac{\lambda}{M}\frac{\partial E}{\partial\psi_j} - \gamma\frac{1}{\cos\psi_j}\frac{\partial E}{\partial\varphi_j},$$
$$(3)$$

where γ is the gyromagnetic ratio and λ is the damping parameter. In the linear approximation with respect to small deviations from the equilibrium position ($\delta_j = \varphi_j - \varphi_{0j}$), the high-frequency susceptibility of the system can be represented as a sum $\chi = \chi_1 + \chi_2$, where the susceptibilities of the particular subsystems have the form

$$\chi_j = \frac{M^2}{\Delta_1\Delta_2 - D^2}[D\sin(\varphi_{03-j} - \varphi_h)$$
$$- \Delta_{3-j}\sin(\varphi_{0j} - \varphi_h)]\exp(i\alpha_j).$$
$$(4)$$

Here, φ_h is the azimuth angle of the microwave field **h**; D and Δ_j are the parameters given by the formulas

$$D = \bar{J}_1\cos(\varphi_{01} - \varphi_{02}) + 2\bar{J}_2\cos 2(\varphi_{01} - \varphi_{02}),$$

$$\Delta_j = (\omega_{0j}^2 - \omega^2 + 4\pi i\lambda\omega)/4\pi\gamma^2 - D,$$

and ω_{0j} are the resonant frequencies of isolated magnetic layers in each of the subsystems in the absence of dissipation:

$$\omega_{0j}^2 = 4\pi\gamma^2[HM\cos(\varphi_{oj} - \varphi_H) + 2K_1\cos 4\varphi_{0j}]. \quad (5)$$

In deriving expressions (4), we assumed that $h(t) = h\exp(i\omega t)$ and $\delta_j(t) = \delta_{j0}\exp(i\omega t - i\alpha_j)$. The amplitude of oscillations of the polar angle is always much less than that of the azimuth angle.

Numerical analysis. Let us consider the effect of the cubic crystallographic anisotropy on the resonance magnetization dynamics on the basis of a numerical analysis of the above equations. We use the parameters corresponding to a real (Fe/Cr)$_n$ structure: for the iron layers, the magnetization $M = 1620$ G, the constant of the growth-induced anisotropy $K_u = 2.06 \times 10^6$ erg/cm^3, $\lambda = 5 \times 10^7$ s^{-1}, $\gamma = 1.76 \times 10^7$ (Oe s)$^{-1}$, and the thickness $d = 21.2 \times 10^{-8}$ cm; the parameters of the Cr layers do not enter explicitly in expression (1), but they determine the values of the coupling constants.

Figure 1 shows (a) the resonance precession frequency of the magnetic moments and (b) the absolute value of magnetic susceptibility as functions of the bias field for the values of the anisotropy constants $K_1 = (0, 2.3, 4.6) \times 10^5$ erq/cm^3 (curves *1–3*). The coupling constants are taken equal to $J_1 = 0.2$ erg/cm^2 and $J_2 = 0.115$ erg/cm^2. The solid curves represent the "acoustical" branch corresponding to a transverse microwave field (**h** $\perp$ **H**) and the phase difference of precession motions in the neighboring layers $\alpha_1 - \alpha_2 = 0$. The dashed curves refer to the "optical" branch corresponding to a longitudinal microwave field (**h** $\parallel$ **H**) and $\alpha_1 - \alpha_2 = \pi$. From these dependences, it follows that the presence of the crystallographic anisotropy leads to the appearance of a minimum on the field dependence of the resonance frequency corresponding to the acoustical mode. Consequently, there exists a frequency range where the resonant precession in the transverse microwave field of one frequency is excited for two values of the bias field. The minimum corresponds to a maximum of the resonance magnetic susceptibility of the system. This maximum is absent when the crystallographic anisotropy constant equals zero. With increasing the constant K_1, the minimum of the resonance frequency shifts toward higher frequencies, and the maximum of the magnetic susceptibility increases. For the optical mode, the crystallographic anisotropy only leads to an insignificant decrease in the resonance frequency and an increase in the magnetic susceptibility of the system. The maximum value of the bias field for the optical mode decreases. This is associated with a decrease in the saturation field when the magnetic moments of both subsystems are parallel.

Figure 2 shows the field dependences of the resonance frequency (solid curves) and the resonance magnetic susceptibility (dashed curves). These curves correspond to the acoustical mode for the anisotropy constant $K_1 = 4.6 \times 10^5$ erg/cm^3 and the coupling constants $J_1 = 0.175$ erg/cm^2 and $J_2 = 0.1$ erg/cm^2 (curves *1*) and $J_1 = 0.4$ erg/cm^2 and $J_2 = 0.23$ erg/cm^2 (curves *2*). From these data, it follows that enhancement of the exchange coupling levels out the extrema of the resonance depen-
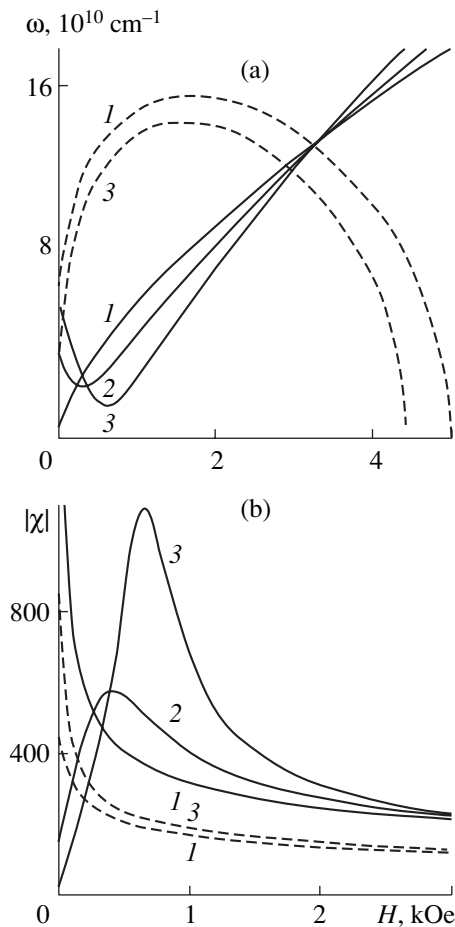
Fig. 1. Field dependences of (a) the resonance frequency and (b) magnetic susceptibility for the acoustical (solid curves) and optical (dashed curves) precession modes of the magnetic moments, calculated for $K_1 = (0, 2.3, 4.6) \times 10^5$ erg/cm^3 (*1–3*); $J_1 = 0.2$ erg/cm^2, and $J_2 = 0.115$ erg/cm^2.
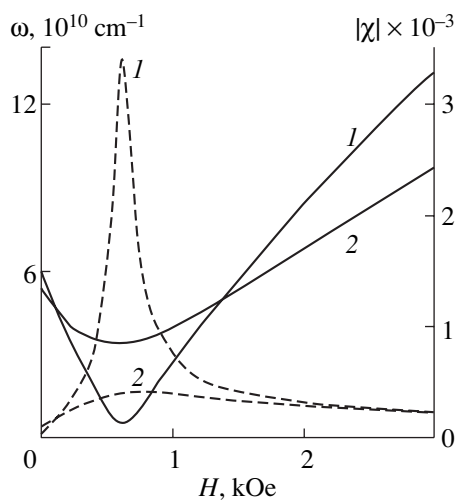
Fig. 2. Field dependences of the resonance frequency (solid curves) and magnetic susceptibility (dashed curves) for the acoustical mode, calculated for $K_1 = 4.6 \times 10^5$ erg/cm^3; (*1*) $J_1 = 0.175$, $J_2 = 0.1$ and (*2*) $J_1 = 0.4$, $J_2 = 0.23$ erg/cm^2.

dences of $\omega(H)$ and $|\chi|(H)$, but the frequency range in which the two values of the bias field correspond to one resonance frequency remains unchanged. The results obtained from a numerical solution of nonlinear equations (3) are close to those presented above even for fairly large amplitudes of the microwave field.

Thus, our analysis showed that the cubic crystallographic anisotropy of ferromagnetic layers in multilayer nanostructures with bilinear and biquadratic exchange coupling significantly affects predominantly the acoustical modes of the resonance magnetization precession. This effect leads to the appearance of a minimum in the dependence of the resonant frequency on the bias field and the accompanying maximum in the magnetic susceptibility of the system. Since the contribution from the crystallographic anisotropy in the nanostructures of this type is usually comparable to that from the growth-induced anisotropy, this result should be taken into account when designing microwave devices and elements based on such structures.

REFERENCES

1. M. N. Baibich, J. M. Broto, A. Fert, *et al.*, Phys. Rev. Lett. **61**, 2472 (1988).
2. Yu. V. Kudryavtsev and P. Gontazh, Fiz. Met. Metalloved. **77** (6), 44 (1994).
3. A. M. Shutyĭ and D. I. Sementsov, Fiz. Met. Metalloved. **95** (3), 5 (2003).
4. A. Schreyer, J. F. Ankher, Th. Zeidler, *et al.*, Phys. Rev. B **52**, 16066 (1995).
5. V. V. Ustinov, M. M. Kirillova, I. D. Lobov, *et al.*, Zh. Éksp. Teor. Fiz. **109**, 477 (1996) [JETP **82**, 253 (1996)].
6. G. S. Patrin, N. V. Volkov, and V. P. Kononov, Pis'ma Zh. Éksp. Teor. Fiz. **68**, 287 (1998) [JETP Lett. **68**, 307 (1998)].
7. D. M. Edwards, J. M. Ward, and J. Mathon, J. Magn. Magn. Mater. **126**, 380 (1993).
8. N. G. Bebenin, A. V. Kobelev, A. R. Tankeev, and V. V. Ustinov, Fiz. Met. Metalloved. **82**, 348 (1996).
9. A. B. Drovosekov, N. M. Kreĭnes, D. I. Kholin, *et al.*, in *Proceedings of the 16th International School-Seminar on New Magnetic Materials for Microelectronics (NMMM-16), Moscow, 1998*, Chap. 1, pp. 14–15.
10. A. K. Zvezdin and V. V. Kostyuchenko, Fiz. Tverd. Tela (St. Petersburg) **41**, 461 (1999) [Phys. Solid State **41**, 413 (1999)].
11. A. M. Shutyĭ and D. I. Sementsov, Zh. Éksp. Teor. Fiz. **118** (3), 110 (2000) [JETP **91**, 531 (2000)].
12. M. A. Milyaev, L. N. Romashev, V. V. Ustinov, *et al.*, in *Proceedings of the 18th International School-Seminar on New Magnetic Materials for Microelectronics (NMMM-18), Moscow, 2002*, Chap. 1, pp. 102–104.

Translated by Yu. Vishnyakov

Attractor Coverage Time, Time Dimension, and Its Relation to Capacity Dimension

A. A. Koronovskiĭ*, A. V. Starodubov, and A. E. Khramov**

State Scientific Center "College," Saratov State University, Saratov, Russia
*e-mail: * alkor@cas.ssu.runnet.ru; ** aeh@cas.ssu.runnet.ru*
Received April 22, 2003

Abstract—We have studied the time to complete coverage of a chaotic attractor by cells as a function of the cell size. This dependence is described with good precision by a power law. The system attractor is characterized by a new quantity called the time dimension by analogy with the capacity dimension. A relation between the two values has been studied. For a homogeneous chaotic attractor characterized by a uniform invariant probability density distribution, the two dimensions coincide. In the case of an inhomogeneous chaotic attractor, the time dimension is greater than the capacity one. © 2003 MAIK "Nauka/Interperiodica".

The analysis of transient processes is an important and sometimes even the primary task in the investigation of dynamics in many systems, since such processes can frequently provide important information about the whole system and its dynamics [1–4]. In cases when a dynamic system exhibits a periodic behavior in time, there is a quite simple and sufficiently effective method for the analysis of transient processes [5–7]. This method, typically used for the analysis of maps, can also be applied to flow systems by using the Poincaré section procedure [8]. However, if a system exhibits involved chaotic oscillations, the transient analysis encounters considerable difficulties [9].

The main difficulty is related to determining the transient process duration by means of a special procedure based on the construction of a basis array of the attractor cells [10]. The method proposed in [9, 10] is as follows. The region of initial conditions containing the attractor is covered with a lattice (one-, two-, or *n*-dimensional, depending on the dynamic system dimension) with a cell size (discretization step) ε. Then, an initial condition is selected and the system is iterated a sufficiently large number of times N (definitely greater than the maximum transient time duration). In the course of this iteration process, the imaging point travels over the lattice following the attractor and passing through various lattice cells. Beginning with a certain discrete time, the transient process is considered terminated and the number of cells visited by the imaging point during the iterative procedure (these cells are considered as belonging to the chaotic attractor) is counted. After termination of the iterative procedure, we obtain the so-called "basis" array of the attractor cells that is used for determining the transient process duration as described in [10].

For correctly determining the transient process duration, it is desired to find possibly large number of the attractor cells. Let us characterize the time required for constructing the basis array by the attractor coverage time $T_c(\varepsilon)$. For the dynamic systems with discrete time, the coverage time is defined as the number of iterations necessary for the complete coverage of all elements of a chaotic attractor by cells of size ε, averaged over a large number of initial conditions.

Thus, the coverage time is related to the number of attractor cells. As the cell size ε decreases, the number of cells in the lattice and the number of cells covering the attractor grow and, hence, the time required for determining the attractor cells increases. Let us study the dependence of the attractor coverage time T_c on the lattice cell size ε for a logistic map

$$x_{n+1} = \lambda x_n (1 - x_n), \tag{1}$$

which is a standard model in the nonlinear dynamics and the theory of oscillations. In Eq. (1), λ is the control parameter determining the oscillation regimes. We will study the map (1) with λ = 3.58, for which the system exhibits chaotic oscillations.

Figure 1 shows a plot of the chaotic attractor coverage time T_c versus the lattice cell size ε. This dependence was determined by averaging over one hundred observations with various initial conditions for each value of ε. Following the above definition, the coverage time for each ε was determined as the number of the iteration step in which the last attractor cell was found (after which the iteration procedure was continued over a sufficiently large number of discrete time units so as to be sure that the chaotic attractor is completely covered and no new cells are added to the basis array). Then, the attractor coverage time was determined for the same ε with different initial conditions and the results were averaged over a large number of observations.
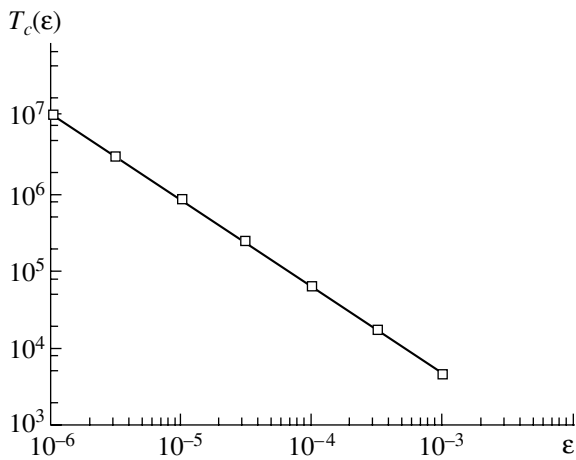
Fig. 1. A double logarithmic plot of the attractor coverage time T_c versus the lattice cell size ε for a logistic map with $\lambda = 3.58$. Symbols $\square$ show the results of numerical modeling averaged over 100 initial conditions and $N = 10^9$ iterations for each ε value. Solid line represents the power law (2) with $a = 1.1375 \pm 0.002$.
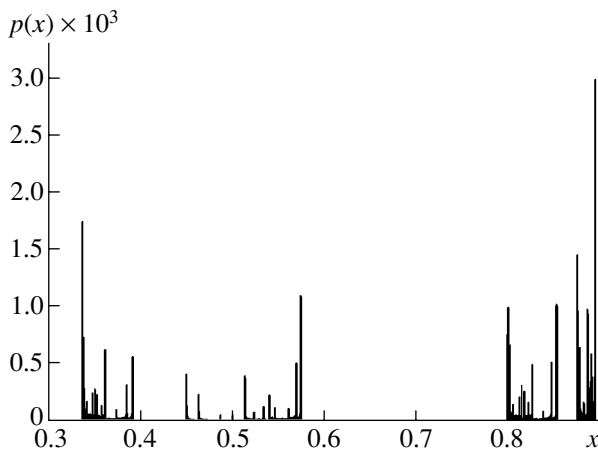
Fig. 2. An invariant distribution of the probability density $p(x)$ of the imaging point visits to the attractor cells for a logistic map with $\lambda = 3.58$. The distribution was obtained for $N = 10^9$ iterations on a lattice with the cell size $\varepsilon = 10^{-5}$.

As can be seen from Fig. 1, the $T_c(\varepsilon)$ plot can be described with good accuracy by a power law

$$T_c(\varepsilon) \sim \varepsilon^{-a} \qquad (2)$$

for the given control parameter λ, the exponent in this law determined by least squares is $a = 1.1375 \pm 0.002$.

Obviously, a change in the control parameter λ will modify the attractor. Accordingly, the attractor coverage time $T_c(\varepsilon)$ and the exponent a will change as well. Thus, both the coverage time and the exponent a are important intrinsic characteristics of the chaotic attractor.

Since the growth in the attractor coverage time $T_c(\varepsilon)$ with decreasing ε is related to an increase in the number

of attractor cells, the exponent in the power law (2) can be related to the capacity dimension D_0 [11] because this characteristic determines a change in the number of attractor cells in response to the change in the cell size of a lattice covering the attractor. The number of attractor cells depends on the lattice cell size as [11]

$$N(\varepsilon) \sim \varepsilon^{-D_0}. \qquad (3)$$

Here, $N(\varepsilon)$ is the number of lattice cells covering the given attractor for the lattice discretization step ε and D_0 is the attractor capacity dimension. Taking logarithm and considering the limit of $\varepsilon \longrightarrow 0$, we obtain an explicit expression for the capacity dimension

$$D_0 = -\lim_{\varepsilon \to 0} \frac{\log N(\varepsilon)}{\log \varepsilon} \qquad (4)$$

(the logarithm base is arbitrary).

By analogy with the capacity dimension D_0, let us introduce the quantity τ_0, called the time dimension, as

$$\tau_0 = -\lim_{\varepsilon \to 0} \frac{\log T_c(\varepsilon)}{\log \varepsilon}. \qquad (5)$$

This quantity will characterize the dependence of the attractor coverage time $T_c(\varepsilon)$ on the lattice cell size. Similar approach is employed for characterizing the recurrence time of the imaging point to a small vicinity of a fixed point [12] by introducing a spectrum of the generalized recurrence time dimensions.

Since both characteristics, τ_0 and D_0, of a given attractor are related to the number of attractor cells, it is interesting to consider a relationship between these values. A comparison of the capacity and time dimensions leads to a conclusion that τ_0 is greater than D_0 (for the system under consideration with $\lambda = 3.58$, $D_0 = 0.9983 \pm 0.0001$).

We may suggest that the difference between τ_0 and D_0 is related to inhomogeneity of the attractor existing in the phase space of the system.[1] Indeed, there are cells of the attractor (or regions composed of such attractor cells) that are less frequently visited by the imaging point as compared to the other cells (or regions). This fact is illustrated in Fig. 2 showing an invariant distribution of the probability density of the imaging point visits to the attractor cells. As can be seen, there are cells visited with a lower probability than all other cells. As the ε value decreases, the number of attractor cells increases according to relation (3). It the attractor were homogeneous (i.e., the invariant distribution of the probability density of visits were uniform, $p(x) =$ const), we would expect that an increase in the attractor coverage time $T_c(\varepsilon)$ corresponds to an increase in the

---

[1] In this case, by inhomogeneity we imply the fact that various points of the attractor are characterized by different probabilities of being visited by the imaging point.

number of cells $N(\varepsilon)$: for a homogeneous attractor, the time dimension τ_0^h may coincide with the capacity dimension D_0^h.

Indeed, consider a dynamic system with discrete time $x_{n+1} = f(x_n)$ characterized by a homogeneous chaotic attractor with the capacity dimension D_0 and an invariant distribution of the probability density $p(x) = $ const. The number of attractor cells depends on the ε value according to relation (3) as $N(\varepsilon) = N_0 \varepsilon^{-D_0}$. The probability of visits to an attractor cell is

$$P = (1/N_0)\varepsilon^{D_0^h}. \qquad (6)$$

Taking into account (i) a strong dependence of the system dynamics in the regime of chaotic oscillations on the initial conditions and (ii) the homogeneity of the attractor, we can assume that the probability for the imaging point to visit a given attractor cell in the nth iteration step is determined only by relation (6) and weakly depends on where the imaging point occurred in the $(n-1)$th step. Then, the probability P_k that the entire attractor will be covered with cells during k iterations is

$$P_k = N_0 \varepsilon^{-D_0^h} \exp\left(-\frac{k}{N_0 \varepsilon^{-D_0^h}}\right), \qquad (7)$$

and the condition that the attractor coverage time is $T_c(\varepsilon) = K$ appears as $P_K = 1$. Therefore, the attractor coverage time $T_c(\varepsilon)$ in the case under consideration is determined as

$$T_c(\varepsilon) = N_0 \varepsilon^{-D_0^h} \ln(N_0 \varepsilon^{-D_0^h}), \qquad (8)$$

and according to the definition (5), the time dimension is

$$\tau_0^h = -\lim_{\varepsilon \to 0} \frac{\ln(N_0 \varepsilon^{-D_0^h} \ln(N_0 \varepsilon^{-D_0^h}))}{\ln \varepsilon} = D_0^h. \qquad (9)$$

Thus, in the case of a homogeneous chaotic attractor characterized by a uniform invariant probability density distribution, the time and capacity dimensions coincide. For an inhomogeneous attractor, the situation is different: as a rule, the attractor cells characterized by greater probabilities will be visited (covered) first, while the cells with a lower probabilities of visits will be covered later. Taking into account inhomogeneity of the attractor, the complete coverage time in this case will be greater than that for the homogeneous attractor. In the double logarithmic plot of the attractor coverage

time $T_c(\varepsilon)$, this is manifested by a greater slope and, accordingly, by an increase in the time dimension τ_0 as compared to the value τ_0^h for the homogeneous attractor. Apparently, the time dimension τ_0 of an inhomogeneous chaotic attractor is always greater than the capacity dimension D_0. It should be noted that analogous conclusion concerning a difference between the spectrum of generalized recurrence time dimensions and the spectrum of generalized dimensions was made in [12].

In conclusion, we have introduced the attractor coverage time $T_c(\varepsilon)$ and the time dimension τ_0 characterizing attractors for discrete dynamic systems and established a relationship between these quantities and the capacity dimension D_0.

REFERENCES

1. V. V. Astakhov, B. P. Bezruchko, O. B. Pudovochkin, and E. P. Seleznev, Radiotekh. Élektron. (Moscow) **38**, 291 (1993).

2. B. P. Bezruchko, T. V. Dikanev, and D. A. Smirnov, Izv. Vyssh. Uchebn. Zaved., Prikl. Nelineǐnaya Din. **9** (3), 3 (2001).

3. B. P. Bezruchko, T. V. Dikanev, and D. A. Smirnov, Phys. Rev. E **64**, 036210 (2001).

4. I. Triandaf, E. M. Bollt, and I. B. Schwartz, Phys. Rev. E **67**, 037201 (2003).

5. G. B. Astaf'ev, A. A. Koronovskiǐ, and A. E. Khramov, Izv. Vyssh. Uchebn. Zaved., Prikl. Nelineǐnaya Din. **11** (2003, in press).

6. A. A. Koronovskiǐ, D. I. Trubetskov, A. E. Khramov, and A. E. Khramova, Dokl. Akad. Nauk **383**, 322 (2002) [Dokl. Phys. **47**, 181 (2002)].

7. A. A. Koronovskiǐ, D. I. Trubetskov, A. E. Khramov, and A. E. Khramova, Izv. Vyssh. Uchebn. Zaved., Radiofiz. **45**, 880 (2002).

8. M. Hénon, Physica D **5**, 412 (1982).

9. A. A. Koronovskiǐ, A. V. Starodubov, and A. E. Khramov, Izv. Vyssh. Uchebn. Zaved., Prikl. Nelineǐnaya Din. **10** (5), 25 (2002).

10. A. A. Koronovskiǐ, A. V. Starodubov, and A. E. Khramov, Pis'ma Zh. Tekh. Fiz. **29** (8), 32 (2003) [Tech. Phys. Lett. **29**, 323 (2003)].

11. S. P. Kuznetsov, *Dynamic Chaos*, in *Modern Theory of Vibrations and Waves* Series (Fizmatlit, Moscow, 2001).

12. N. Hadyn, J. Luevano, G. Mantica, and S. Vaienti, Phys. Rev. Lett. **88**, 224502 (2002).

Translated by P. Pozdeev

Nonlinear Susceptibility Interference in Laser SRS–CARS Diagnostics of Hydrogen in Gas Mixtures

G. M. Mikheev*, D. G. Kalyuzhnyĭ, and A. Yu. Popov
Institute of Applied Mechanics, Ural Division, Russian Academy of Sciences, Izhevsk, Udmurtia, Russia
e-mail: gmmikheev@udmnet.ru
Received May 26, 2003

Abstract—We have studied the possibility to measure small hydrogen concentrations in dense gas mixtures by method of coherent anti-Stokes Raman scattering (CARS) in combination with biharmonic laser pumping by means of stimulated Raman scattering (SRS). It was found that the interference of nonlinear susceptibilities of a buffer gas and hydrogen can lead to a parabolic dependence of the signal intensity on the hydrogen concentration, which makes the results of analyses uncertain. The ambiguity can be eliminated by selecting an appropriate composition and pressure of the gas mixture in the cell of the SRS generator of biharmonic laser pumping. Using this approach, hydrogen in air at atmospheric pressure can be detected by the laser SRS–CARS technique on a level of 5 ppm. © *2003 MAIK "Nauka/Interperiodica".*

The problem of selective and rapid diagnostics of hydrogen in condensed media and dense gas mixtures (e.g., in air at atmospheric pressure) is currently of importance [1, 2]. In connection with this, it was of interest to develop a relatively simple analytical method based on the coherent anti-Stokes Raman scattering (CARS) in combination with biharmonic laser pumping by means of stimulated Raman scattering (SRS) [3–6] for the laser diagnostics of hydrogen in gas mixtures. This study was aimed at determining the influence of the interference of nonresonance and resonance nonlinear molecular susceptibilities on the SRS–CARS diagnostics of hydrogen in dense gas mixtures.

CARS is a four-photon parametric process, whereby mixing two laser beams with the frequencies ω_p and ω_s in a medium possessing a cubic nonlinear susceptibility $\chi^{(3)}$ results in the generation of a coherent directional radiation at an anti-Stokes frequency $\omega_a = 2\omega_p - \omega_s$ [7]. For the SRS–CARS diagnostics of hydrogen, the analyzed medium is probed by a biharmonic laser pumping beam at the frequencies ω_p and ω_s obeying an approximate resonance condition

$$\omega_p - \omega_s \approx \Omega_{H_2-BG}, \qquad (1)$$

where Ω_{H_2-BG} is the frequency of the $Q_{01}(1)$ vibrational transition in hydrogen present in a buffer gas (BG) mixture possessing a density of ρ_{H_2-BG}. The necessary biharmonic laser pumping is preliminarily created in an SRS generator by focusing a high-power monochromatic laser radiation beam with a frequency of ω_p onto

a cell with compressed hydrogen at a pressure of P_{H_2} ($\omega_p - \omega_s = \Omega_{H_2-H_2}$, the frequency of the $Q_{01}(1)$ vibrational transition in hydrogen at P_{H_2}).

The scattered radiation intensity I_a at the anti-Stokes frequency ω_a is determined by the relation

$$I_a \sim \left| \chi^{(3)R} + \chi^{(3)NR} \right|^2 I_p^2 I_s, \qquad (2)$$

where I_p and I_s are the intensities of radiation at the frequencies ω_p and ω_s, respectively; $\chi^{(3)R} = n_{H_2} \gamma_r$ is the cubic resonance susceptibility of the impurity molecules studied; $\chi^{(3)NR} = n_{BG} \gamma_{BG}$ is the cubic nonresonance susceptibility due to the electron contribution (related predominantly to the participation of buffer gas molecules in the scattering events); γ_r and γ_{BG} are the cubic hyperpolarizabilities of the impurity and the buffer gas, respectively; n_{H_2} and n_{BG} are the number densities of molecules of the impurity (H_2) and the buffer gas, respectively (it is assumed that $n_{H_2} \ll n_{BG}$).

The cubic resonance susceptibility $\chi^{(3)R}$ is given by the following expression [7]:

$$\chi^{(3)R} = \frac{1}{3} \Delta_k^n \frac{2\pi n_{H_2} c^4}{h\Gamma\omega_s^4} \frac{d\sigma}{do} \frac{\Gamma}{\Omega_{H_2-BG} - (\omega_p - \omega_s) - i\Gamma}, \qquad (3)$$

where Γ is the full width at half maximum (FWHM) of the Raman-active transition; Δ_k^n is the differential population of levels; $d\sigma/do$ is the molecular cross sec-

tion of spontaneous Raman scattering for the given Raman-active transition.

As can be seen from relations (2) and (3), the non-resonance contribution $\chi^{(3)NR}$ can be ignored for $\rho_{H_2-BG} \ll 1$ Amagat (the case of rarefied gas mixtures). In this case, the quantity $[I_a/(I_p^2 I_s)]^{1/2}$ determined from relation (2) is proportional to the hydrogen concentration n_{H_2}. However, when small hydrogen concentrations are present in a buffer gas occurring at atmospheric pressure, the nonresonance contribution $\chi^{(3)NR}$ becomes significant and the dependence of $[I_a/(I_p^2 I_s)]^{1/2}$ on n_{H_2} can be nonlinear because of interference of the nonlinear susceptibilities of the impurity and the buffer gas. By virtue of the coherent character of CARS, contributions from the molecules of various types to scattered signal intensity exhibit interference rather that simple addition [7]. However, to our knowledge, this problem was not considered in application to the SRS–CARS diagnostics of hydrogen in gas mixtures.

Taking into account expression (3), relation (2) can be transformed to

$$\frac{I_a}{I_p^2 I_s} = b\left(\frac{\gamma^2}{1+\Delta^2}n_{H_2}^2 - \frac{2n_{BG}\gamma\gamma_{BG}\Delta}{1+\Delta^2}n_{H_2} + n_{BG}^2\gamma_{BG}^2\right), \quad (4)$$

where b is a coefficient and

$$\gamma = \frac{1}{3}\Delta_k^n \frac{2\pi c^4}{h\Gamma\omega_s^4}\frac{d\sigma}{do}, \quad (5)$$

$$\Delta = \frac{\Omega_{H_2-H_2} - \Omega_{H_2-BG}}{\Gamma}. \quad (6)$$

According to relation (4), the dependence of $I_a/(I_p^2 I_s)$ on n_{H_2} at $\Delta \le 0$ is a monotonically increasing function. However, for $\Delta > 0$, this dependence exhibits a minimum at an impurity concentration of

$$n_{H_2}^{min} = \frac{n_{BG}\gamma_{BG}}{\gamma}\Delta. \quad (7)$$

In the absence of impurity molecules, the SRS–CARS signal intensity is determined by the nonresonance scattering from buffer gas molecules:

$$\frac{I_a}{I_p^2 I_s} = b(n_{BG}^2\gamma_{BG}^2). \quad (8)$$

For $\Delta > 0$, adding hydrogen to a buffer gas will lead to a decrease in the signal intensity. At the point of mini-

mum, the signal is

$$\left(\frac{I_a}{I_p^2 I_s}\right)_{min} = b\left(\frac{n_{BG}^2\gamma_{BG}^2}{1+\Delta^2}\right). \quad (9)$$

As the hydrogen concentration grows further, the signal exhibits a monotonic increase. Therefore, the SRS–CARS analysis in the case of $\Delta > 0$ is ambiguous: in the region of small impurity concentrations ($n_{H_2} < 2n_{H_2}^{min}$), the same signal intensity corresponds to two values of the hydrogen concentration. This ambiguity is eliminated at $\Delta \le 0$.

Our experiments were conducted using the SRS–CARS optical scheme for hydrogen diagnostics described in [6]. The hydrogen pressure in the SRS generator was $P_{H_2} = 4$ bar. We have studied the response $I_a/(I_p^2 I_s)$ as a function n_{H_2} at various pressures of the H_2–BG mixture, where BG was nitrogen, argon, helium, air, carbon dioxide, neon, propane, ethane, or elegas.

For example, Fig. 1 presents the plots of $I_a/(I_p^2 I_s)$ versus the relative hydrogen concentration $C_{H_2} = n_{H_2}/N$ ($N = 2.68 \times 10^{19}$ cm^{-3} is the Loschmidt number) in argon (buffer gas) at various pressures. As can be seen, introducing hydrogen at small concentrations into the optical cell at $P_{Ar} > 0.5$ bar (Fig. 1b and 1c) leads to a decrease in the SRS–CARS signal intensity. At a certain $C_{H_2}^{min}$ (dependent on P_{Ar}), the scattering signal intensity exhibits a minimum and then increases with C_{H_2} according to the parabolic law. Similar results were obtained for the H_2–BG mixtures with BG = nitrogen, air, carbon dioxide, propane, ethane, or elegas. In the mixtures H_2–He and H_2–Ne, the $I_a/(I_p^2 I_s)$ value exhibited a monotonic growth with increasing C_{H_2} in the entire range of BG pressures from 0 to 1 bar.

These experimental results are consistent with formula (4), taking into account that the parameter Δ depends both on the hydrogen pressure in the SRS generator and on the pressure of the H_2–BG mixture studied. Indeed, according to [8], the Δ value can be expressed to the first approximation as follows:

$$\Delta = \frac{a_{H_2-H_2}\rho_{H_2-H_2} - a_{H_2-BG}\rho_{H_2-BG}}{\Gamma}, \quad (10)$$

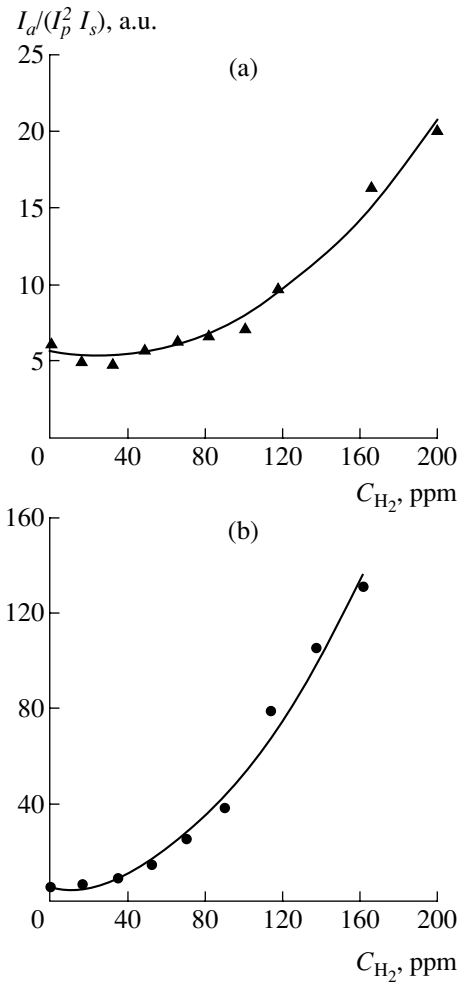where $a_{H_2-H_2}$ is the coefficient characterizing a shift of the $\Omega_{H_2-H_2}$ level due to the collisions between hydrogen molecules ($a_{H_2-H_2} < 0$); $\rho_{H_2-H_2}$ is the hydrogen density in the SRS generator; a_{H_2-BG} is the coefficient charac-
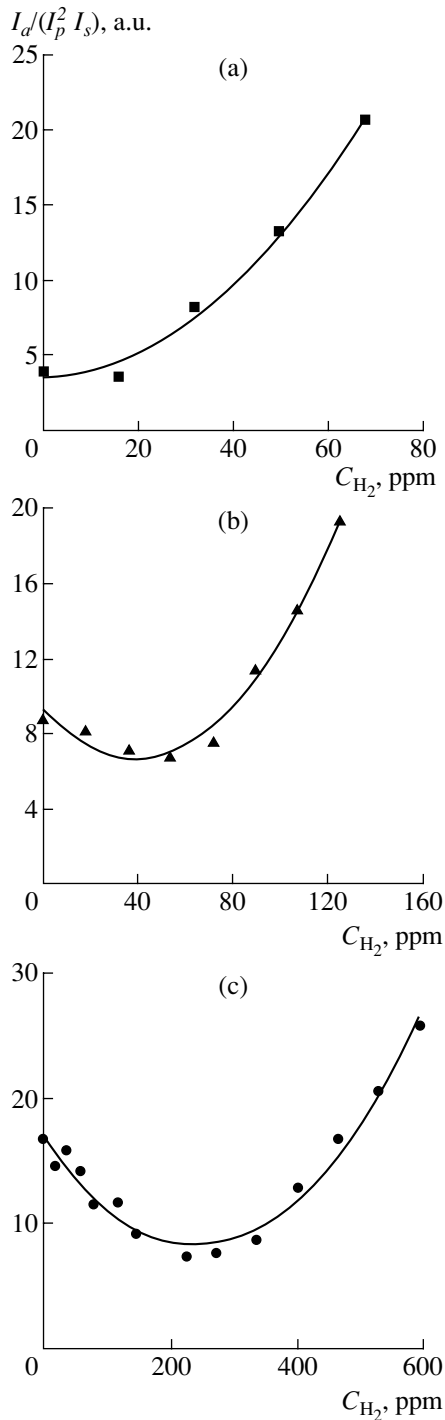
Fig. 1. Plots of the SRS–CARS signal intensity $I_a/(I_p^2 I_s)$ versus hydrogen concentration C_{H_2} in H₂–Ar gas mixture at various argon pressures ($T = 295$ K): (a) 0.54; (b) 0.76; (c) 1.0 bar.

Fig. 2. Plots of the SRS–CARS signal intensity $I_a/(I_p^2 I_s)$ versus hydrogen concentration C_{H_2} in air at atmospheric pressure, measured using an SRS generator with the cell filled with (a) pure H₂ and (b) an H₂–Ar mixture (87% H₂– 13% Ar) at a pressure of 4 bar and $T = 295$ K.

terizing a shift of the Ω_{H_2-BG} level due to the collisions between hydrogen molecules and buffer gas particles; and ρ_{H_2-BG} is the hydrogen–buffer gas mixture density. As shown in [8–10], the coefficients a_{H_2-BG} are nega-

tive for the H₂–Ar and H₂–N₂ mixtures and positive for the H₂–He and H₂–Ne mixtures. Accordingly, the Δ values for H₂–Ar and H₂–N₂ mixtures are negative at small ρ_{H_2-BG} densities and become positive at large values of ρ_{H_2-BG}. For the H₂–He and H₂–Ne mixtures, the Δ value is positive for all ρ_{H_2-BG} values. This behavior agrees with the experimental data.

The critical buffer gas density, above which the $I_a/(I_p^2 I_s)$ versus C_{H_2} curves exhibit a minimum, can be increased either by increasing the hydrogen pressure in the SRS generator or by adding an appropriate buffer gas (e.g., argon) capable of decreasing the frequency of the vibrational transition $Q_{01}(1)$. The experimental dependence of $I_a/(I_p^2 I_s)$ on C_{H_2} measured in air at atmo-

spheric pressure using an SRS generator with $P_{H_2} = 4$ bar ($T = 295$ K) exhibits a minimum (Fig. 2a). An analogous dependence measured using the same SRS generator with the cell filled with an H_2–Ar mixture (87% H_2–13% Ar) at $P_{H_2-Ar} = 4$ bar shows a monotonic increase in $I_a/(I_p^2 I_s)$ with C_{H_2} (Fig. 2b).

Thus, by selecting a proper composition and pressure of the gas mixture in the SRS generator cell it is possible to eliminate ambiguities during the SRS–CARS detection of hydrogen in dense gas mixtures. Using an automated system of SRS–CARS hydrogen diagnostics [11] with optimized composition and pressure of the gas mixture in the SRS generator cell, we succeeded in detecting 5 ppm of hydrogen in air at atmospheric pressure. This is more than ten times better as compared to the results reported in [2, 4].

REFERENCES

1. K. Okuno, T. Uda, S. O'Hira, and Y. Naruse, J. Nucl. Sci. Technol. **28**, 509 (1991).

2. K. Kalli, A. Othonos, and C. Christofides, Rev. Sci. Instrum. **68**, 3544 (1997).

3. P. R. Regnier and J. P. E. Taran, Appl. Phys. Lett. **23**, 240 (1973).

4. A. A. Ivanov, G. A. Polyakov, and V. B. Voronin, Izv. Ross. Akad. Nauk, Ser. Fiz. **57** (2), 165 (1993).

5. G. M. Mikheev and T. N. Mogileva, Kvantovaya Élektron. (Moscow) **23**, 943 (1996) [Quantum Electron. **26**, 919 (1996)].

6. Gen. M. Mikheev, Georg. M. Mikheev, T. N. Mogileva, and D. G. Kalyuzhnyĭ, Kvantovaya Élektron. (Moscow) **32**, 39 (2002) [Quantum Electron. **32**, 39 (2002)].

7. S. A. Akhmanov and N. I. Koroteev, *Methods of Nonlinear Optics in the Light Scattering Spectroscopy* (Nauka, Moscow, 1981).

8. A. D. May, V. Degen, J. C. Stryland, and H. L. Welsh, Can. J. Phys. **39**, 1769 (1961).

9. J. Ph. Berger, R. Saint-Loup, H. Berger, *et al.*, Phys. Rev. A **49**, 3396 (1994).

10. P. M. Sinclair, J. Ph. Berger, X. Michaut, *et al.*, Phys. Rev. A **54**, 402 (1996).

11. G. M. Mikheev, T. N. Mogileva, A. Yu. Popov, and D. G. Kalyuzhnyĭ, Prib. Tekh. Éksp., No. 2, 101 (2003) [Instrum. Exp. Tech. **46**, 233 (2003)].

Translated by P. Pozdeev

The Spatiotemporal Field of Turbulent Flow Pulsation

L. N. Pyatnitsky

Associated Institute for High Temperatures, Russian Academy of Sciences, Moscow, Russia
e-mail: pyat7@mail.ru
Received June 6, 2003

Abstract—Relations describing the spatiotemporal field of pulsation of the hydrodynamic parameters of a turbulent flow have been derived based on the wave model of turbulence. The process of chaotization of the pulsation field is analyzed. The results of calculations of the longitudinal and transverse velocity pulsation components are compared to the results of measurements reported by H. Reichardt. © 2003 MAIK "Nauka/Interperiodica".

Previously [1–3], a new concept of turbulence has been experimentally justified, a mechanism of the turbulent flow pulsation has been considered, and the formation of a turbulent boundary layer and a laminar sublayer has been described. The pulsation of flow parameters results from the superposition of perturbations arising (in the form of excessive pressure centers) at the wall in the field of the flow velocity gradient and propagating as wave packets.

Within a wave packet, $|l - ct| \le a$, the pulsation of velocity u and other parameters is described by the pressure distribution function $f(r)$ in a primary perturbation with a characteristic size of $2a$ and by the distance l traveled by the wave for the time t:

$$u, p, \rho \sim f(l - ct)/l. \qquad (1)$$

The flow core features the superposition of wave packets of a nearly spherical shape. At the wall, where the flow velocity exhibits a strong gradient, the wave front of a packet is broken and the character of pulsation is changed. The region of the wave front breakage is interpreted as a boundary, the height of which determines the characteristic size of a primary perturbation. Upon the wave reflection, the velocity pulsation in the wave packet near the wall ceases and the energy is transferred to the oscillations of the other parameters. This region is interpreted as a laminar sublayer of the turbulent boundary layer.

This paper presents the relations describing the spatiotemporal field of pulsation of the hydrodynamic parameters of a turbulent flow and the process of chaotization of this pulsation field. The results of calculations of the longitudinal and transverse velocity pulsation components are compared to the results of measurements performed by H. Reichardt.

The direction of wave propagation at a given point in the flow velocity field U is determined by a unit vector **s**, which is equivalent to an acoustic ray in terms of the geometric acoustics. The behavior of this vector is described by the equation [4]

$$\frac{d\mathbf{s}}{dl} = \frac{1}{c}[\mathrm{rot}\, U, \mathbf{s}]. \qquad (2)$$

Consider a flow directed along the x axis of a flat channel of height $z = d$ and let us evaluate the total change in the vector **s** orientation in the velocity field $U(z)$ by calculating the polar (ϑ) and azimuthal (φ) direction angles of the vector. Integrating Eq. (2), we obtain (for $M = U/c \ll 1$):

$$\left.\begin{aligned}
\sin\vartheta &= \sqrt{\sin^2\vartheta_0 + 2M(z)\sin\vartheta_0\cos\varphi_0 + M^2(z)}, \\
\sin\varphi &= \frac{\sin\vartheta_0\sin\varphi_0}{\sqrt{\sin^2\vartheta_0 + 2M(z)\sin\vartheta_0\cos\varphi_0 + M^2(z)}}.
\end{aligned}\right\} \quad (3)$$

The obtained solution (3) presents the direction angles $\{\vartheta, \varphi\}$ of vector **s** as functions of the initial orientation $\{\vartheta_0, \varphi_0\}$, the coordinate z, and the distribution $M(z)$. Once the orientation $\{\vartheta, \varphi\}$ is known, the trajectory of the given point of the wave in the channel can be calculated. To this end, the coordinates of this point $\{\xi, \eta, \zeta\}$ are determined as functions of the pathlength l during the wave travel in the half-space above the lower wall. According to formulas (3), the position of this point relative to the wave center is described by a system of parametric differential equations

$$\left.\begin{aligned}
\frac{d\xi}{dl} &= \sin\vartheta_0\cos\varphi_0 + M(z); \\
\frac{d\eta}{dl} &= \sin\vartheta_0\sin\varphi_0; \\
\frac{d\zeta}{dl} &= \sqrt{\cos^2\vartheta_0 - 2M(z)\sin\vartheta_0\cos\varphi_0 - M^2(z)}; \\
\xi(0) &= \eta(0) = \zeta(0) = 0.
\end{aligned}\right\} \quad (4)$$

In describing the wave configuration in the coordinates $\{x, y, z\}$ related to the channel frame, we should take into account that a perturbation can arise at an arbitrary point $\mathbf{rp}\{xp, yp, zp\}$ on any wall, with a delay of tp relative to $t = 0$. Let us use the dimensionless variables, representing distances in fractions of the channel height d and times in the d/c scale. The number of wave reflections n from the walls can be expressed through the ordinate ζ as $n = \text{In}(\zeta)$, where In is the operation of taking the integer part, and the system of equations (4) can be rewritten as

$$
\left.
\begin{aligned}
x &= xp = \int_0^{l-tp} (\sin\vartheta_0 \cos\varphi_0 + M(z))\,dl, \\
y &= yp + \sin\vartheta_0 \sin\varphi_0 (l - tp), \\
z &= zp + \int_0^{l-tp} \left(\sqrt{\cos^2\vartheta_0 - 2M(z)\sin\vartheta_0\cos\varphi_0 - M^2(z)} \right. \\
&\quad \left. - 2\text{In}\left[\frac{n+1}{2}(-1)^{n+zp} \right] \right)dl, \\
n &= \text{In}[(l - tp)\sqrt{\cos^2\vartheta_0 - 2M(z)\sin\vartheta_0\cos\varphi_0 - M^2(z)}].
\end{aligned}
\right\}
\quad (5)
$$

For the sequences of parameters $\mathbf{rp}$ and tp, the joint solution of Eqs. (5) and (1) yields the spatiotemporal field of pulsation of the flow parameters in the channel. Attenuation of the wave upon reflection from the walls is described in (1) by the coefficient $(1 - \alpha)^n$. The field can be calculated using modern mathematical program packages such as Mathematica 4.

Figures 1a and 1b present the patterns of perturbations in the flow velocity for $l = 0.2$ and 2.2, respectively (the wave front and the velocity pulsation vectors are shown in the plane $y = 0$; the space outside the channel is shadowed; the length of the velocity vector corresponds to the pulsation amplitude). As the wave propagates, the amplitude gradually decreases, while the spatiotemporal field of pulsation remains determined and quite regular.

In the initial stage featuring the propagation of seven waves for $l = 0.3$ (Fig. 1c, wave fronts are not shown), the perturbation field is still regular, but the pattern of pulsation observed for $l = 2.2$ (Fig. 1d) appears as chaotic. An analysis of the corresponding spectra indicates a stochastic character of pulsation, which becomes random only for the random sequences of parameters $\mathbf{rp}$ and tp.

According to formulas (3), the trajectory of vector $\mathbf{s}$ in the field $M(z)$ deviates from a straight line. This deviation depends on the pathlength l traveled by the vector in the layer of strong velocity gradient with the thickness δ. In the direction of large angles ϑ_0 (at the channel
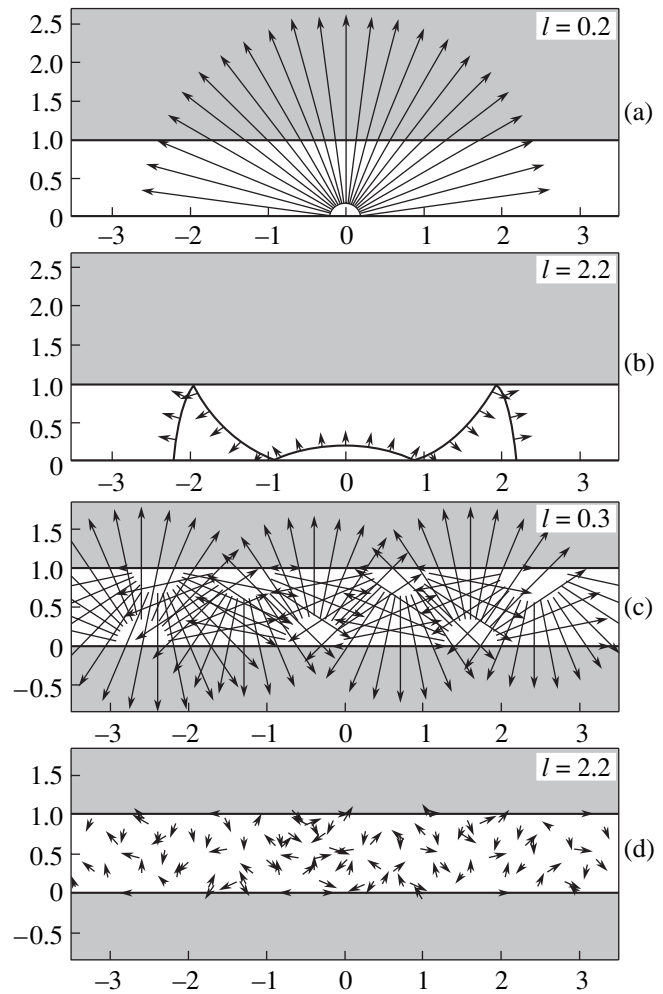
Fig. 1. Schematic diagrams showing the field of velocity pulsation in the plane $y = 0$ for various values of l.

wall), the pathlength rapidly grows with the angle as $l_0 = \delta/\cos\vartheta_0$ (the growth rate sharply increases with the degree of deviation from the straight line, $l > l_0$). As a result, the ratio of the longitudinal velocity pulsation component to the transverse one (u_x/u_z) must increase on approaching the boundary layer zone.

This very trend was experimentally observed by Reichardt [5] for flows in a channel and by Klebanoff [6] in experiments with a plate (see also [7, Ch. 18]). In particular, the turbulent pulsation in an air flow in the experiments of Reichardt [5] was measured in a 1-m-wide channel with a height of 24.4 cm at a Mach number of $M_0 = 0.003$ (flow velocity, $U_0 = 100$ cm/s) and a Reynolds number exceeding 10^4. Figure 2a shows the experimental distributions of longitudinal ($\sqrt{\overline{u^2}}$) and transverse ($\sqrt{\overline{w^2}}$) rms velocity pulsation components for the channel halfwidth. The data are normal-
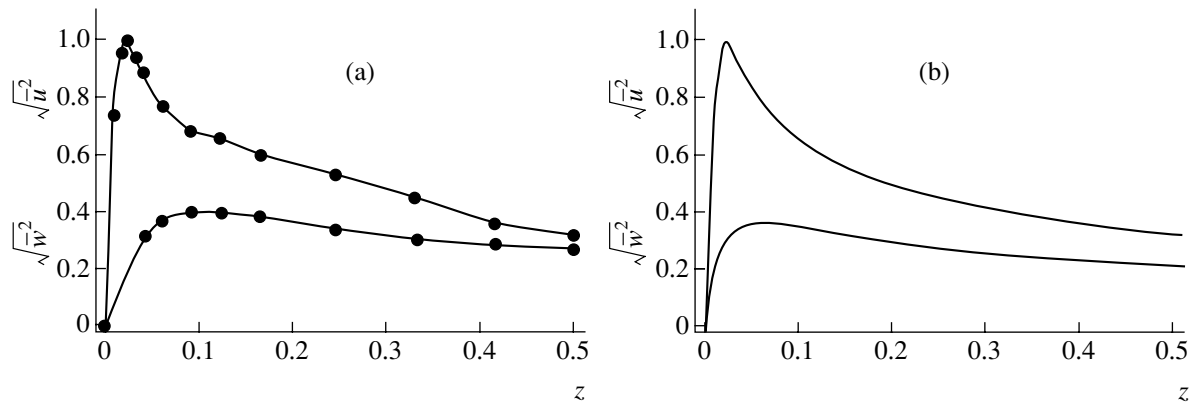
Fig. 2. Longitudinal ($\sqrt{\overline{u^2}}$) and transverse ($\sqrt{\overline{w^2}}$) rms velocity pulsation profiles in a channel: (a) experimental data of Reichardt [5]; (b) calculation using the simplified scheme.

ized to the maximum longitudinal pulsation component $(\sqrt{\overline{u^2}})_{max}$.

An analysis of the results of measurements shows that the transverse velocity pulsation component relatively weakly depends on z, while the longitudinal component exhibits a pronounced maximum at a distance of $\delta \approx 0.03$ from the wall. This result (not given proper explanation) is naturally interpreted based on the wave mechanism of the turbulent flow pulsation. Moreover, it is possible to provide for a quantitative description of the pulsation components within the framework of this mechanism.

Using relations (1), the velocity pulsation components can be expressed as

$$u \sim f\left(\frac{l_n - l}{a}\right)\sin(\vartheta)/l, \quad w \sim f\left(\frac{l_n - l}{a}\right)\cos(\vartheta)/l, \quad (6)$$

where l is the distance traveled by the wave, l_n is the distance to the point of observation, ϑ is the angle of ray slope at this point, and $a = \delta$ is a characteristic size of the primary perturbation. The values of pulsation components can be calculated by solving the system of equations (5) and (6). In order to demonstrate possibilities of the proposed method, the calculation scheme will be simplified so as to obtain analytical expressions.

To this end, the arc-like trajectories of vectors **s** coming to the observation point $\{x = 0, z\}$ from the perturbation centers xp are replaced by the straight line connecting these points. The xp distribution is assumed to be uniform along x and the initial perturbations are localized within the region of $xp \in [-10, 10]$. Outside this region, the velocity pulsation amplitude decreases by a factor of more than $(xp/\delta) = 330$ and can be

neglected. The dependence of the rms velocity pulsation components on the coordinate z is determined by expressing the variables in (6) through xp and z:

$$\sqrt{\overline{u^2}} \sim \sqrt{2\left(\int_0^{10}\left(\frac{(1 + \varepsilon)xp}{xp^2 + (z + a)^2}\right)^2 d(xp)\right)},$$

$$\sqrt{\overline{w^2}} \sim \sqrt{2\left(\int_0^{10}\left(\frac{(1 - \varepsilon)xp}{xp^2 + (x + a)^2}\right)^2 d(xp)\right)}.$$

(7)

Here, the coefficient ε compensates for the distortion of pulsation contributions as a result of the trajectory bending. In the denominator, the parameter a reflects the fact that formulas (6) are valid only outside the boundary layer; Eqs. (5) should be integrated in the half-space $z > a$. The plots were constructed taking into account that, within the primary perturbation region, the velocity field is determined using the Green's function of the boundary value problem for the wave equation (the pulsation amplitude decays from the maximum value at $z = 0$ to zero at $z = l = 0$).

Figure 2b shows the pulsation components calculated using formulas (7) with $\varepsilon = 0.2$. A comparison between Figs. 2a and 2b shows that the proposed model provides for a quite satisfactory description of the experimental results of H. Reichardt. In these experiments, the u/U ratio amounted to 10^{-4}. In an acoustic wave, the amplitudes of oscillations in the velocity (u) and pressure (p) are related as $u/c = p/p_0$ [4], from which it follows that $p/p_0 \approx 10^{-4}$. For air at atmospheric pressure ($p_0 \sim 10^5$ Pa), this yields $p \approx 10$ Pa (~0.1 Torr). The obtained values of $u \sim 5$ cm/s and $p \approx 10$ Pa are by no means unusual. The acoustic waves with pulsation amplitudes on this level are produced by human voice,

which confirms the role of acoustic waves in the formation of turbulent flow pulsation fields.

REFERENCES

1. L. N. Pyatnitskiĭ, Zh. Éksp. Teor. Fiz. **113**, 191 (1998) [JETP **86**, 107 (1998)].

2. L. N. Pyatnitskiĭ, Zh. Éksp. Teor. Fiz. **119**, 665 (2001) [JETP **92**, 576 (2001)].

3. L. N. Pyatnitskiĭ, Pis'ma Zh. Tekh. Fiz. **29** (9), 9 (2003) [Tech. Phys. Lett. **29** (2003) (in press)].

4. L. D. Landau and E. M. Lifshitz, *Fluid Mechanics,* 2nd ed. (Nauka, Moscow, 1986; Pergamon Press, Oxford, 1987).

5. H. Reichardt, Naturwissenschaften **26**, 404 (1938).

6. P. S. Klebanoff, *Characteristics of Turbulence in Boundary Layer with Zero Pressure Gradient*, NACA Rep. 1247 (1955), p. 19, Supersedes NACA Technical Note 3178.

7. H. Schlichting, *Boundary Layer Theory* (McGraw-Hill, New York, 1968; Nauka, Moscow, 1974).

Translated by P. Pozdeev

The Energy Spectra of Clusters
Formed during Ion Sputtering of Metals

V. I. Matveev[a],* and S. A. Kochkin[b]

[a] *Pomorskiĭ State University, Arkhangelsk, Russia*
[b] *Arkhangelsk State University, Arkhangelsk, Russia*
* *e-mail: matveev.victor@pomorsu.ru*
Received May 14, 2003

Abstract—We propose a method for calculating the energy spectra of neutral and charged clusters with the number of atoms $N \geq 5$ sputtered from a metal surface during ion bombardment. The calculated energy distributions of clusters emitted from tantalum and niobium bombarded with atomic gold ions are compared to the published experimental data. © *2003 MAIK "Nauka/Interperiodica".*

In many cases [1–5], experimental investigations of the process of ion sputtering of solids in the form of clusters are aimed at elucidating the mechanisms responsible for the presence of polyatomic particles in the sputtered products. As a rule (see, e.g., [6–11]) such experiments involve the measurements of energy spectra and size distributions of neutral and singly-charged clusters for various targets and the ion beam compositions and currents. These data, as well as the yields of neutral and charged clusters depending on the target temperature [8], provide detailed information about the mechanisms of cluster formation. Theoretical description of the process of cluster emission in the course of ion sputtering is a difficult task, primarily because of an essentially multiparticle character of the problem. Calculations using the methods of molecular dynamics [1] encounter considerable technical difficulties rapidly growing with the number of atoms in the clusters. Such simulations can hardly be reproduced by researchers other than the authors of a particular computational scheme. The difficulties additionally increase when processes determining the charge composition of the sputtered products are included into the molecular dynamics scheme (see, e.g., review [5]).

In this paper, we propose a method for calculating the energy spectra of large neutral and charged clusters (with the number of atoms $N > 5$) sputtered from a metal surface during ion bombardment. The approach is based on the physical notions formulated in [12–15] and the method [15] developed for calculating the total cluster yield.

Let us consider a solid composed of atoms, each atom oscillating in a potential well of depth Δ at a natural frequency ω (the characteristic oscillation period being $T = 2\pi/\omega$). Let the impinging ions possess a velocity such that both the primary ions and fast recoil atoms moving in a metal target experience a large number of collisions during the time period $\tau \ll T$, as a result

of which atoms of the metal target acquire the momenta $\mathbf{q}_i$, i being the atom number. According to [15], the probability for a cluster of N atoms to be emitted as a whole with a momentum $\mathbf{k}$ is

$$
W_{\mathbf{k}} = \left| \left\langle \Phi_{\mathbf{k}}(\mathbf{R}) \left| \exp\left(\frac{i}{\hbar} \sum_{i=1}^{N} \mathbf{q}_i \mathbf{R} \right) \right| \Phi_0(\mathbf{R}) \right\rangle \right|^2
$$
$$
\times \exp\left(-\frac{1}{n_0} \frac{1}{2\hbar^2 \alpha^2} \sum_{i=1}^{N} \mathbf{q}_i^2 \right), \tag{1}
$$

where $\alpha^2 = m\omega/\hbar$, m is the mass of one atom, $\hbar$ is the Planck constant, $n_0 \approx \Delta/\hbar\omega$, $\Phi_0(\mathbf{R})$ is the wave function of the center of mass of the block of N atoms in the ground state, $\Phi_{\mathbf{k}}(\mathbf{R})$ is the wave function of the center of mass of the same block in the state of continuum with the momentum $\mathbf{k}$, and $\mathbf{R}$ is the radius-vector representing the coordinates of the center of mass.

The center of mass of a block of N atoms in the metal is assumed to perform harmonic oscillations at a frequency Ω in a potential well with the depth U_N that has a meaning of the binding energy between cluster and metal. This binding energy is proportional to the contact area S_N between a block of N atoms and the rest of the metal. In terms of [12–15], $U_N = \sigma S_N = \delta N^{2/3}$, where δ has a meaning of the cluster binding energy per atom (generally speaking, δ differs from Δ—the potential well of each individual atom in the solid). Thus, we consider the center of mass of a block of N atoms as occurring in a spherically symmetric oscillator potential truncated at a height of U_N. This potential can be

expressed as $U(\mathbf{R}) = \dfrac{Nm\Omega^2}{2} \mathbf{R}^2$ for $R < R_N$ (R_N corresponds to $U(\mathbf{R}_N) = U_N$) and has a constant value $U(\mathbf{R}) = U_N$ for $R > R_N$.

Prior to being sputtered, the center of mass of a given block occurs in the ground state $\Phi_0(\mathbf{R})$ in the potential $U(\mathbf{R})$. The wave function $\Phi_{\mathbf{k}}(\mathbf{R})$ of the center of mass in the state of continuum with the momentum $\mathbf{k}$ and the energy $E_c + U_N$ ($E_c = \mathbf{k}^2/(2mN)$) in the same potential $U(\mathbf{R})$ can be written in quasiclassical form as

$$\Phi_{\mathbf{k}}(\mathbf{R}) = \frac{A}{(2\pi\hbar)^{3/2}} \exp\left(\frac{i}{\hbar}\int \mathbf{k}(\mathbf{R})d\mathbf{R}\right), \qquad (2)$$

where $|\mathbf{k}(\mathbf{R})| = \sqrt{2mN(E_c + U_N - U(\mathbf{R}))}$ and $\mathbf{k}(\mathbf{R}) \longrightarrow \mathbf{k}$ as $\mathbf{R} \longrightarrow \infty$.

Following [15], we assume that the potential well $U(\mathbf{R})$ is sufficiently deep to obey the condition $\hbar\Omega \ll U_N$. This implies that $U(\mathbf{R}) \ll U_N$ on the scale of the ground state $\Phi_0(\mathbf{R})$ and, in calculating the matrix element $\langle\Phi_{\mathbf{k}}(\mathbf{R})|\exp(i\sum_i \mathbf{q}_i \mathbf{R}/\hbar)|\Phi_0(\mathbf{R})\rangle$ for Eq. (1), we may take the momentum in the state $\Phi_{\mathbf{k}}(\mathbf{R})$ to be $|\mathbf{k}(\mathbf{R})| = \sqrt{2mN(E_c + U_N)} = |\mathbf{k}(0)|$. This yields

$$W_{\mathbf{k}} = |A^2|\frac{1}{(2\pi\eta\hbar^2)^{3/2}}$$

$$\times \exp\left(-\frac{\left(\sum_{i=1}^N \mathbf{q}_i - \mathbf{k}(0)\right)^2}{2\eta\hbar^2}\right) \exp\left(-\frac{1}{n_0}\frac{1}{2\hbar^2\alpha^2}\sum_{i=1}^N (\mathbf{q}_i)^2\right), \qquad (3)$$

where $\eta = mN\Omega/(2\hbar)$. The probability (3) should be averaged over all possible $\mathbf{q}_i$ ($i = 1, 2, .., N$). A natural assumption concerning the distribution of $\mathbf{q}_i$ is that all these vectors are independent and all their orientations are equiprobable, so that the averaging can be performed, as it was done in [15], over the angles Ω_{qi} of the $\mathbf{q}_i$ vectors. The calculation can be significantly simplified by assuming that all $\mathbf{q}_i$ possess equal lengths $|\mathbf{q}_i| = q$ and are randomly oriented in space. As a result, the average probability for $N \gg 1$ takes the form (cf. [15])

$$\overline{W}_{\mathbf{k}} = A^2 \frac{1}{2^3\pi^{3/2}} \frac{1}{(\eta\hbar^2/2 + Nq^2/6)^{3/2}}$$

$$\times \exp\left(\frac{\mathbf{k}^2(0)}{4(\eta\hbar^2/2 + Nq^2/6)}\right) \exp\left(-\frac{1}{n_0}\frac{Nq^2}{2\hbar^2\alpha^2}\right), \qquad (4)$$

where q has a meaning of the average momentum transfer and is the only variable parameter in the theory [15].

The total probability $\overline{W}_N$ of finding the center of mass in a continuous spectrum can be determined by integrating $\overline{W}_{\mathbf{k}}$ over all $\mathbf{k}$. To this end, the integration

element d^3k can be represented as $d^3\mathbf{k} = 4\pi k^2 dk = 4\pi mN\sqrt{2mN(E_c + U_N)}\, dE_c$ that yields

$$\overline{W}_N = \int \overline{W}_{\mathbf{k}} d^3k = \int_0^\infty \frac{d\overline{W}_N}{dE_c} dE_c. \qquad (5)$$

Here, $\dfrac{d\overline{W}_N}{dE_c}$ is the energy spectrum of clusters consisting of N atoms:

$$\frac{d\overline{W}_N}{dE_c} = |A|^2 \frac{2}{\sqrt{\pi}} \frac{(E_c + U_N)^{1/2}}{\varepsilon^{3/2}} \exp\left(-N\frac{3}{2}\frac{\varepsilon}{\Delta} - \frac{E_c + U_N}{\varepsilon}\right), \qquad (6)$$

where $\varepsilon = \dfrac{2}{3}\dfrac{q^2}{2m}$ and $U_N = \delta N^{2/3}$. Requiring that the probability $\overline{W}_N$ would coincide with the value obtained previously [15] by summing over all bound states $\Phi_n(\mathbf{R})$ of the center of mass and subtracting the result from unity,

$$\overline{W}_N = \left[1 - \left(1 + \frac{\varepsilon}{U_N}\right)^{-3/2}\right]\exp\left(-N\frac{3}{2}\frac{\varepsilon}{\Delta}\right), \qquad (7)$$

we determine the amplitude $|A|^2$:

$$|A|^2 = \frac{\sqrt{\pi}}{2}\left[1 - \left(1 + \frac{\varepsilon}{U_N}\right)^{-3/2}\right]\Gamma^{-1}\left(\frac{3}{2}, \frac{U_N}{\varepsilon}\right), \qquad (8)$$

where $\Gamma^{-1}(x, y) = 1/\Gamma(x, y)$ and $\Gamma(x, y)$ is the incomplete gamma-function. Strictly speaking, this procedure of determining $|A|^2$ is consistent for $U_N/\varepsilon \longrightarrow 0$ and can be additionally justified by the coincidence of the $\overline{W}_N$ values calculated as an integral (5) over continuum and as a sum (7) over the bound states.

In order to determine the energy spectrum of clusters with allowance of their charges, we also use the physical notions formulated in [12–15], according to which the process of charged state formation is considered as a part of the sputtering mechanism. According to [15], the probability $P_N(Q)$ that a sputtered cluster of N atoms would possess a charge Qe (e being the electron charge) is determined using a standard formula for the probability of fluctuations

$$P_N(Q) = \frac{1}{D_N}\exp\left\{-\frac{1}{2}\frac{Q^2}{(\Delta Q_N)^2}\right\}, \qquad (9)$$

$$(\Delta Q_N)^2 = \frac{3^{1/2}}{\pi^{4/3}}\frac{m_e\vartheta}{\hbar^2}\left(\frac{V}{N}\right)^{2/3}\gamma^{1/3}N.$$

Here D_N is the normalization factor determined by summation over all possible values of $Q = 0, \pm1, \pm2, \ldots$; $\overline{(\Delta Q_N)^2}$ is the mean square deviation of the cluster
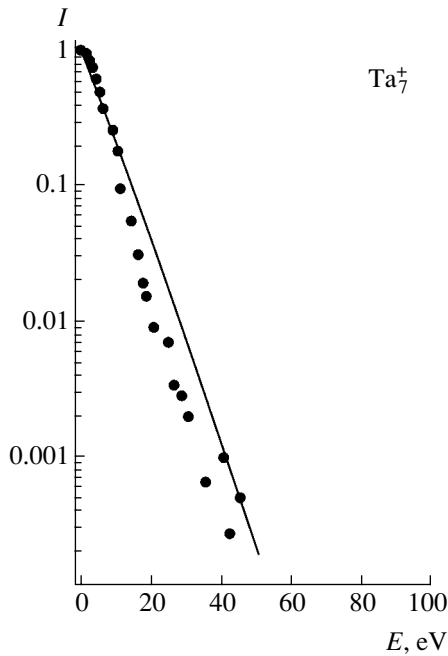
Fig. 1. The energy spectrum I_7^1 of singly-charged tantalum clusters Ta_7^1 containing $N = 7$ atoms, sputtered from a tantalum target bombarded with singly-charged 6-keV Au^{-1} ions. Solid curve presents the results of calculation for the parameter $q = 450$ at. units ($\hbar = m_e = e = 1$); points show the experimental data from [16].
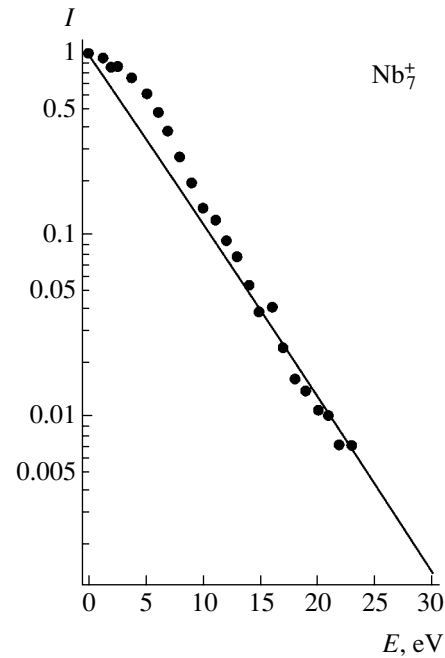
Fig. 2. The energy spectrum I_7^1 of singly-charged niobium clusters Nb_7^1 containing $N = 7$ atoms, sputtered from a niobium target bombarded with singly-charged 6-keV Au^{-1} ions. Solid curve presents the results of calculation for the parameter $q = 285$ at. units ($\hbar = m_e = e = 1$); points show the experimental data from [7].

charge from the equilibrium value; m_e is the effective mass of the conduction electron; V is the cluster volume; ϑ is the target temperature; and γ is the valence of metal atoms.

Finally, to determine the energy spectrum dW_N^Q/dE_c of the clusters containing N atoms and possessing the charge Qe, the spectrum $d\overline{W}_N/dE_c$ in (5) has to be multiplied by $P_N(Q)$. The resulting expression for the energy spectrum is

$$\frac{dW_N^Q}{dE_c} = \frac{(E_c + U_N)^{1/2}}{\varepsilon^{3/2}\Gamma\left(\frac{3}{2}, \frac{U_N}{\varepsilon}\right)}\left[1 - \left(1 + \frac{\varepsilon}{U_N}\right)^{-3/2}\right]$$

$$\times \exp\left(-N\frac{3}{2}\frac{\varepsilon}{\Delta} - \frac{E_c + U_N}{\varepsilon}\right)\frac{1}{D_N}\exp\left\{-\frac{1}{2}\frac{Q^2}{(\Delta Q_N)^2}\right\}. \tag{10}$$

It should be noted that the energy spectra (10) (as well as the total probabilities W_N^Q, see [15] and the experimental data in [8]) of the neutral clusters are independent of the target temperature, whereas the spectra of charged clusters are strongly temperature-dependent. However, as the temperature increases, the latter spectra approach those of the neutral clusters.

In experiment, it is a usual practice to measure the relative energy spectra of clusters with various numbers of atoms. In order to compare such data to the calculated spectrum (10), the latter should be appropriately normalized (after which any convenient units can be employed). Figures 1 and 2 present the energy spectra $I_N^Q = (dW_N^Q/dE_c)/(dW_N^Q/dE_c)|_{E_c = 0}$ (normalized to unity at $E_c = 0$) of singly-charged (I_N) clusters of tantalum (Ta_N) and niobium (Nb_N) with $N = 7$ for the corresponding metal targets sputtered with 6-keV Au^{-1} ions. It should be noted that this normalization, albeit convenient in experiment, leads to some "impoverishment" of the information gained (in particular, the temperature dependence according to (10) is lost). For the comparison, Figs. 1 and 2 present the experimental data taken from [16, 7]. In the calculation, the number of fitting parameters was reduced by assuming that $\Delta = \delta = 8.1$ eV (the energy of sublimation) for tantalum and $\Delta = \delta = 7.47$ eV for niobium [17].

REFERENCES

1. *Basic and Applied Aspects of Solid Sputtering: Collection of Articles*, Ed. by E. S. Mashkova (Mir, Moscow, 1989).

2. H. H. Andersen, K. Dan. Vidensk. Selsk. Mat. Fys. Medd. **43**, 127 (1993).

3. H. M. Urbassek and W. O. Hofer, K. Dan. Vidensk. Selsk. Mat. Fys. Medd. **43**, 97 (1993).

4. I. A. Baranov, Yu. V. Martynenko, S. O. Tsepelevich, and Yu. N. Yavlinskiǐ, Usp. Fiz. Nauk **156**, 478 (1988) [Sov. Phys. Usp. **31**, 1015 (1988)].

5. *Sputtering by Particle Bombardment*, Ed. by R. Behrisch and K. Wittmaak (Springer-Verlag, New York, 1996; Mir, Moscow, 1998).

6. Th. J. Colla, H. M. Urbassek, A. Wucher, *et al.*, Nucl. Instrum. Methods Phys. Res. B **143**, 284 (1998).

7. S. F. Belykh, B. Habets, U. Kh. Rasulev, *et al.*, Nucl. Instrum. Methods Phys. Res. B **164**–**165**, 809 (2000).

8. C. Staudt, R. Heinrich, P. Mazarov, *et al.*, Nucl. Instrum. Methods Phys. Res. B **164**–**165**, 715 (2000).

9. R. Kissel and H. M. Urbussek, Nucl. Instrum. Methods Phys. Res. B **180**, 293 (2001).

10. S. F. Belykh, V. V. Palitsin, I. V. Veryovkin, *et al.*, Nucl. Instrum. Methods Phys. Res. B **203**, 164 (2003).

11. S. N. Morozov and U. Kh. Rasulev, Nucl. Instrum. Methods Phys. Res. B **203**, 192 (2003).

12. V. I. Matveev and P. K. Khabibullaev, Dokl. Akad. Nauk **362**, 191 (1998) [Dokl. Phys. **43**, 544 (1998)].

13. S. F. Belykh, V. I. Matveev, I. V. Veryovkin, *et al.*, Nucl. Instrum. Methods Phys. Res. B **155**, 409 (1999).

14. V. I. Matveev, Zh. Tekh. Fiz. **70** (8), 108 (2000) [Tech. Phys. **45**, 1063 (2000)].

15. V. I. Matveev, Zh. Tekh. Fiz. **72** (6), 115 (2002) [Tech. Phys. **47**, 767 (2002)].

16. S. F. Belykh, U. Kh. Rasulev, A. V. Samartsev, and I. V. Veryovkin, Nucl. Instrum. Methods Phys. Res. B **136**–**138**, 773 (1998).

17. C. Kittel, *Introduction to Solid State Physics* (Wiley, New York, 1976; Nauka, Moscow, 1978).

Translated by P. Pozdeev

Radiation-Stimulated Processes
in CdTe Solar Cells

Zh. Zhanabergenov, Sh. A. Mirsagatov, and S. Zh. Karazhanov

Physicotechnical Institute, Academy of Sciences of the Republic of Uzbekistan,
Tashkent, Uzbekistan
Received June 3, 2003

Abstract—The parameters of polycrystalline cadmium telluride (CdTe) solar cells exhibit nonmonotonic variation with increasing dose of γ radiation. It is established that this behavior is related to a nonmonotonic dose dependence of the minority carrier lifetime in the base region. The short circuit current, the fill factor, and the conversion efficiency of γ-irradiated CdTe solar cells can be greater than the analogous parameters of unirradiated devices. © *2003 MAIK "Nauka/Interperiodica".*

As is known, irradiation can significantly modify the electrical properties of semiconductor devices. For example, a nonmonotonic dose dependence was reported for the short circuit current (J_{sc}) of germanium-based [1] and silicon-based [2–4] solar cells and the collector current of CdTe-based bipolar phototransistors [5]. In addition, J_{sc} exhibited a nonmonotonic variation depending on the deep trap concentration (N_t) determined by theoretical analysis of a contribution of the impurity photovoltaic effect to the photoelectric conversion efficiency [6, 7]. One of the main results of such investigations was the establishing of the fact that J_{sc} increases and V_{oc} (the open circuit voltage) decreases in response to a monotonic increase in the concentration of deep defects. The solar cell efficiency (η) can decrease (increase) with increasing N_t, provided that the drop related to a decrease in V_{oc} is greater (smaller) then the growth related to an increase in J_{sc}. The cases of drop and growth of η depending on the deep impurity concentration in silicon-based solar calls were reported in [2–4] and [8], respectively.

In this paper, we present the experimental data for polycrystalline CdTe solar cells, showing evidence for a possible growth in their conversion efficiency with increasing concentration of deep defects according to a theoretical model developed in [8].

The experiments were performed with p-CdTe/n-CdTE/n-CdS solar cells with a base resistivity of ρ ≈ 10^3–10^5 Ω cm and a working area of 1 cm² obtained using a technology described elsewhere [10]. The film thicknesses were about $d \sim 50$ μm. The initial CdTe films possessed a polycrystalline structure, representing grains composed of columnar microcrystals oriented in the growth direction and disoriented with respect to the azimuth angle. The grain size was within

100–150 μm, which implies that the grains extend over the whole film thickness. The samples were irradiated at $T = 50°$C with γ quanta of $E \approx 1.2$ MeV energy from a Co⁶⁰ source at a rate of 1700 rad/s in a range of doses $\leq 1.6 \times 10^{18}$ cm⁻².
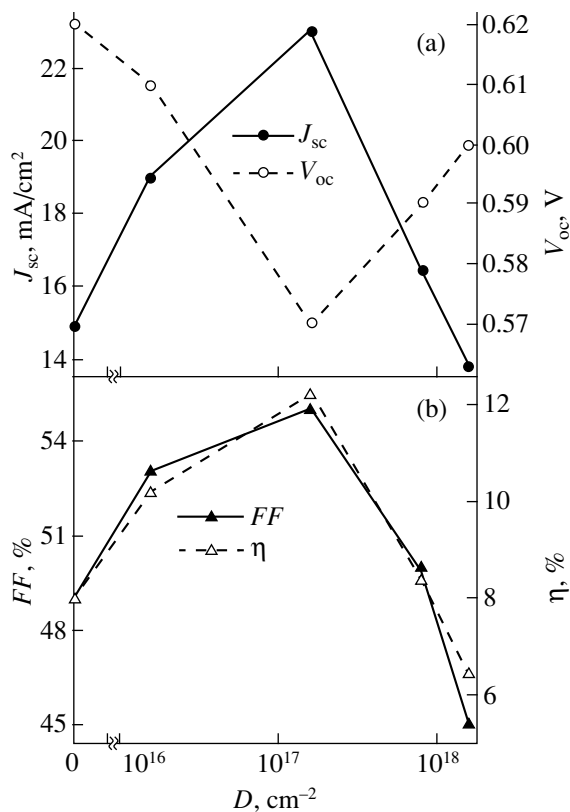
Fig. 1. Plots of (a) the short circuit current J_{sc} and open circuit voltage V_{oc} and (b) the fill factor *FF* and conversion efficiency η of polycrystalline CdTe solar cells versus the dose of γ radiation.

Figure 1 shows the dose dependence of the short circuit current (J_{sc}), the open circuit voltage (V_{oc}), the fill factor (FF) and the efficiency (η) for the CdTe solar cells studied. As can be seen, all these parameters exhibit a nonmonotonic variation with monotonically increasing γ radiation dose D. It is also seen that J_{sc}, FF, and η of the unirradiated solar cells are smaller than the analogous values in the region of doses $D \le 8 \times 10^{17}$ cm^{-2}. The behavior observed for the CdTe solar cells basically differs from that of the silicon-based devices [2–4], for which the properties of irradiated samples in the entire dose range were lower as compared to the values prior to irradiation. However, the data of Baruch [1] concerning an increase in the J_{sc} of germanium-based solar cells upon irradiation are consistent with our results. To the best of our knowledge, the observed growth in the η value with increasing N_t is the first experimental evidence in favor of the theoretical model proposed in [8], according to which the growth in the efficiency due to an increase in J_{sc} predominates over the drop in η related to a decrease in V_{oc}.

It should be noted that, in contrast to the case of single crystal germanium-based [1] and silicon-based [2–4] solar cells, the parameters of polycrystalline CdTe solar cells increase or decrease in a rather broad range of radiation doses and in a smoother manner. This implies a more stable character of the aforementioned dependences.

Following [7–9], we may suggest that the increase in J_{sc}, FF, and η with the irradiation dose D is related to an increase in the minority carrier lifetime τ_p in the base region caused by a growth in the degree of compensation. This hypothesis is confirmed by a dose dependence of the dark resistivity ρ presented in Fig. 2. As can be seen from these data, the $\rho(D)$ curve is also nonmonotonic and exhibits correlation with the plots of $J_{sc}(D)$, $FF(D)$, and $\eta(D)$ curves in Fig. 1. Therefore, we may conclude that γ radiation produces recharge of the defect states, thus increasing the degree of compensation and leading to nonmonotonic variation of the CdTe solar cell parameters.

The fact of an increase in the degree of compensation is also confirmed by data on the effect of γ radiation on the capacitance–voltage characteristic $C(V)$ of a metal–oxide–semiconductor (MOS) structure based on large-block p-CdTe films prepared using a technology described in [11]. The characteristics obtained by numerical modeling prior to exposure and after irradiation to a dose of $D = 1.6 \times 10^{16}$ or 1.6×10^{17} cm^{-2} (case 1) are shifted to the right from the experimental $C(V)$ curves, while the characteristic corresponding to a radiation dose of $D = 8 \times 10^{17}$ cm^{-2} (case 2) is shifted to the left from the experimental $C(V)$ curve. From this we conclude that, in case (1), the oxide–semiconductor
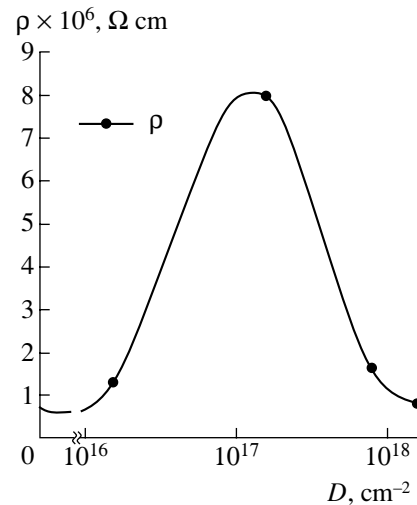
Fig. 2. The dose dependence of the resistivity of γ-irradiated polycrystalline CdTe.

(ITO–p-CdTe) interface contains predominantly the surface states of the donor type, whereas case (2) corresponds to prevailing states of the acceptor type [12]. This conclusion is also consistent with the above assumption concerning an increase in the degree of compensation with the growing radiation dose.

An analysis of Fig. 1 shows that V_{oc} rather weakly varies with the dose, while J_{sc}, FF, and η exhibit significant changes. This behavior suggests that the $J_{sc}(D)$ variation plays a determining role in the nonmonotonic dose dependences of FF and η. A comparison of the dose dependences of J_{sc} (Fig. 1a) and ρ (Fig. 2) shows that, while the former parameter increases only by ~15%, the latter value exhibits an almost tenfold growth. Therefore, the growth of $\rho(D)$ plays a determining role in the drop of V_{oc}. Indeed, an increase in $\rho(D)$ leads to a growth in the dark saturation current that dominates over the increase in $J_{sc}(D)$.

In conclusion, we have studied the effect of γ radiation on the properties of polycrystalline CdTe solar cells. It was established that the main solar cell parameters exhibit a nonmonotonic variation with monotonically increasing dose. This behavior is attributed to a nonmonotonic dose dependence of the minority carrier lifetime in the base region. The short circuit current, the fill factor, and the conversion efficiency of the γ-irradiated CdTe solar cells can be greater than the analogous parameters of unirradiated devices.

REFERENCES

1. P. Baruch, J. Phys. Chem. Solids **8**, 153 (1959).

2. M. Yamaguchi, S. J. Taylor, M. Yu. Yang, *et al.*, Jpn. J. Appl. Phys. **35**, 3918 (1996).

3. T. Yamaguchi, S. J. Taylor, S. Watanabe, *et al.*, Appl. Phys. Lett. **72**, 1226 (1998).

4. M. Imaizumi, S. J. Taylor, M. Yamaguchi, *et al.*, J. Appl. Phys. **85**, 1916 (1999).

5. Sh. A. Mirsagatov and A. I. Sultanov, Élektron. Tekh. Ser. Lazern. Tekh. Optoélektron., No. 3 (55), 98 (1990).

6. M. J. Keevers and M. A. Green, J. Appl. Phys. **75**, 4022 (1994).

7. S. Zh. Karazhanov, J. Appl. Phys. **89**, 4030 (2001).

8. S. Zh. Karazhanov, Appl. Phys. Lett. **78**, 3836 (2001).

9. S. Zh. Karazhanov, Appl. Phys. Lett. **76**, 2689 (2000).

10. S. A. Azimov, Sh. A. Mirsagatov, and S. A. Muzaffarova, Geliotekhnika, No. 4, 22 (1982).

11. Sh. A. Mirsagatov and S. A. Muzaffarova, Geliotekhnika, No. 2, 18 (1983).

12. S. M. Sze, *Physics of Semiconductor Devices* (Wiley, New York, 1969; Énergiya, Moscow, 1973).

Translated by P. Pozdeev

Solving the Boundary Value Problems of Electrodynamics in the Regions of Fractal Geometry by the Method of *R*-Functions

V. F. Kravchenko* and M. A. Basarab

Institute of Radio Engineering and Electronics, Russian Academy of Sciences, Moscow, 103907 Russia
* e-mail: kravchenko_vf@fromru.com
Received May 22, 2003

Abstract—A numerical-analytical method of *R*-functions is used for the first time to solve the boundary value problems of electrodynamics in the fractal regions of the Sierpiński carpet and the Koch island types. © *2003 MAIK "Nauka/Interperiodica".*

As is known, the boundary of a medium may significantly affect the structure of the electromagnetic field and the character of propagation of the electromagnetic waves because their interaction with the interface gives rise to the phenomena of complete or partial reflection, diffraction, etc. A possible approach to modeling of the real interfaces consists in using the ideas of fractal geometry [1, 2]. In this paper, we consider for the first time the application of the *R*-function method (RFM) [3] to solving the boundary value problems of electrostatics and electrodynamics in the regions of fractal geometry.

Let us define a compound region $\Omega \subset R^2$ with the boundary $\partial\Omega$ in the form of a combination of primitive regions $\{\Omega_k\}_{k=1}^m$ obtained using the set-theoretical operations of intersection, combination, and complementation. We assume that the boundaries of these regions are determined by implicit equations $\{\omega_k(x, y) = 0\}_{k=1}^m$, where $\omega_k > 0$ for $(x, y) \in \Omega_k$ and $\omega_k < 0$ for $(x, y) \notin \overline{\Omega}_k = \Omega_k \cup \partial\Omega_k$. The RFM makes it possible to construct an equation of the boundary, $\partial\Omega\omega(x, y) = 0$, where the function ω is positive inside the region Ω, negative outside it, and turns into zero on the boundary $\partial\Omega$. The most commonly used set of *R*-functions is the set $\mathcal{R}_0$ with algebro-logical operations in the form

$$\begin{aligned} f_1 \wedge f_2 &\equiv f_1 + f_2 - \sqrt{f_1^2 + f_2^2}, \\ f_1 \vee f_2 &\equiv -(\overline{f}_1 \wedge \overline{f}_2), \quad \overline{f} \equiv -f. \end{aligned} \tag{1}$$

Let us consider a boundary value problem in the region $\Omega \subset R^2$ for electrostatics (the Poisson equation for an unknown potential u)

$$\Delta u = f \in \Omega, \tag{2}$$

or electrodynamics (the Helmholtz equation for the Hertz potential)

$$\Delta u + \lambda u = 0 \in \Omega, \tag{3}$$

with the Dirichlet boundary conditions

$$u|_{\partial\Omega} = 0. \tag{4}$$

We shall seek for a solution of the problem (2)–(4) in the form of the Kantorovich structure [3]

$$u = \omega \sum_{i=0}^{N} c_i \psi_i, \tag{5}$$

where ψ_i are the known basis set functions and c_i are undetermined coefficients. Let us consider a solution of the problem (2)–(4) in the form of (5) for the regions of fractal geometry of the Sierpiński carpet and the Koch island types [1].

The Sierpiński carpet is constructed as follows. The initial square is divided into nine equal squares and the central one is rejected. Applying this procedure to each of the residual squares and infinitely repeating the process, we arrive at a fractal object, known as the Sierpiński carpet, with the fractional dimension $D = \log 8 / \log 3 \approx 1.893$. Breaking the infinite process at the kth step, we obtain the kth-order prefractal. According to [4], the boundary function of the Sierpiński prefractal assumes the form

$$\omega_k(x, y) = \begin{cases} \omega_0(x, y), & k = 0, \\ \omega_{k-1}(x, y) \wedge F_k(x, y), & k = 1, 2, \ldots, \end{cases} \tag{6}$$

$$F_k(x, y) = -3^{-k}\omega_0[6\arcsin[\sin(3^{k-1}\pi x/2)]/\pi,$$
$$6\arcsin[(3^{k-1}\pi y/2)]/\pi], \tag{7}$$

$$\omega_0(x, y) = [(a^2 - x^2) \wedge (a^2 - y^2)]/2a.$$

(a) (b)

(a) (b)
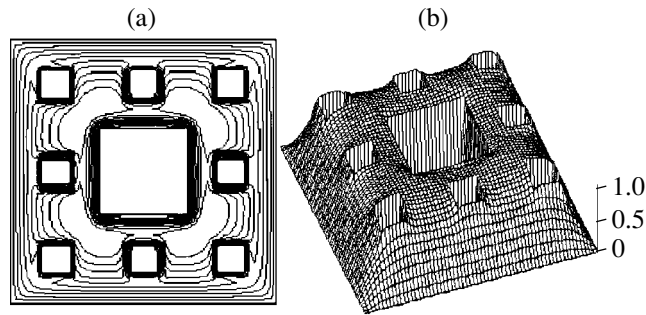
Fig. 1. Level lines for (a) the function of the second-order prefractal region of the Sierpiński carpet and (b) the potential distribution in the problem (2), (8).

Fig. 2. Level lines for (a) the function of the third-order prefractal region of the Koch island and (b) the fundamental mode E_{01}.

Figure 1a shows the level lines of the boundary function ω_2 for the second-level prefractal of the Sierpiński carpet.

By the same token, the Koch curve is constructed from an initial segment by removing its middle part, which is then replaced by the sides of the equilateral triangle. Repeating this procedure with respect to each of the obtained segments gives in the infinite limit the Koch curve with the fractal dimension $D = \log 4 / \log 3 \approx 1.26$. The boundary equation for the initial half-plane $y \leq 0$ is $\omega_0 = -y = 0$.

The RFM algorithm for the kth-order prefractal ($k \geq 1$) includes two steps:

(i) R-disjunction of the function ω_{k-1} with reflection with respect to the line $y = -x\sqrt{3} + 3^{k-1}\sqrt{3}$:

$$\tilde{\omega}_k(x, y) = \omega_{k-1}(x, y) \vee \omega_{k-1}[(-x - y\sqrt{3} + 3^k)/2,$$
$$(-x\sqrt{3} + y + 3^{k-1}\sqrt{3})/2];$$

(ii) R-conjunction of the function $\tilde{\omega}_k$ with reflection with respect to the line $x = 3^k/2$:

$$\omega_k(x, y) = \tilde{\omega}_k(x, y) \wedge \tilde{\omega}_k(3^k - x, y).$$

The Koch curve constructed on the sides of the equilateral triangle gives a structure known as the Koch island (or snowflake) [1]. The equation of a boundary of

the Koch island is obtained by applying three R-conjunction operations to the functions of the Koch curves rotated by $60°$ with respect to each other:

$$W_k(x, y) = \omega_k(y + 3^k/2, x - 3^{k-1}\sqrt{3}/2)$$
$$\wedge [\omega_k[y - x\sqrt{3} + 3^k)/2, (-x - y\sqrt{3} - 3^{k-1}\sqrt{3})/2]$$
$$\wedge \omega_k[(-y - x\sqrt{3} + 3^k)/2, (-x + y\sqrt{3} - 3^{k-1}\sqrt{3})/2]].$$

Figure 2a shows the level lines for the third-order prefractal for the Koch island constructed using the R-operations of the system $\mathscr{R}_0$ (1).

We can see that, in contrast to the fractal regions, the prefractal regions have piecewise smooth boundaries. Therefore, the basis set functions $\omega\psi_i$ of the Kantorovich structure (5) combine into a complete coordinate system [3], which provides the convergence of the variation and projection methods of solving the boundary value problems in the regions under consideration. The asymptotic behavior of the solution for the infinite increase of the prefractal order is considered in detail elsewhere [1].

Example 1. Let us solve the Dirichlet problem for the Laplace equation (2) ($f = 0$) in the region determined by the Sierpiński kth-order prefractal. In Eq. (2), u is an unknown potential. We assume that the potential f_0 is given at the external boundary $\partial\Omega_0$ of the region Ω and the potential f' is applied to the internal parts of the boundary $\partial\Omega' = \partial\Omega\backslash\partial\Omega_0$:

$$u = \begin{cases} f_0, & (x, y) \in \partial\Omega_0, \\ f', & (x, y) \in \partial\Omega\backslash\partial\Omega_0. \end{cases} \quad (8)$$

Let us seek for an approximate solution of the problem in the form of the Kantorovich structure

$$u = \omega_k \sum_{i=0}^{N} c_i \psi_i + \frac{f'\omega_0 + f_0\omega'}{\omega_0 + \omega'}, \quad \omega' = \Lambda_{j=1}^{k} F_j.$$

Choosing the Legendre polynomials of the order $2M$ as the basis set functions, ψ_i, we can leave (owing to sym-

Table 1. Relative errors of the differences between successive approximations $u^{(M)}$ and $u^{(M-1)}$

Polynomial order $2M$	Number of functions $N+1$	Uniform norm of difference $u^{(M)} - u^{(M-1)}$	L_2 norm of difference $u^{(M)} - u^{(M-1)}$
2	3	0.497	0.367
4	6	0.105	0.087
6	10	0.093	0.125
8	15	0.076	0.104

Table 2. Eigenvalues for the Koch island and the majorizing round regions

ν	2.405	3.832	5.135	5.520	7.016	8.417	8.654	10.174
$R\sqrt{\lambda}$	3.760	5.984	5.987	9.390	9.719	10.573	11.198	13.301
$\nu R/r$	4.166	6.637	8.894	9.561	12.152	14.579	14.989	17.622

metry considerations) only terms of the even powers with respect to both variables:

$$L_{k(i,j)}(x, y) = L_{2i}(ax)L_{2j}(ay), \quad i + j = \overline{0, M}.$$

Here, the ordering function is $k(i, j) = (i + j)(i + j + 1)/2 + j$. We find the undetermined coefficients c_i in the solution structure using the Bubnov–Galerkin method. To illustrate the convergence of the method, Table 1 shows the relative errors of the differences between successive approximations $u^{(M)}$, $u^{(M-1)}$ in the uniform and L_2 norms. Figure 1b displays the potential distribution for the second-order prefractal of the Sierpiński carpet type for $f_0 = 0$, $f' = 1$, $M = 4$ ($N = 14$).

Example 2. Let us solve the problem of calculating the TM waves in a regular waveguide with a prefractal cross section of the Koch island type. We find the solutions (eigenfunctions) of type (3) with the boundary conditions (4) with respect to the longitudinal component of the electric field, $u = E_z$, where $\sqrt{\lambda}$ is the transverse wavenumber. The solution structure assumes the form (5) with $\omega = W_k$. We use the Mth order Legendre polynomials as the basis set functions. Figure 2b shows the structure of the fundamental oscillation mode (E_{01} wave) for the third-order prefractal of the Koch island type. The second line in Table 2 gives the first eight normalized eigenvalues obtained for the following set of parameters: the prefractal order, $K = 3$; the vertical size, $h = 10$ mm; the horizontal size, $l = 2h/\sqrt{3} \approx 12$ mm;

$M = 3$ ($N = 9$). For a rough estimate and comparison, the first and the last lines in Table 2 give the eigenvalues of the majorizing round regions with the radii $R = h/\sqrt{3}$ and $r = h/3$ (here, ν are the zeroes of the Bessel functions). It is interesting to note that the eigenvalues corresponding to certain pairs of the eigenfunctions are virtually degenerate. We have observed this effect for various fractal parameters K.

The results of the numerical experiment lead us to the conclusion that the RFM method is effective for the regions with fractal boundaries. The proposed approach can be extended to a broad class of other fractal objects and to the external problems of the electromagnetic wave scattering from fractal structures.

REFERENCES

1. K. Falconer, *Techniques in Fractal Geometry* (Wiley, New York, 1997).

2. V. F. Kravchenko, *Lectures on the Theory and Applications of Atomic Functions* (Radiotekhnika, Moscow, 2003).

3. V. L. Rvachev, *Theory and Applications of R-Functions* (Naukova Dumka, Kiev, 1982).

4. M. A. Basarab and V. F. Kravchenko, Élektromagn. Volny Élektron. Sist. **6** (6), 31 (2001).

Translated by M. Kobrinskiǐ

Virtual Anode as a Source of Low-Frequency Oscillations of a High-Current Electron Beam

P. I. Markov*, I. N. Onishchenko, and G. V. Sotnikov

Kharkov Institute of Physics and Technology, National Scientific Center, Kharkov, Ukraine
* e-mail: pmarkov@kipt.kharkov.ua
Received April 3, 2003

Abstract—We have studied the transport of a relativistic electron beam with supercritical current in a cylindrical drift chamber in the presence of an ion flux. A theoretical analysis of the electron–ion flux dynamics was based on the coarse particle PIC method (code SOM). Simultaneous injection of a supercritical electron beam and a weak-current low-energy ion beam may result in the formation of a virtual anode in addition to the electron virtual cathode in a drift chamber. The virtual anode exhibits periodic pulsations. Numerical results obtained for hydrogen and nitrogen ions show that the ratio of the frequencies of these pulsations is inversely proportional to the square root of the ion mass ratio. These oscillations of the virtual anode lead to temporal modulation, at the same frequency, of both electron and ion currents at the drift chamber output. © 2003 MAIK "Nauka/Interperiodica".

According to the collective acceleration method [1], ions are accelerated in a slow space charge wave. This wave can be obtained by spatiotemporal modulation of a high-current electron beam. A low-frequency modulation necessary for the ion acceleration can be produced by passing the high-current electron beam (with a current above the vacuum threshold) through a plasma.

A possible physical mechanism of such modulation, which was proposed by Balakirev *et al.* [2], is as follows. Consider a thin annular electron beam injected into a cylindrical vacuum drift chamber. The limiting (critical) electron beam current that can be transported through this system is [3]

$$I_{ce} = mc^3(\gamma_e^{2/3} - 1)^{3/2}/[2e\ln(R/r_e)], \qquad (1)$$

where e and m are the electron charge and mass, respectively; γ_e is the relativistic factor of electrons in the beam; R is the drift chamber radius; and r_e is the electron beam radius. Increasing the beam current above the limit I_{ce} leads to the formation of a virtual cathode (VC). Ions present in such a system will be accelerated in the VC field and driven to the region of minimum potential. These ions will neutralize the volume charge of an electron cloud in the VC region, which leads to dissipation of the cloud. Breakage of the virtual cathode stops the supply of ions to the VC region. As a result, conditions for the VC formation are restored and the process is repeated.

Let us consider a different mechanism of producing low-frequency modulation, employing ions injected to the drift chamber in the same direction as the electron beam. The injected ion beam current is limited (by

analogy with the case of an electron beam) by a certain critical value given by an expression analogous to formula (1) for electrons [4]:

$$I_{ci} = Mc^3(\gamma_i^{2/3} - 1)^{3/2}/[2e\ln(R/r_i)], \qquad (2)$$

where M is the ion mass, γ_i is the relativistic factor, and r_i is the ion beam radius. A comparison of expressions (1) and (2) shows that, even for the electron and ion beams of comparable energy, the limiting ion current is significantly lower as compared to the electron analog, $I_{ci}/I_{ce} \sim \sqrt{m/M}$. At an ion beam current above I_{ci}, a positively charged cloud (called virtual anode, VA) is formed at the entrance to the drift chamber that reflects the ion beam. The frequency of VA oscillations is significantly lower than that of the VC oscillations. For the ratio of ion and electron beam currents on the order of the ratio of the corresponding critical values, we have $\omega_i/\omega_e \sim \sqrt{m/M}$ (ω_i and ω_e are the VA and VE oscillation frequencies, respectively). The VA oscillations will induce ion current oscillations at the drift chamber entrance. This time variation in the charge compensation of the electron beam will result in a related low-frequency modulation of the electron beam. Below we present the results of complete numerical simulation of a VC dynamics in the presence of low-energy ions in a cylindrical resonator.

The electron-ion flux dynamics was described using the following physical model. Thin annular electron and ions beams penetrate through a thin metal foil transparent for both species and enter a cylindrical drift chamber of radius R and length L. The chamber is exposed to an external magnetic field that is sufficiently
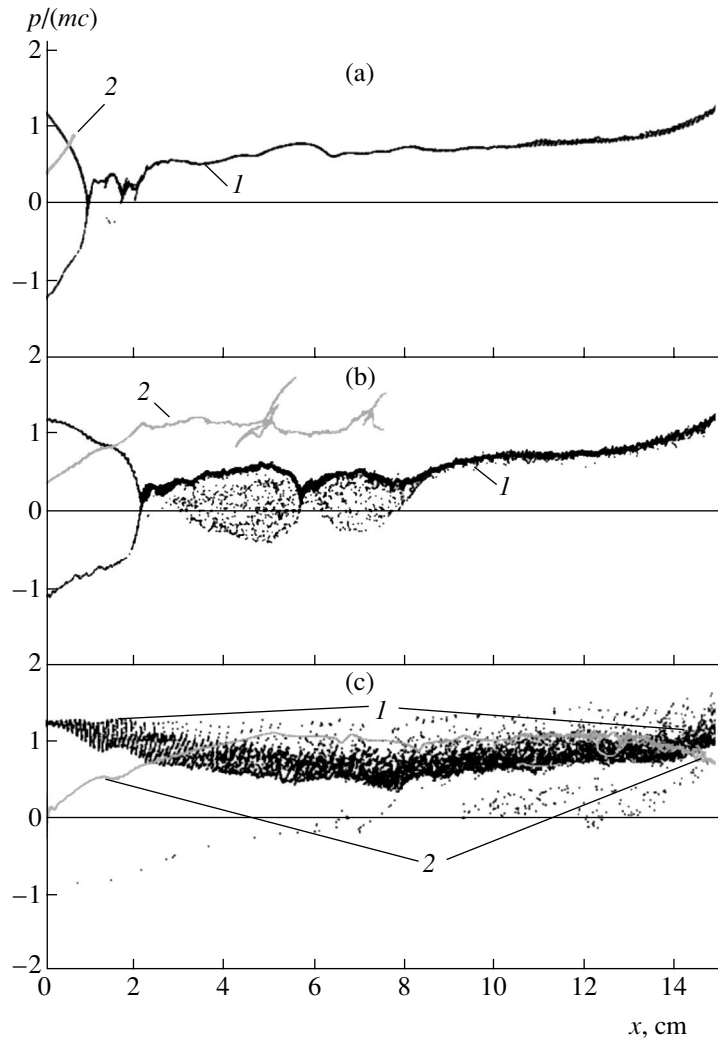
Fig. 1. Phase planes of momentum p versus longitudinal coordinate x for (*1*) electrons and (*2*) ions in the drift chamber at various moments of time $t = 1.54$ (a), 10.5 (b), and 23.97 ns (c). Ordinates of the points for ions are increased by a factor of $\sqrt{M/m}$.

strong to allow the motion of particles in the beams to be considered one-dimensional. We assume the electron and ion beam radii to coincide, $r_e = r_i = r_b$, although this is not a principal condition for the numerical simulation algorithm. Generalization to the case of noncoinciding beams is provided by introducing an additional boundary condition.

The numerical simulation algorithm [5] is based on the method of coarse particles [6] generalized to the case of arbitrary sign of the particle charge. In a refined version of the numerical code SOM, the accuracy of the model is controlled taking into account the energy conservation law. The numerical analysis was performed for the parameters of the experimental setup "Agat" [2]: $R = 2.5$ cm; $r_b = 1.625$ cm; electron beam current $I_b = 4.6$ kA; electron beam energy $eU_b = 280$ keV; $L = 15$ cm. For these drift chamber dimensions and electron beam parameters, the critical electron current is $I_{ce} = 3.8$ kA. The plasma was simulated by injecting low-

energy ($eU_i = 28$ keV) ions of hydrogen or nitrogen. The ion beam current ($I_i = 92$ and 25 A for hydrogen and nitrogen, respectively) was selected so that the unperturbed ion and electron current densities would be approximately equal. As noted above, the radius of the ion flux coincided with the electron beam radius. Under these conditions, the critical ion currents (2) for hydrogen and nitrogen ions are $I_{ci} \simeq 3.2$ and $\simeq 0.87$ A, respectively.

The charge transport dynamics for the simultaneously injected electron beam and ion flux was as follows. Within a time on the order of 1 ns, a VC forms at a distance of 1.0 cm from the left-hand end of the drift chamber (Fig. 1a). At this time, the number of ions in the system is small and the system (vircator) parameters are almost completely determined by the behavior of electrons. The VC is slightly (by 0.2 cm) shifted rightward from a position corresponding to the absence of ions in the drift chamber.
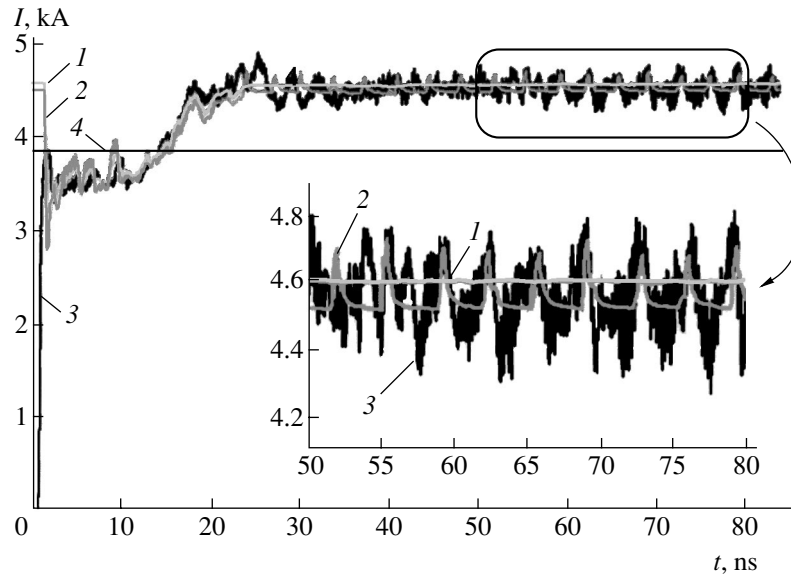
Fig. 2. Time series illustrating the dynamics of (*1*) electron current, (*2*) ion current, and (*3*) total current at the resonator output; straight line (*4*) shows the limiting electron current in the vacuum drift chamber.

Driven by the longitudinal electric field of the VC, hydrogen ions are accelerated to an energy determined by the VC potential that is approximately equal to the primary electron beam energy. Reaching the bottom of a potential well created by the VC, ions move without acceleration, with an almost constant energy. Subsequently (Fig. 1b), the accumulation of ions in the system drives the electron VC to move inward the drift chamber. As a result, the electric field strength in the VC region drops and this formation exhibits partial degradation, which leads to an increase in the output current. In addition, conditions for the VA formation are developed at the chamber entrance. This is evidenced by the appearance of slow ions at the entrance and by a positive surface charge density.

The aforementioned factors result in that the VA is formed in the system at *t* = 18 ns. At the same time, the electron VC is virtually completely broken. Subsequent interaction of the electron and ion fluxes takes place in the absence of VC. Strongly retarded electrons leave the resonator with time and the newly injected ones are decelerated to a much lower degree, while being strongly thermalized. The typical pattern for a system in this state is depicted in Fig. 1c. The VA exhibits pulsations in time, periodically vanishing and appearing again, this leading to related pulsations in the curve of input current and to modulation of the output electron current of the vircator (Fig. 2). For hydrogen ions, the frequency of these pulsations amounts to 300 MHz.

In the same way, we have performed analogous simulation for nitrogen ions injected to the same drift chamber. The pattern of charge transport dynamics is qualitatively the same as that for a hydrogen ion. The frequency of pulsations at the drift chamber entrance and exit decreases to 100 MHz, approximately in pro-

portion to the square root of the nitrogen to hydrogen ion mass ratio. In contrast to the case of hydrogen ions, the injection of nitrogen ions admits the regime with a periodic appearance of the electron VC on the background of the VA pulsations. This process is significantly slower than that described above, since it is related to the ion flight time through the drift chamber. The frequency of these electron VC pulsations is approximately one-fifth of the ion VA pulsation frequency.

The further system dynamics is determined by the interaction between electron and ion beams. The total and electron current at the resonator output exhibit oscillations about equilibrium values, exceeding the limiting electron current. The frequency of these oscillations is significantly lower, while the amplitude is significantly higher than those in the case of a single (electron) beam injection.

Thus, we have proposed and studied a mechanism of low-frequency modulation that can be used for creation of a slow wave in collective ion accelerators. The above analysis was performed assuming the one-dimensional motion of electrons and ions. Neglect of the transverse motions in the ion beam propagating in the drift chamber is acceptable for $H^2 \ll (Mc^2/e)(E_r/R)$, which would require applying an external magnetic field of ~100 kOe in the case of hydrogen ions. However, this strong requirement can be significantly reduced if we take into account that the joint injection of electron and ion beams is accompanied by a significant decrease in the strength of radial electric fields. In our numerical experiments, the ion current was selected so as to obey the condition of compensation for the electron beam charge. This is necessary for the VC compensation, but this condition also significantly reduces requirements

to the magnetic field strength necessary to maintain the equilibrium laminar ion beam motion.

REFERENCES

1. A. G. Lymar', N. A. Khizhnyak, and V. V. Belikov, Vopr. At. Nauki Tekh., Ser.: Fiz. Vysok. Énerg. At. Yadra, No. 3 (5), 78 (1973).

2. V. A. Balakirev, A. M. Gorban', I. I. Magda, *et al.*, Fiz. Plazmy **23**, 350 (1997) [Plasma Phys. Rep. **23**, 323 (1997)].

3. A. S. Bogdankevich and A. A. Rukhadze, Usp. Fiz. Nauk **103**, 609 (1971) [Sov. Phys. Usp. **14**, 163 (1971)].

4. R. B. Miller, *Introduction to the Physics of Intense Charged Particle Beams* (Plenum Press, New York, 1982; Mir, Moscow, 1984).

5. Yu. A. Berezin and V. A. Vshivkov, *Method of Particles in the Dynamics of Rarefied Plasma* (Nauka, Novosibirsk, 1980).

6. P. I. Markov, I. N. Onishchenko, and G. V. Sotnikov, in *Proceedings of the 12th International Conference "Microwave Engineering and Telecommunication Technologies," Sevastopol, 2002* (Veber, Sevastopol, 2002; ISBN), pp. 477–478.

Translated by P. Pozdeev

A Difference in the Change of Parameters of Silicon-on-Sapphire Structures upon X-ray Irradiation from the Sides of Epitaxial Layer and Substrate

A. N. Kiselev, V. A. Perevoshchikov*, V. D. Skupov, and D. O. Filatov

Nizhni Novgorod State University, Nizhni Novgorod, Russia

* e-mail: vap@nifti.unn.ru

Received May 28, 2003

Abstract—The data of atomic force microscopy and ellipsometry reveal a difference in changes of the silicon surface micromorphology, the refractive indices, and the extinction coefficients of silicon and sapphire in the silicon-on-sapphire structures upon pulsed X-ray irradiation at $E \leq 300$ keV from the side of the silicon epilayer and from the sapphire substrate. © *2003 MAIK "Nauka/Interperiodica".*

Previously [1], we reported that exposure of a silicon-on-sapphire (SOS) structure to pulsed X-ray radiation of "subthreshold" energies from the side of a heteroepitaxial silicon layer of this structure leads to a change in the silicon surface microrelief. Here we present new results obtained in the course of further investigations of this phenomenon in SOS structures with 0.3-μm-thick n-Si(001) films grown by monosilane pyrolysis on 470-μm-thick α-Al$_2$O$_3$(01$\bar{1}$2) substrates. The control samples were (001)-oriented single crystal silicon wafers (KEF-4.5 grade), also with a thickness of 470 μm.

The samples were irradiated in air from the side of the "device" silicon epilayer (side 1) or from the substrate (side 2) by unfiltered pulsed X-ray beam generated by a Ta anode. The average energy at the maximum of the continuous X-ray spectrum (bounded at $E \leq 300$ keV) was 75 keV. The samples were irradiated in a pulsed mode, at a pulse duration of 5 ns and a repetition period of 300 s. The absorbed radiation dose per pulse amounted to 30 r. The total dose was varied in a range of $D = 0$–900 r by increasing the number of absorbed radiation pulses.

Changes in the surface morphology of silicon epilayers and control single crystal samples were studied by atomic force microscopy (AFM). The AFM measurements were performed using a Smena-A instrument (NT-MDT Company, Russia) and the data were processed using an SPMLab 5.0 Analysis Only program package (©Thermomicroscopes). In addition, the refractive indices and extinction coefficients of silicon and sapphire were determined from side 1 using a

LEF-753 ellipsometer operating at a wavelength of $\lambda = 0.63$ μm.

The results of our experiments showed that irradiation of an SOS structure from the side of the silicon epilayer or from the substrate side changes the amplitude of the surface microrelief and modifies the shape of the distribution function of the lateral size of microroughnesses on the epilayer surface (Fig. 1). Analogous characteristics of the surface of control samples irradiated in the same regimes remained unchanged. The characteristic feature of the observed effects is a decrease in the height of microroughnesses on the surface of "device" epilayers irradiated from side 1 and an increase in this height upon the irradiation from side 2 (Figs. 1b and 1c).

It was found that the maximum height R_t of microroughnesses on the silicon film surface as a function of the radiation dose can be approximately (to within 12%) described by a linear relation $R_t = R_{t0} + aD$, where $R_{t0} = 51 \pm 4$ nm and $a = -1.2 \times 10^{-3}$ r^{-1} for the samples irradiated from side 1 and $a = 6.1 \times 10^{-2}$ r^{-1} for the samples irradiated from side 2. The halfwidth of the distribution function of the lateral microroughness size in the "device" silicon epilayer also almost linearly varies with the radiation dose. However, this parameter always increases with the dose, irrespective of the direction of X-ray irradiation. The slope of this dependence is 0.3 r^{-1} in the case of irradiation from side 1 and 0.12 r^{-1} in the case of irradiation from side 2.

According to the ellipsometric data, X-ray irradiation leads to an increase in the refractive index n in both the "device" epilayer and the substrate, irrespective of the exposed side (Fig. 2). Here, a difference in
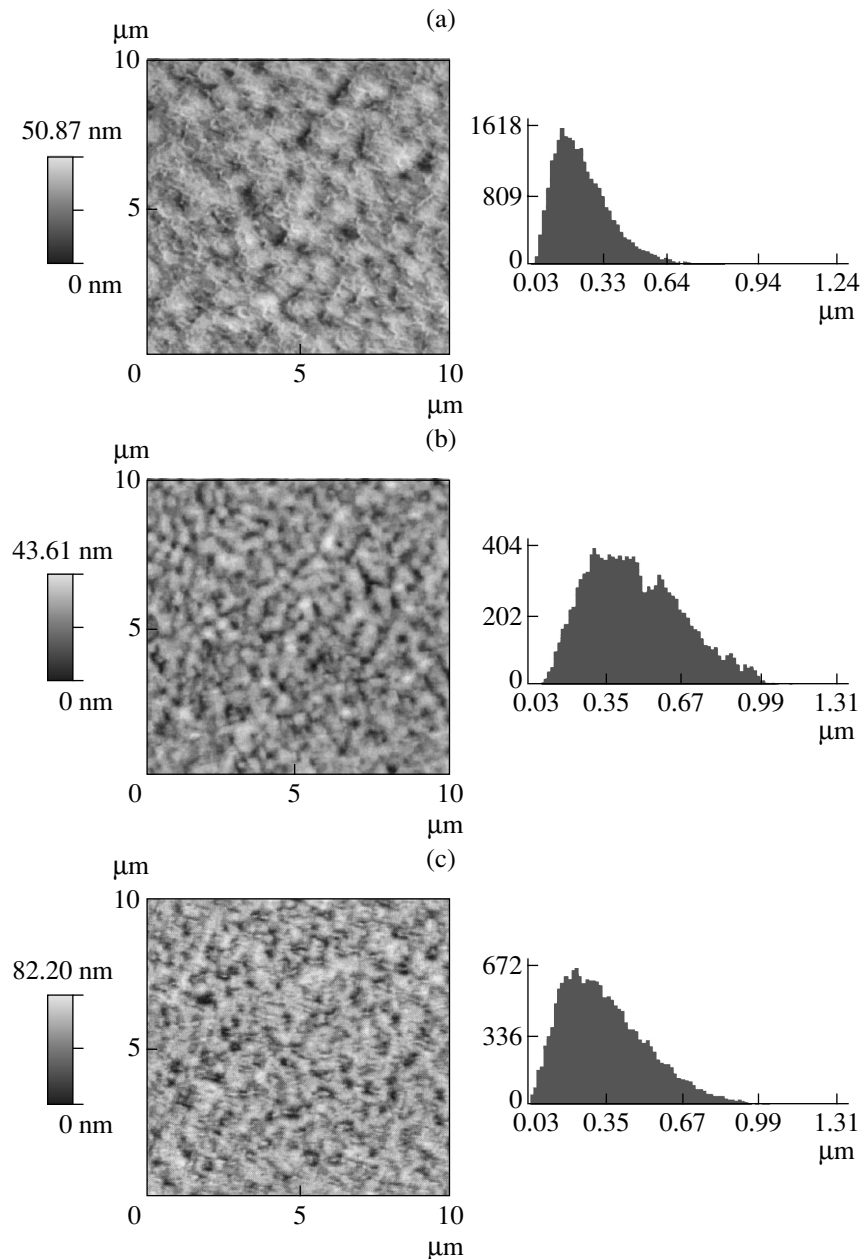
Fig. 1. AFM microtopographs and histograms of the lateral microroughness size distribution for SOS structures (a) in the initial state and (b, c) upon pulsed X-ray irradiation to a dose of $D = 900$ r from (b) side 1 (epilayer) and (c) side 2 (sapphire substrate).

the irradiation mode is manifested only by changes in the extinction coefficient k. In the substrate, k decreases with increasing radiation dose in both variants, while k of the silicon epilayer increases with the dose upon irradiation from side 1 and decreases upon the exposure of side 2. To within the experimental accuracy, the rates of variation of the extinction coefficient in both cases is $\left(\frac{dk}{dD}\right)_{Si} = 1.4 \times 10^{-5}$ r^{-1}. This behavior of the ellipsometric parameters of components of the irradiated SOS structures are most proba-

bly explained by redistribution of the metal impurities and electrically active defects between the epilayer and substrate under the action of elastic waves arising in sapphire in the field of ionizing radiation [1]. The growth of k is evidence of an increase in the high-frequency conductivity of the silicon film upon irradiation.

The nonequivalent response of the SOS structure components irradiated from sides 1 and 2 can be explained by asymmetry of the distribution of the absorbed X-ray radiation energy in depth of the compo-
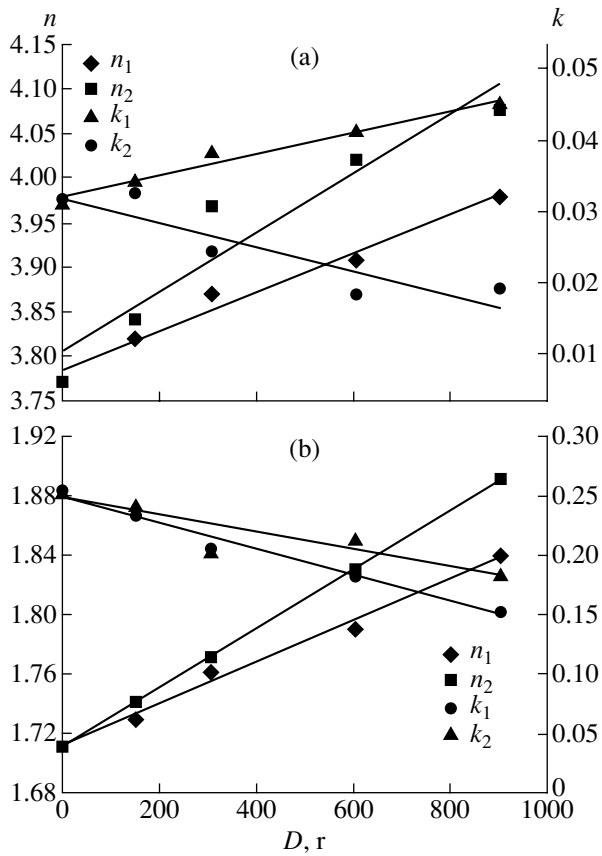
Fig. 2. Plots of the ellipsometric parameters n and k versus radiation dose D for (a) silicon epilayer and (b) sapphire substrate of SOS structures irradiated by X-ray pulses from sides 1 (n_1, k_1) and 2 (n_2, k_2).

sition. In the case of irradiation from side 1, a minimum in the absorbed energy (and, hence in the total amplitude of excited elastic waves) takes place in the epilayer and the adjacent substrate region. During the irradiation from side 2, this zone is subjected to the action of a wave field of greater amplitude (representing a superposition of elastic waves generated in the whole volume of the sapphire substrate). In this case, mechanical stresses of alternating sign not only activate the channel of nonconservative rearrangement of defects of the dislocation type in the epilayer [2], but additionally induce the microplastic deformation of silicon via slippage. Apparently, it is the latter process that accounts for the observed differences in the character of changes in the microrelief of "device" layers in SOS structures irradiated from the sides of silicon and sapphire.

REFERENCES

1. A. N. Kiselev, V. A. Perevoshchikov, V. D. Skupov, and D. O. Filatov, Pis'ma Zh. Tekh. Fiz. **27** (17), 35 (2001) [Tech. Phys. Lett. **27**, 725 (2001)].

2. P. V. Pavlov, Yu. A. Semin, V. D. Skupov, and D. I. Tetel'baum, Fiz. Tekh. Poluprovodn. (Leningrad) **20**, 503 (1986) [Sov. Phys. Semicond. **20**, 315 (1986)].

Translated by P. Pozdeev

Low-Energy Electron Mean Free Path
in Thin Films of Copper Phthalocyanine

S. A. Komolov*, É. F. Lazneva, and A. S. Komolov
Institute of Physics, St. Petersburg State University, St. Petersburg, Russia
* e-mail: sak.@paloma.spbu.ru

Abstract—The formation of thin organic films of copper phthalocyanine (CuPc) deposited onto the surface of gold-coated quartz crystal resonator was studied *in situ* under ultrahigh vacuum conditions by means of total electron-beam-induced current spectroscopy in combination with deposit thickness determination by piezocrystal microbalance technique. Variations in the fine structure of the total current spectra of CuPc layers of various thicknesses in the 0–8 nm interval have been analyzed and the electron mean free path in thin CuPc films was determined as a function of the electron energy. For electron energies of 5.0, 7.2, 14.4, and 18.0 eV above the Fermi level, the mean free path is 6.4, 3.9, 2.6, and 2.3 nm. © 2003 MAIK "Nauka/Interperiodica".

Introduction. Thin semiconducting organic films in contact with inorganic materials exhibit special electron properties that make such systems new promising materials for photovoltaic cells, light-emitting diodes, and some other devices of molecular electronics [1–3]. The electron energy structure at the interface between organic and inorganic materials, determining special features of the electron and photoelectron properties of such systems, can be successfully studied by methods of electron spectroscopy immediately in the course of deposition of the organic macromolecules onto inorganic substrates [4–6]. It was established that the formation of a potential barrier and the electron spectrum is accomplished upon deposition of several monolayers of macromolecules [5, 7, 8].

In this context, it was of interest to determine simultaneously the parameters such as the thickness of a deposited layer of organic molecules and the mean free path of low-energy (0–25 eV) electrons. The use of low-energy electrons excludes the possibility of electron-stimulated decomposition of organic molecules in the deposit. The thickness d of a film deposited onto a given substrate is usually estimated by measuring the thickness of an analogous film formed on the surface of a quartz crystal resonator situated in the same experimental chamber. However, in such cases one cannot be sure that the results are correct because the sticking coefficients of organic molecules on the resonator surface can significantly differ from those on the sample surface. This is also valid for the electron mean free path L, which is calculated based on the analysis of attenuation (or amplification) of the intensity of characteristic lines in the electron spectra of the substrate (or deposit), depending on the film thickness [9–11].

In this study, a quartz crystal resonator was used as the substrate for depositing organic molecules, as the

microbalance for simultaneously determining the deposit thickness, and as the electrode for measuring the total current spectra. This method excluded the errors in determining the film thickness and the electron mean free path, related to a difference in the sticking coefficients of molecules on the surfaces of a sample and a quartz crystal.

Experimental. The experiments were performed under ultrahigh vacuum (UHV) conditions in a chamber evacuated to a residual pressure of 5×10^{-8} Pa. The substrate was a standard quartz crystal resonator with a resonance frequency of 11.000045 MHz, a sensitivity of 9×10^{-10} g/Hz, and a surface area of 0.5 cm^2. CuPc molecules were deposited onto the resonator surface covered with a 40-nm-thick gold layer. The gold film ensured good conductivity and a high sticking coefficient. It was also important that gold does not react with adsorbed CuPc molecules and practically does not modify their electron structure [5].

Sequential deposition of gold and CuPc layers onto the quartz crystal resonator surface and parallel measurements of the deposit thickness and the total current spectra were performed *in situ*. The molecules of CuPc (Aldrich), evaporated from a Knudsen cell situated at a distance of 10 cm from the substrate, were deposited at an angle of 45° and a rate of 0.1 nm/min. CuPc molecules have a molecular weight of 576 amu and possess a chemical structure depicted in the inset in Fig. 1. In order to determine the thickness of a film, it is necessary to know the density of the deposit. According to the data of tunneling microscopy [12], the area of a CuPc molecule adsorbed on a solid surface is 1.9 nm^2. Assuming the height of the molecule to be 0.4 nm, we estimate the molecular volume at 0.76 nm^3 and the density of CuPc in a deposited layer at 1.3 ± 0.1 g/cm^3. An error of 3 Hz in the resonator frequency measurements

corresponds to the CuPc film thickness determined to within 0.05 nm.

The total current spectra were measured in the course of the CuPc film deposition. During these experiments, a beam of electrons with energies in the 0–25 eV interval and a total current of about 10 nA was incident perpendicularly to the sample surface and the energy derivative $S(E) = dI/dE$ of the total current $I(E)$ was measured in the sample circuit [13]. The position of the primary peak in the $S(E)$ signal (called the total current spectrum) corresponds to the vacuum energy level E_V for the sample surface. By measuring E_V variations in the course of deposition, it is possible to follow changes of the electron work function $W = E_V - E_F$, where E_F is the Fermi level of the system. A fine structure of the total current spectrum is determined by the energy dependence of the elastic scattering of electrons, related to the structure of the density of vacant electron states in the energy interval studied [13, 14].

For a deposited layer thickness $d < L$, where L is the mean free path of electrons in the film, the measured total current spectrum represents a superposition of an attenuated spectrum of the substrate and a spectrum characteristic of the deposited material. The intensity $S_1(d)$ of a signal due to the characteristic features of the substrate is attenuated according to the law [10, 11]

$$S_1(d) = S_{10}\exp(-2d/L), \tag{1}$$

where S_{10} is the initial intensity of the given characteristic signal. The intensity of features in the spectrum of the deposited film increases as

$$S_2(d) = S_{20}(1 - \exp(-2d/L)), \tag{2}$$

where S_{20} is the intensity of these features in the spectrum of a massive film ($d \gg L$). By simultaneously measuring the film thickness and the total current spectra and analyzing these spectra in terms of relations (1) and (2), it is possible to determine the electron mean free path L for the energies corresponding to the characteristic features in the total current spectra.

Results and discussion. Figure 1 shows a sequence of the total current spectra measured in the course of CuPc deposition. Here, curve *1* is the spectrum of a freshly deposited gold film characterized by an electron work function of 5.3 eV (arrow *1* at the energy axis indicates the position of the vacuum energy level for the initial gold film). Curves *2–7* represent the total current spectra measured for various CuPc film thicknesses (0.25, 0.5, 1.25, 2.0, 3.0, and 6.0 nm, respectively). As the deposit thickness grows, the spectra display a decrease in intensity of the characteristic features of gold (minimum **a** and maximum **b** in the region of 16–18 eV) and the development of a structure characteristic of CuPc (the main peaks being **A**, **B**, and **F** at 5.0, 7.2, and 14.4 eV, respectively). Here, peak **A** corresponds to the upper energy level in the π band, while **B** and **F** represent the lower levels of the σ_1 and σ_2 bands of vacant states in CuPc [15]. It should be noted that the electron
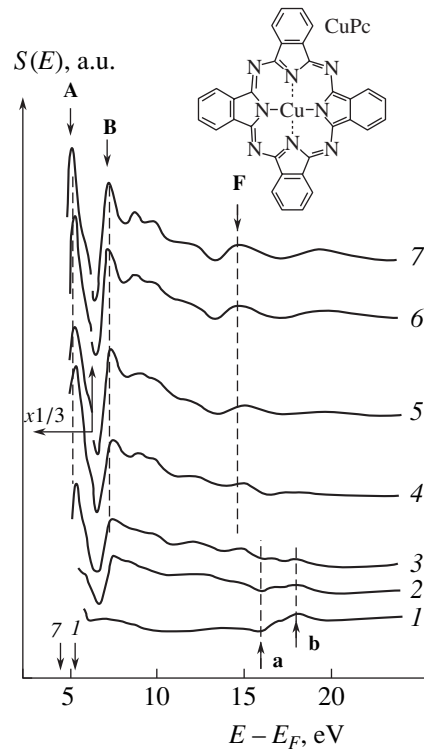
Fig. 1. Variation of the total current spectra in the course of CuPc deposition onto gold-coated quartz substrate: (*1*) freshly deposited gold film; (*2–7*) CuPc films with thicknesses 0.25, 0.5, 1.25, 2.0, 3.0, and 6.0 nm, respectively. Arrows *1* and *7* indicate the positions of vacuum energy levels for the corresponding curves.

work function decreases to 4.5 eV after deposition of a 1-nm-thick CuPc layer and then remains unchanged during the subsequent increase in the CuPc film thickness (arrow *7* at the energy axis indicates the position of the vacuum energy level for the CuPc film surface).

The fine structure of the total current spectrum of CuPc (peaks **A**, **B**, and **F**) is manifested at submonolayer coverages, when only separate CuPc molecules or their clusters are adsorbed on the gold surface. As the adsorption coverage grows, the intensity of these structural features increases. This behavior of the spectrum indicates that the electron structure of individual CuPc molecules remains virtually unchanged in the course of their aggregation into a massive film. An analysis of the variation of intensity of the main peaks in the total current spectra depending on the deposit thickness showed that low-energy peaks exhibit a slower growth rate.

The differences are most clearly pronounced when the experimental data are plotted on the semilogarithmic scale as $\ln(S_1/S_{10}) = f(d)$ for peak **b** and as $\ln((S_{20} - S_2)/S_{20}) = f(d)$ for peaks **A**, **B**, and **F**. These plots are presented in Fig. 2, where curves *1–3* correspond to the CuPc peaks **A**, **B**, and **F**, respectively, and curve *4*, to the substrate peak **b**. As can be seen, these semilogarithmic plots can be approximated with a good accuracy by straight lines. By determining the slopes of

S_1/S_{10}; $(S_{20} - S_2)/S_{20}$, a.u.
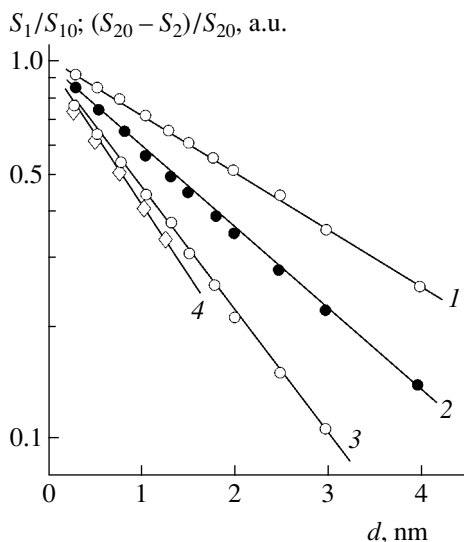
Fig. 2. Semilogarithmic plots describing variation of the intensity of peaks **A** (*1*), **B** (*2*), **F** (*3*), and **b** (*4*) in the total current spectra shown in Fig. 1.

these lines, we can calculate the electron mean free paths in thin CuPc films ($L = 6.4$, 3.9, 2.6, and 2.3 nm) for the corresponding electron energies (5.0, 7.2, 14.4, and 18.0 eV above the Fermi level). The observed decrease in the electron mean free path is consistent with the notions about an increase in the probability of electron scattering with increasing kinetic energy (in the energy range studied), assuming the electron–electron scattering with the excitation of interband transitions [9, 16]. The absolute values of the electron mean free path agree in the order of magnitude with the data summarized in [9].

Conclusion. We have determined the mean free path of low-energy electrons in thin organic films of CuPc *in situ*, in the course of their deposition in vacuum onto the gold-coated surface of a quartz crystal resonator. The dynamics of variation of the total current spectra, followed depending on the deposited film thickness, reflects their structure of vacant electron states in the energy interval from 5 to 25 eV above the Fermi energy level. The electron mean free paths determined from an analysis of the total current spectra amount to $L = 6.4$, 3.9, 2.6, and 2.3 nm for the electron energies of $E - E_F = 5.0$, 7.2, 14.4, and 18.0 eV, respectively. In our experiments, the gold-coated surface of a quartz crystal resonator (used for measuring the deposit thickness) was simultaneously used as the sample for which the total current spectra were measured in the course of

CuPc deposition. This method eliminates uncertainties related to the possible difference of the sticking coefficients of molecules on the surfaces of a sample and a quartz resonator, influencing the results of the electron mean free path determination.

REFERENCES

1. J. F. Nierengarten, G. Hadziioannon, and N. Armaroli, Mater. Today **4** (2), 16 (2001).

2. J. Wang, G. Yu, A. J. Heeger, and G. Sradanov, Org. Electron. **1**, 33 (2000).

3. N. Fahlman and W. R. Salaneck, Surf. Sci. **500**, 904 (2002).

4. K. Seki, N. Hayashi, H. Oji, *et al.*, Thin Solid Films **393**, 298 (2001).

5. I. G. Hill, J. Schwartz, and A. Kahn, Org. Electron. **1**, 5 (2000).

6. A. S. Komolov and P. J. Moller, Synth. Met. **128**, 205 (2002).

7. A. S. Komolov and Yu. G. Aliaev, Phys. Low-Dimens. Semicond. Struct. **5–6**, 37 (2001).

8. S. A. Komolov, N. B. Gerasimova, A. G. Sidorenko, and Yu. G. Alyaev, Pis'ma Zh. Tekh. Fiz. **26** (24), 80 (2000) [Tech. Phys. Lett. **26**, 1110 (2000)].

9. M. P. Seah and W. A. Dench, Surf. Interface Anal. **1** (1), 2 (1979).

10. S. A. Komolov and L. T. Chadderton, Surf. Interface Anal. **1** (3), 82 (1979).

11. S. A. Komolov, Zh. Tekh. Fiz. **49**, 2361 (1979) [Sov. Phys. Tech. Phys. **24**, 1318 (1979)].

12. C. Ludvig, R. Strohmaier, and J. Petersen, J. Vac. Sci. Technol. B **12**, 1963 (1994).

13. S. A. Komolov, *Total Current Spectroscopy of Surfaces* (Gordon and Breach, Philadelphia, 1992).

14. S. A. Komolov, P. J. Moller, E. F. Lazneva, and A. S. Komolov, Appl. Surf. Sci. **175**, 663 (2001).

15. A. S. Komolov and P. J. Moller, Synth. Met. **128**, 205 (2002).

16. W. F. Krolikovski and W. E. Spicer, Phys. Rev. B **1**, 478 (1970).

Translated by P. Pozdeev

Effect of the Ion Beam Current Density on the Formation of Implanted Metal Nanoparticles in a Dielectric Matrix

A. L. Stepanov[a, b] and V. N. Popok[c, *]

[a] Institute of Physics 1, Aachen Technical University, 52056 Aachen, Germany
[b] Kazan Physicotechnical Institute, Russian Academy of Sciences, Kazan, Tatarstan, 420029 Russia
[c] Göteborg University & Chalmers University of Technology, 41296 Göteborg, Sweden
* e-mail: popok@fy.chalmers.se
Received June 2, 2003

Abstract—The effect of the ion beam current density, varied within 4–15 μA/cm^2, on the formation of metal nanoparticles in a subsurface layer of SiO$_2$ substrates implanted with 30-keV Ag$^+$ ions to a dose of 5×10^{16} cm^{-2} was studied by optical spectroscopy and atomic force microscopy techniques. An increase in the ion beam current density leads to the formation of nanoparticles of a greater size as a result of the glass substrate heating and due to an increase in the diffusion mobility of implanted silver atoms. These results suggest the possibility of controlling the dimensions of implanted nanoparticles in dielectrics by means of variation of the ion beam current density during the process. © 2003 MAIK "Nauka/Interperiodica".

Ion implantation is a technologically convenient and effective method for introducing impurities into solids, in particular, for the obtaining of composite materials based on dielectrics containing dispersed metal nanoparticles [1]. Such composites are promising materials for ultrafast-response nonlinear optical devices dealing, for example, with pico- and femtosecond laser pulses [2, 3]. The synthesis of nanoparticles in dielectrics by ion implantation is a complicated process depending on a large number of factors, including ion energy, dose, type, and the dielectric matrix [4]. Recently, we have demonstrated that substrate temperature is an important factor influencing the size and distribution of nanoparticles [5–8].

This study was aimed at determining the influence of another implantation parameter—the ion beam current density—on the formation of nanoparticles.

The substrates for the obtaining of composites were made of a silicate glass (SiO$_2$, Heraeus). The glass substrates were implanted with 30-keV Ag$^+$ ions to a dose of 5×10^{16} cm^{-2}, at an ion beam current density variable from 4 to 15 μA/cm^2. The process was conducted in a vacuum of 10^{-5} Torr using an ILU-3 implanter system. At the beginning of ion bombardment, the substrates occurred at room temperature.

The optical properties of the metal-implanted composite material (Ag:SiO$_2$) were studied by absorption spectroscopy. The measurements were performed on a Perkin-Elmer Lambda 19 spectrophotometer. The surface morphology of ion-implanted glasses was studied on a Dimension 3000 scanning probe microscope (National Instruments) operating in the atomic force microscopy (AFM) regime in the tapping mode.

Figure 1 shows the optical transmission spectra of synthesized Ag:SiO$_2$ composite layers. As can be seen from these spectra, the samples exhibit selective absorption in the visible spectral range, which is indicative of the formation of silver nanoparticles in the glass matrix and is explained by the plasma polariton resonance of these nanoparticles [9]. The spectra are typical of the silver nanoparticles in a SiO$_2$ matrix, while a shift of the resonance absorption band toward long-wavelength spectral region with increasing ion beam current density can be related to an increase in the nanoparticle size and in the efficiency of aggregation of the implanted silver atoms [9].
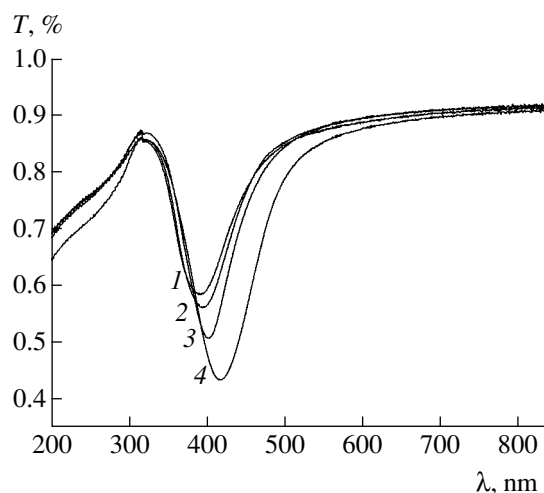
Fig. 1. The optical absorption spectra of SiO$_2$ implanted with 30-keV Ag$^+$ ions at various ion beam current densities (μA/cm^2): (*1*) 4; (*2*) 8; (*3*) 12; (*4*) 15.
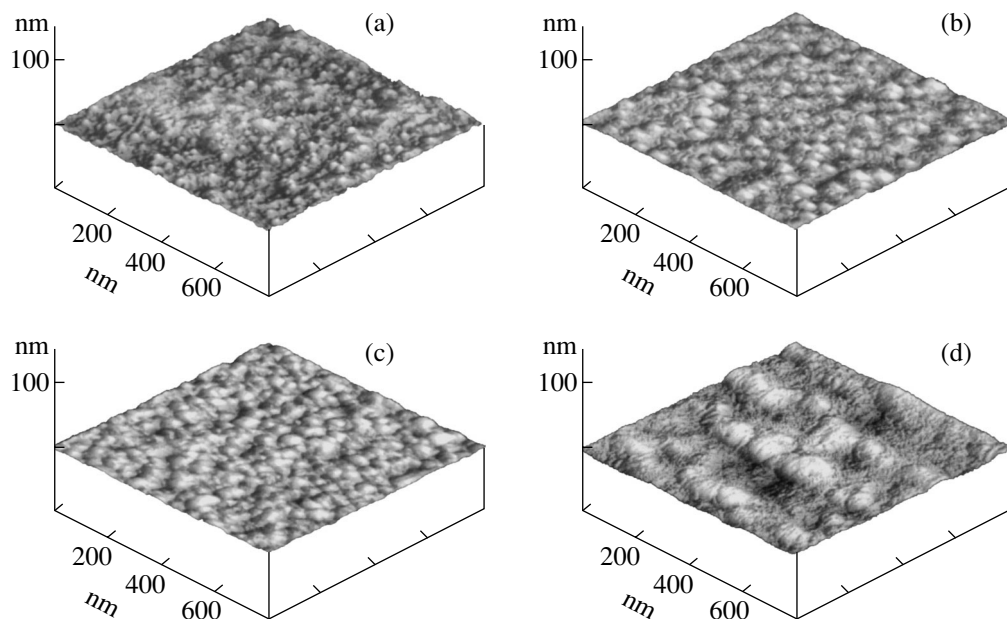
Fig. 2. AFM images of the surface of SiO_2 substrates implanted with 30-keV Ag^+ ions at various ion beam current densities ($\mu A/cm^2$): (a) 4; (b) 8; (c) 12; (d) 15.

Previously [10], the depth–concentration profiles of implanted silver were computer-simulated using a DYNA algorithm. The results showed that prolonged ion irradiation (to a dose of $\geq 10^{16}$ cm^{-2}) leads to a shift of the maximum in the implanted silver concentration profile toward the SiO_2 surface (to a depth of ~10 nm), with a monotonic decrease of the metal concentration in depth of the sample. The effective accumulation of silver atoms to a level exceeding the solubility limit for this metal favors intensive nucleation and growth of nanoparticles immediately at the glass surface. It should be also noted that an important factor in the case of high-dose implantation is the effect of surface sputtering. Estimates show that, in the ion bombardment regime employed, the thickness of a sputtered glass layer amounts to several tens of nanometers [1]. Under these conditions, we may expect that metal nanoparticles can be exposed on the dielectric surface. Indeed, it was demonstrated that, during the high-dose implantation of low-energy (<60 keV) Fe^+ ions into SiO_2 [11], Ag^+ ions into Ta_2O_5, SiO_2, Si_3N_4 [12, 13], and soda-lime silicate glass [14], and Cu^{2+} ions into Al_2O_3 [15], the formation of metal nanoparticles is accompanied by the appearance of hemispherical protrusions on the dielectric surface.

Figure 2 presents the AFM images of the SiO_2 surface after implantation with Ag^+ ions at various ion beam currents. In contrast to a smooth surface of the initial glass, the morphology of ion-implanted samples is characterized by the presence of hemispherical protrusions reflecting the "emergence" of spherical nanoparticles to the surface as a result of glass sputtering.

This phenomenon provides for a methodological possibility of qualitatively estimating the dimensions of largest nanoparticles synthesized in the subsurface layer. As can be seen from Fig. 2, there is a clear tendency of the size of hemispheres to increase in the glasses implanted at a higher ion beam current density. A comparison of the results presented in Figs. 1 and 2 shows that an increase in the ion beam current density is accompanied by a correlated variation of the optical absorption spectrum (growth of the absorption intensity and shift of the peak toward long-wavelength region) and the AFM images (increase in the size of protrusions indicative of coarsening of the nanoparticles).

The most probable factor responsible for the growth of silver nanoparticles in the samples studied is the increase in the glass substrate temperature during ion implantation. Previously [6], we experimentally demonstrated that the implantation of 60-keV Ag^+ ions to a dose of 4×10^{16} cm^{-2} at a relatively low ion beam current density (3 $\mu A/cm^2$) into silicate glasses maintained at 20 or 60°C leads to the formation of greater particles in the substrates heated to the higher temperature. The results of theoretical modeling [8] indicate that, as the temperature of an ion-irradiated glass matrix increases from 20 to 100°C, the coefficient of silver diffusion in the glass grows by at least three orders in magnitude.

The whole process of nanoparticle synthesis by ion implantation can be divided into several stages, including incorporation of accelerated ions, diffusion, nucleation, and growth. In our experiments, all samples prior to the implantation occurred under equal conditions at room temperature. Different values of the ion beam

current density imply a difference in the number of ions supplied to the target and in the energy flux that is converted into heat. Thus, both the rate of substrate heating (i.e., the temperature gradient) and the temperature of glass are obviously higher under the conditions of greater ion current density. According to our estimates, an increase in the ion beam current density from 4 to 15 $\mu A/cm^2$ may increase the temperature of the sample surface layer up to 80–100°C. Comparing these estimates to the results obtained in [6, 8], we may ascertain that temperature-enhanced (thermostimulated) diffusion of metal in the glass takes place under the conditions of implantation at elevated ion beam current densities.

According to this, the higher temperature of the glass matrix and the greater temperature gradient in this matrix increase the diffusion mobility of silver atoms, thus leading to their effective sink to the nuclei and, hence, to coarsening of the nanoparticles (diffusion growth). As a result, a smaller proportion of implanted silver atoms in the "hot" matrix (in comparison to that in the "cold" samples) remain unattached to nanoparticles and stay dispersed in the implanted layer. In addition, heating creates conditions for the coarsening of nanoparticles due to the Ostwald maturation mechanism, whereby smaller nuclei (possessing lower melting temperatures) dissociate into atoms and this material is spent for the growth of other nanoparticles, this also resulting in a decrease in their total number. Apparently, under the implantation conditions studied in our experiments, the substrate temperature not yet reaches a level at which there arises an effective diffusion flow of incorporated atoms from the implanted subsurface layer to deeper layers.

In conclusion, we have established that using higher ion beam current densities during Ag^+ ion implantation into glass leads to the formation of metal nanoparticles of greater dimensions and even to their aggregation, probably as a result of the substrate heating and an increase in the diffusion mobility of incorporated silver atoms. This effect suggests the possibility of obtaining composite materials with the metal nanoparticle size in the subsurface layer controlled by variation of the ion beam current density during implantation.

REFERENCES

1. A. L. Stepanov and D. E. Hole, Recent Res. Development Appl. Phys. **5**, 1 (2002).

2. D. Ricard, in *Nonlinear Optical Materials: Principles and Applications* (IOS, Amsterdam, 1995).

3. A. L. Stepanov, I. B. Khaĭbullin, P. Taunsend, D. Khole, and A. A. Bukharaev, RF Patent No. 2156490 (2000).

4. P. D. Townsend, P. J. Chandler, and L. Zhang, *Optical Effects of Ion Implantation* (Cambridge Univ. Press, Cambridge, 1994).

5. A. L. Stepanov, V. N. Popok, and D. E. Khole, Fiz. Khim. Stekla **28**, 131 (2002).

6. A. L. Stepanov, D. E. Khole, and V. N. Popok, Pis'ma Zh. Tekh. Fiz. **27** (13), 57 (2001) [Tech. Phys. Lett. **27**, 554 (2001)].

7. A. L. Stepanov, Pis'ma Zh. Tekh. Fiz. **27** (20), 39 (2001) [Tech. Phys. Lett. **27**, 862 (2001)].

8. A. L. Stepanov, D. E. Hole, and P. D. Townsend, J. Non-Cryst. Solids **260**, 65 (1999).

9. U. Kreibig and M. Vollmer, *Optical Properties of Metal Clusters* (Springer, Berlin, 1995).

10. A. L. Stepanov, V. A. Zhikharev, and I. B. Khaĭbullin, Fiz. Tverd. Tela (St. Petersburg) **43**, 733 (2001) [Phys. Solid State **43**, 766 (2001)].

11. A. A. Bukharaev, V. M. Janduganov, E. A. Samarsky, and N. V. Berdunov, Appl. Surf. Sci. **103**, 49 (1996).

12. M. T. Pham, W. Matz, and H. Seifarth, Anal. Chim. Acta **350**, 209 (1997).

13. G. Steiner, M. T. Pham, Ch. Kuhne, and R. Salzer, Fresenius J. Anal. Chem. **362**, 9 (1998).

14. A. L. Stepanov, V. N. Popok, D. E. Khole, and A. A. Bukharaev, Fiz. Tverd. Tela (St. Petersburg) **43**, 2100 (2001) [Phys. Solid State **43**, 2192 (2001)].

15. A. L. Stepanov, V. N. Popok, D. E. Hole, and I. B. Khaĭbullin, Appl. Phys. A **74**, 441 (2002).

Translated by P. Pozdeev

Laser Diodes (λ = 0.98 μm) with a Narrow Radiation Pattern and Low Internal Optical Losses

S. O. Slipchenko, N. A. Pikhtin, N. V. Fetisova, M. A. Khomylev, A. A. Marmalyuk, D. B. Nikitin, A. A. Padalitsa, P. V. Bulaev, I. D. Zalevskiĭ, and I. S. Tarasov

Ioffe Physicotechnical Institute, Russian Academy of Sciences, St. Petersburg, Russia
SigmaPlus Company, Moscow, Russia
e-mail: nike@hpld.ioffe.rssi.ru
Received June 19, 2003

Abstract—Quantum-confined InGaAs/AlGaAs/GaAs heterostructures for laser diodes emitting at λ = 0.98 μm, optimized to provide for reduced radiation divergence in the vertical plane and decreased internal optical losses, have been synthesized by metalorganic-hydride vapor-phase epitaxy. For the obtained laser diodes the far field pattern full width at half-maximum in the vertical plane falls within 16°–19°, the internal optical losses are about 0.7 cm^{-1}, the internal quantum yield amounts to 97%, and the maximum continuous emission power reaches 8.6 W. © *2003 MAIK "Nauka/Interperiodica"*.

Implementation of the concept of high-power semiconductor lasers, stipulating minimization of the internal optical losses in laser heterostructures [1, 2], allowed high output powers to be reached [1–3] that considerably expanded the field of possible applications of such lasers. However, traditionally low directivity of the laser emission [1, 2] hinders effective use of the whole radiant energy. In this context, optimization of the laser heterostructure design aimed at decreasing the radiation divergence in the plane perpendicular to the *p–n* junction, while retaining low internal optical losses, is currently an important task.

From the theory of planar dielectric waveguides, it is known that the radiation pattern in the far field zone is determined by the electromagnetic field profile in the waveguide [4]. Several papers have been devoted to the influence of the semiconductor heterostructure design and parameters on the radiation pattern [1, 5–10]. In particular, the effect of the optical mode tunneling into the narrow-bandgap regions confined between wide-bandgap emitters was studied in [5–8]. This allowed the far field pattern width in the plane perpendicular to the *p–n* junction to be reduced to 15° [7]. Unfortunately, high values of the optical confinement factors for strongly doped wide-bandgap emitters hinder the obtaining of minimum internal optical losses inherent in high-power semiconductor lasers [1, 2]. The use of narrow-bandgap inserts is effective only provided that a considerable proportion of the optical mode is propagating in wide-bandgap emitters. In a structure with increased waveguide width, this approach no longer provides an effective solution of the problem. However, the very fact of increased waveguide layer width allows the radiation pattern to be narrowed and the internal optical losses to be decreased [1].

It was theoretically demonstrated and experimentally confirmed [1] that the only natural limitation in further increasing the waveguide thickness is related to the threshold conditions for the high-order waveguide mode generation. One possible means of avoiding the generation of high-order modes is to increase the related absorption losses [1]. Using this approach allowed a heterostructure to be created with a waveguide width of 1.2 μm, for which the maximum output radiation power in the continuous wave (CW) regime was 10.9 W, the far field pattern width in the plane perpendicular to the *p–n* junction was 36°, and the internal optical losses fell within 1 cm^{-1} [1]. Further increase in the waveguide layer thickness determining the appearance of high-order modes can be provided by decreasing the difference between refractive indices of the waveguide layers and emitters. However, this method leads to a strong decrease in the optical confinement factor for the active region and, hence, to a significant increase in the threshold current [1] that is critical for reaching the maximum laser efficiency. For decreasing this effect, it was suggested [11] to form an active region comprising a quantum well confined between layers possessing a smaller bandgap width as compared to that of the waveguide layer. However, this method also did not allow the threshold current to be reduced to an acceptable level.

In [9, 10], a decrease in the radiation beam divergence in the plane perpendicular to the *p–n* junction was reduced based on the effect of leaky modes. This approach allowed obtaining a radiation pattern width on the order of 10° at an output power of 3 W in a multimode CW generation regime using a mesastructure with a strip width of 50 μm.

This Letter demonstrates the possibility of simultaneously reducing the divergence of laser diode radiation in the plane perpendicular to the *p–n* junction and decreasing the internal optical losses, while retaining high output powers and low threshold currents.

In the theoretical part of this study, we have modeled the laser heterostructure design in order to select the optimum parameters (thicknesses and bandgap widths of emitters and waveguides) of epitaxial layers from the standpoint of suppressing higher modes. Since the heights of barriers formed by the breaks of conduction bands and the valence bands of the emitters and waveguides influence the intensity of carrier leakage from waveguide to emitter, these barriers cannot be lower than a certain critical value characterized by the activation energy of this process. In turn, the depth of a quantum well (QW) at a given bandgap width of the waveguide determines the temperature sensitivity of the threshold current.

Thus, selection of the solid solution composition for the emitter and waveguide layers has to be based primarily on the condition of minimization of the leakage currents and carrier ejection from QWs. Based on the results of our previous investigations of the radiation characteristics of laser diodes [12], we have selected the following solid solution compositions: $Al_{0.38}Ga_{0.62}As$ ($E_g = 1.9$ eV) for the emitter layers and $Al_{0.3}Ga_{0.7}As$ ($E_g = 1.8$ eV) for the waveguide layers. The results of calculations using the model of a planar dielectric waveguide [4] showed that the far field pattern full width at half-maximum for the fundamental mode in the plane perpendicular to the *p–n* junction amounts to 15° when the waveguide width is 4 µm. However, the wave equation for this waveguide layer thickness has three additional solutions corresponding to high-order nodes. This may lead to an increase in the radiation divergence if the threshold conditions are fulfilled [1]. For this reason, the heterostructure design with a waveguide width of 4 µm was further optimized so as to suppress the high-order mode generation.

We used the method of metalorganic-hydride vapor-phase epitaxy (MOVPE) to grow the separate confinement laser heterostructures of the optimum design determined in the course of modeling. The structure comprised heavily doped N-$Al_{0.38}Ga_{0.62}As$ ($N = 10^{18}$ cm^{-3}) and P-$Al_{0.38}Ga_{0.62}As$ ($P = 10^{18}$ cm^{-3}) emitters (with silicon and zinc as the donor and acceptor impurity, respectively), an intentionally undoped 4-µm-thick waveguide based on the $Al_{0.3}Ga_{0.7}As$ solid solution, and the active region formed by two strained 70-Å-thick InGaAs quantum wells. After MOVPE synthesis, the heterostructures were processed by the standard postgrowth methods [13, 14] with allowance for the results of model calculations so as to form mesastrip heterolasers with a strip width of $W = 100$ µm and Fabry–Perot resonators of various lengths within $L = 1000$–4000 µm. Finally, the diodes were mounted strip-
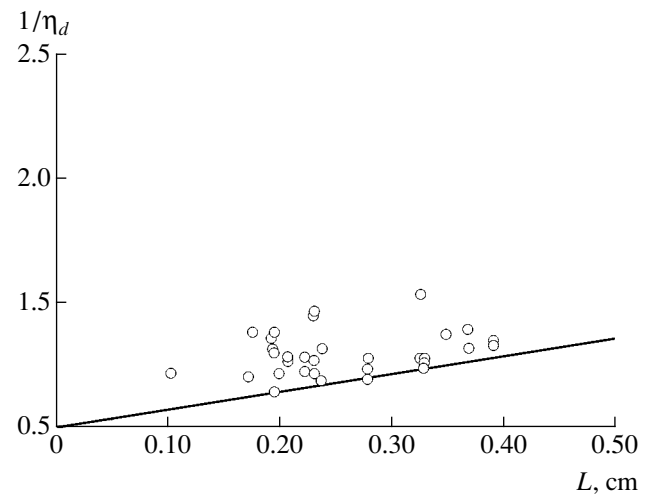

Fig. 1. The plot of experimental inverse external differential quantum efficiency $1/\eta_d$ versus cavity length L.

downward on copper heat sinks and fixed with the aid of an indium-based solder.

All devices were characterized by measuring their output power–current (*P–I*) characteristics in the CW regime at a heat sink temperature of 20°C. These data were used to determine the differential quantum efficiencies and threshold current densities. Figure 1 shows the experimental plot of inverse quantum efficiency ($1/\eta_d$) versus the cavity length L. Approximating this dependence by a straight line and using the well-known method [14], we determined the internal differential quantum efficiency ($\eta_i = 97\%$) and internal optical losses ($\alpha_i = 0.7$ cm^{-1}). The low level of internal optical losses achieved with the given heterostructure design allows laser diodes with superlong cavities to be obtained without significant loss in the external differential quantum efficiency. An increase in the cavity length allows the laser diodes to be pumped by high currents, thus significantly increasing the output power and retaining high efficiency of electrical to optical power conversion.

Investigation of the radiation characteristics of laser diodes with natural mirrors showed that maximum output power in the CW regime at a constant heat sink temperature of 20°C reached 4 W from one cavity edge face and was limited by the catastrophic optical mirror degradation (COMD). In order to avoid the COMD, the laser edge faces were covered, by means of magnetron sputtering, with Si/SiO$_2$ dielectric layers combining the functions of mirrors and passive coatings.

Figure 2 shows the typical plots of the output power P versus pumping current for laser diodes with the cavity length $L = 4000$ µm and cavity edge faces bearing antireflection (AR) and high-reflection (HR) coatings with a power reflection coefficient of 5 and 95%, respectively. The output radiation power in the CW regime at a constant temperature (20°C) of the laser

P_{out}, W
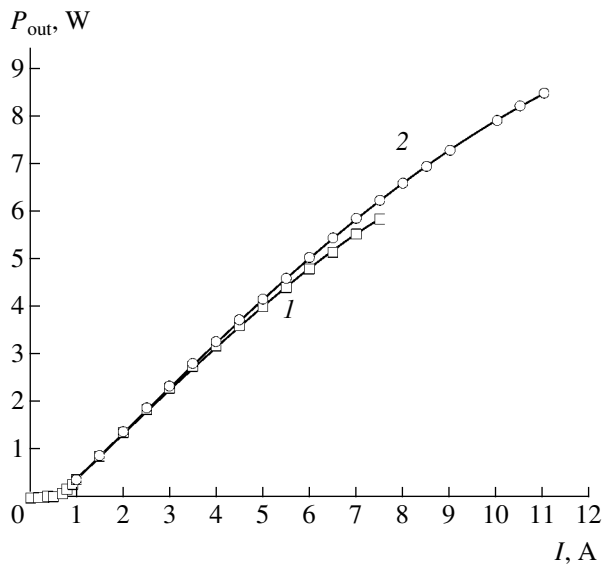
Fig. 2. The *P–I* curves measured in the CW regime for a laser diode with a cavity length of $L = 4000$ μm, a strip width of $W = 100$ μm, and AR(5%)/HR(95%) dielectric coatings on the cavity edge faces. The measurements were performed at a constant temperature of 20°C maintained for (*1*) the heat sink and (*2*) the laser crystal.

crystal and the heat sink was 8.6 and 5.8 W, respectively. A characteristic feature observed for all laser diodes studied was saturation of the *P–I* characteristic beginning at a relatively low pumping current density. This saturation could not be avoided even by maintaining the laser crystal at a constant temperature. This fact indicates that a decrease in the external differential efficiency with increasing pumping current was related
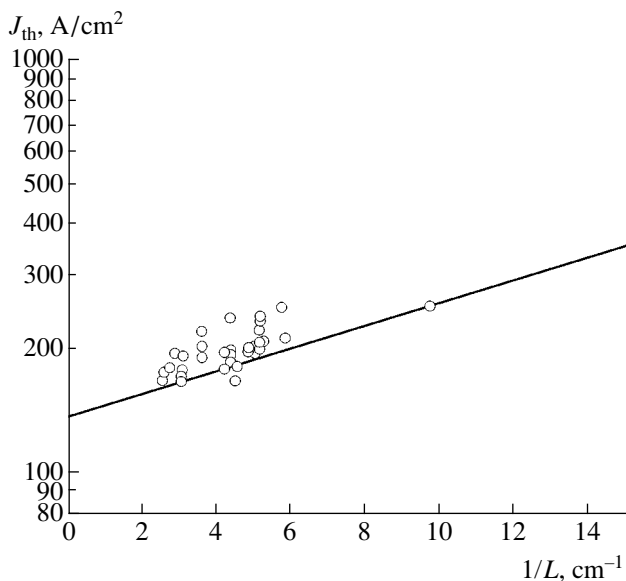
predominantly to the low efficiency of the charge carrier transport to the active region and, to a lower extent, to heating of the active region.

Figure 3 presents a plot of the threshold current density versus inverse length of the laser diode cavity. A threshold current density for the infinite resonator length amounted to 130 A/cm². This threshold current density does not exceed the analogous values for the lasers with usual (extended) waveguide [12]. This fact indicates that the proposed laser design allows a drop in the optical confinement factor of the active region to be successfully avoided.

Figure 4 shows the typical patterns of the radiation intensity distribution in the far field zone in the plane perpendicular to the *p–n* junction for various continuous pumping currents. The values of the far field pattern full width at half maximum ($\Theta_\perp$) amounted to 16–19° in the entire range of pumping currents studied. These data agree well with the results of theoretical calculations. As can be seen, neither the $\Theta_\perp$ value nor the shape of these patterns (described with a high accuracy by the Gauss curve) change significantly when the pumping current is varied. This stability of the radiation pattern is evidence of a single-mode character of emission of the laser diodes in the plane perpendicular to the *p–n* junction.

In conclusion, we have used MOVPE technology to manufacture quantum-confined InGaAs/AlGaAs/GaAs heterostructures with the parameters optimized so as to reduce the internal optical losses and decrease the radiation divergence in the plane perpendicular to the *p–n* junction. Based on these heterostructures, high-power multimode laser diodes of mesastrip design operating at λ = 0.98 μm have been obtained. The possibility of

J_{th}, A/cm²

Fig. 3. The plot of experimental threshold current density J_{th} versus inverse cavity length $1/L$ and its linear approximation (solid line) for laser diodes with a strip width of $W = 100$ μm.

I, a.u.
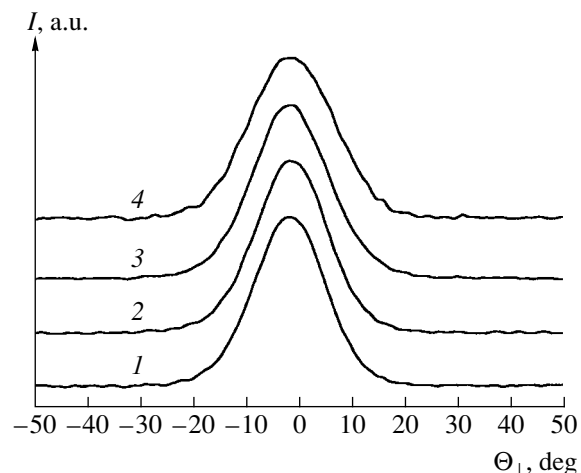
Fig. 4. Distribution of the laser radiation intensity in the far zone in the plane perpendicular to the *p–n* junction for a laser diode with $L = 4000$ μm operating in the CW regime at various pumping currents $I = 0.5$ (*1*), 1 (*2*), 3 (*3*), and 5 A (*4*). The corresponding full width at half maximum is $\Theta_\perp = 16.0°$ (*1*), 16.1° (*2*), 17.2° (*3*), and 19.2° (*4*).

maintaining a single-mode lasing regime in the plane perpendicular to the *p–n* junction is demonstrated, for which the far field pattern full width at half-maximum in the entire range of pumping currents is within 16–19°. The maximum output radiation power in the CW regime reaches 8.6 W at a laser crystal temperature of 20°C.

REFERENCES

1. A. Al-Muhanna, L. J. Mawst, D. Botez, *et al.*, Appl. Phys. Lett. **73**, 1182 (1998).
2. D. A. Livshits, A. Yu. Egorov, I. V. Kochnev, *et al.*, Fiz. Tekh. Poluprovodn. (St. Petersburg) **35**, 380 (2001) [Semiconductors **35**, 365 (2001)].
3. X. He, S. Srinivasan, S. Wilson, *et al.*, Electron. Lett. **34**, 46 (1998).
4. N. C. Casey, Jr. and M. B. Panish, *Heterostructure Lasers* (Academic, New York, 1978; Mir, Moscow, 1981).
5. J. Temmyo and M. Sugo, Electron. Lett. **31**, 642 (1995).
6. D. Vakhshoori, W. S. Hobson, H. Han, *et al.*, Electron. Lett. **32**, 1007 (1996).
7. J. M. Verdiell, M. Ziari, and D. F. Welch, Electron. Lett. **32**, 1817 (1996).
8. N. B. Zvonkov, S. A. Akhlestina, A. V. Ershov, *et al.*, Kvantovaya Élektron. (Moscow) **26**, 217 (1999).
9. V. I. Shveĭkin and V. A. Gelovani, Kvantovaya Élektron. (Moscow) **32**, 683 (2002).
10. J. P. Donnely, R. K. Huang, J. N. Walpole, *et al.*, IEEE J. Quantum Electron. **39**, 289 (2003).
11. M. Buda, T. G. van de Roer, L. M. F. Kaufmann, *et al.*, IEEE J. Sel. Top. Quantum Electron. **3**, 173 (1997).
12. P. V. Bulaev, V. A. Kapitonov, A. V. Lyutetskiĭ, *et al.*, Fiz. Tekh. Poluprovodn. (St. Petersburg) **36**, 1144 (2002) [Semiconductors **36**, 1065 (2002)].
13. E. G. Golikova, V. A. Gorbylev, Yu. V. Il'in, *et al.*, Pis'ma Zh. Tekh. Fiz. **26** (7), 57 (2000) [Tech. Phys. Lett. **26**, 295 (2000)].
14. A. Yu. Leshko, A. V. Lyutetskiĭ, N. A. Pikhtin, *et al.*, Fiz. Tekh. Poluprovodn. (St. Petersburg) **36**, 1393 (2002) [Semiconductors **36**, 1308 (2002)].

Translated by P. Pozdeev

Determination of the Magnetic Anisotropy Constant in Microparticles of Powder-Based Permanent Magnets by Mössbauer Spectroscopy

Sh. M. Aliev, I. K. Kamilov, Sh. O. Shakhshaev, and A. A. Abdullaev

Institute of Physics, Dagestan Scientific Center, Russian Academy of Sciences, Makhachkala, Dagestan, Russia
e-mail: kamilov@datacom.ru

Received May 15, 2003

Abstract—A new Mössbauer technique for determining the uniaxial magnetic anisotropy constant in microparticles of powder-based permanent magnets has been developed and experimentally verified. © *2003 MAIK "Nauka/Interperiodica".*

The technology of anisotropic powder-based permanent magnets includes alignment of the monodomain uniaxial particles of a magnetically hard material in a magnetic field, followed by pressing the material in this oriented state [1]. As a result, the material acquires an axial magnetic texture whose degree of perfection is characterized by the texture scattering angle θ_t or the relative remanent magnetization $\dfrac{M_r}{M_s}$ (M_r and M_s being the remanent and saturation magnetization, respectively).

Previously [2], we developed a method based on the Mössbauer spectroscopy for determining θ_t and $\dfrac{M_r}{M_s}$.
Using the results of that study, we propose a new technique for measuring the uniaxial magnetic anisotropy constant K of the microparticles of powder-based permanent magnets. The K value determines the coercive force and the specific energy of a permanent magnet [1].

The internal energy per unit volume of a permanent magnet in the external magnetic field H is [1]

$$E_U = \frac{1}{2}HM - \frac{1}{2}NM^2, \qquad (1)$$

where M and N are the magnetization and demagnetization factors of the given magnet, respectively. Rotation of the magnetization vectors of particles relative to their easy axes under the action of the field H is hindered by the magnetic anisotropy energy [1]

$$E_A = K\sin^2\varphi, \qquad (2)$$

where φ is a certain average angle of deviation of the magnetization vectors from easy axes in the field H. The balance of E_U and E_A values yields

$$K = \frac{HM - NM^2}{2\sin^2\varphi}. \qquad (3)$$

Based on the conclusions derived in [2] and the relation obtained in that study,

$$\cos^3\theta_t + \frac{9k - 12}{3k + 4}\cos\theta_t + \frac{8 - 12k}{3k + 4} = 0, \qquad (4)$$

we can determine the magnetic texture scattering angle θ_t using the parameter k determined as the ratio of areas under the second and first (or fifth and sixth) lines of the ^{57}Fe Mössbauer spectrum ($k = S_{2(5)}/S_{1(6)}$). The sample for Mössbauer measurements represents a thin plate cut from a magnet in the plane perpendicular to the axis of texture.[1]

Once the texture scattering angle θ_t is known, it is possible to determine the relative remanent magnetization as [2]

$$\frac{M_r}{M_s} = \frac{1 + \cos\theta_t}{2}. \qquad (5)$$

The sample of a textured magnetic material can be formally represented by a single crystal plate with the magnetization vector M_s making an angle $\varphi_0 = \arccos(M_r/M_s)$ with the normal to the sample surface (Fig. 1a). Using this approximation, it is possible to reduce the angles θ_i between the axis of texture and easy axes to an average angle φ_0, which simplifies solution of the problem. By the same token, the relative magnetization of a magnet in the field H applied along the texture axis (Fig. 1b) can be expressed as

$$\frac{M}{M_s} = \frac{1 + \cos\theta}{2} = \cos\varphi_1. \qquad (6)$$

Using relations (3), (5) and (6) and taking into account

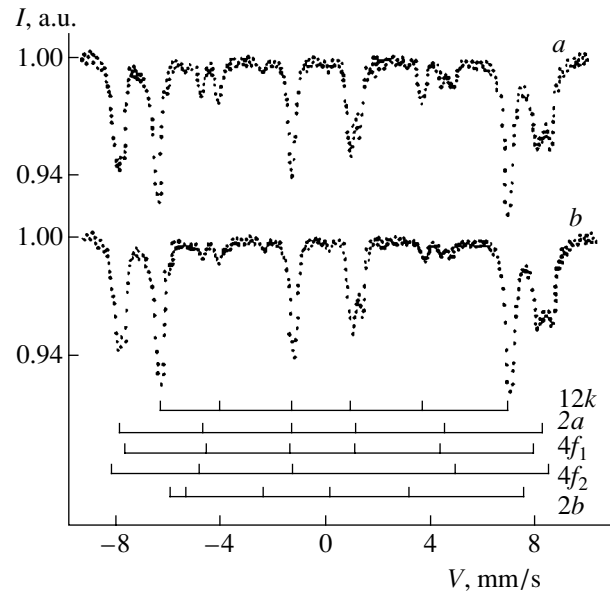[1] Demagnetization factor for a thin plate is $N = 1$ [1].
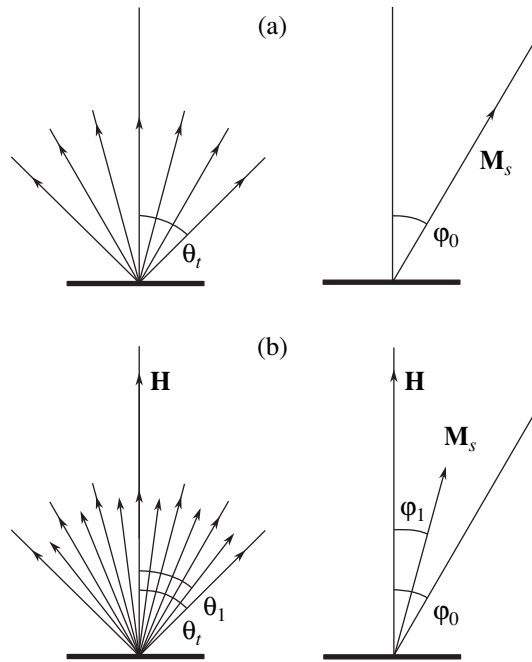
Fig. 1. Distribution of the particle magnetization vector directions relative to the texture axis in a powder-based permanent magnet (left diagrams) and in a single crystal magnet with the easy axis making an angle φ_0 with the normal to the sample plane: (a) in the remanent magnetization state (demagnetizing field assumed equal to zero); (b) in a magnetizing field H applied along the texture axis.

Fig. 2. ^{57}Fe Mössbauer spectra of a 16BA-190 permanent magnet measured (*a*) without applied magnetic field and (*b*) in a field of $H = 2.1$ kOe parallel to the texture axis. The direction of the beam of γ-quanta coincides with the axis of texture.

that $\varphi = \varphi_0 - \varphi_1$ (Fig. 1), we finally obtain

$$K = \frac{M_s \cos\varphi_1 (H - M_s \cos\varphi_1)}{2\sin^2(\varphi_0 - \varphi_1)}. \qquad (7)$$

The proposed method was verified on a 16BA-190 grade magnet based on barium ferrite $BaFe_{12}O_{19}$ [3]. The sample had the shape of a 70-μm-thick plate with a diameter of 15 mm, cut from the magnet along the plane perpendicular to the axis of texture. The measurements in a magnetic field were performed using a water-cooled solenoid. The source of γ-quanta was ^{57}Co in a chromium matrix, with a beam divergence angle not exceeding 5°.

Figure 2 shows the Mössbauer spectra of the sample measured with and without applied magnetic field. The spectra exhibit a superposition of five Zeeman sextets related to iron ions in five magnetic sublattices of barium ferrite [4]. From these spectra, we have obtained $\theta_t = 40°$, $M_r/M_s = 0.88$, and $\varphi_0 = 28°$. In a magnetic field with $H = 2.1$ kOe, the corresponding values are $\theta = 19°$, $M/M_s = 0.97$, and $\varphi_1 = 12°$. For the given magnetic material, $4\pi M_r = 3000$ G [3] and, taking into account the relative remanent magnetization, $M_s = 270$ G. Substituting these data into (7) yields $K = 3.3 \times 10^6$ erg/cm^3. This value coincides with the values of the anisotropy constant obtained by the torsional pendulum

and the ferromagnetic resonance techniques for single crystal ferrite $BaFe_{12}O_{19}$ [5].

An advantage of the method described above is the possibility to perform measurements on the commercial samples, which is very important for testing permanent magnets in order to control and optimize their technical characteristics. Note that the proposed technique has nothing preventing its use for determining the uniaxial anisotropy constants of magnetically hard materials of some other systems (Fe–Co–Ni–Al–Cu, Fe–Co–Cr, etc.) widely used in permanent magnet technology [1].

REFERENCES

1. V. V. Sergeev and T. I. Bulygina, *Magnetically Hard Materials* (Énergiya, Moscow, 1980).

2. Sh. M. Aliev and I. K. Kamilov, Pis'ma Zh. Tekh. Fiz. **20** (5), 9 (1994) [Tech. Phys. Lett. **20**, 178 (1994)].

3. A. A. Preobrazhenskiĭ and E. G. Bishard, *Magnetic Materials and Elements* (Vysshaya Shkola, Moscow, 1986).

4. P. P. Kirichok, O. F. Verezhak, M. B. Voronina, *et al.*, Izv. Vyssh. Uchebn. Zaved. Fiz., No. 1, 93 (1982).

5. J. Smit and H. P. J. Wijn, *Ferrites* (Wiley, New York, 1959; Inostrannaya Literatura, Moscow, 1962).

Translated by P. Pozdeev

Synthesis, Microstructure, and the Transport and Magnetic Properties of Bi-Containing High-Temperature Superconductors with a Porous Structure

M. I. Petrov, T. N. Tetyueva, L. I. Kveglis, A. A. Efremov, G. M. Zeer, K. A. Shaihutdinov, D. A. Balaev, S. I. Popkov, and S. G. Ovchinnikov

Kirensky Institute of Physics, Siberian Division, Russian Academy of Sciences, Krasnoyarsk, Russia
Krasnoyarsk Institute of Commerce and Economics, Krasnoyarsk, Russia
Krasnoyarsk State University of Technology, Krasnoyarsk, Russia
Reshetnev Siberian State Aerospace University, Krasnoyarsk, Russia
e-mail: smp@iph.krasn.ru
Received June 18, 2003

Abstract—Preliminary data on the synthesis and physical properties of polycrystalline $Bi_{1.8}Pb_{0.3}Sr_2Ca_2Cu_3O_x$ high-temperature superconductors of low density with a foam-like microstructure are reported. © *2003 MAIK "Nauka/Interperiodica".*

Recently, Reddy and Schmitz [1] reported on the synthesis of a superconducting foam made of $YBa_2Cu_3O_7$ high-temperature superconductor (HTSC). Such a foam may be an almost ideal material for active elements of fault current limiters, since critical currents in the foam immersed in liquid nitrogen can significantly exceed those in bulk HTSCs. This is explained by the fact that the foam contains open pores which are readily filled by a coolant (liquid nitrogen) that provides effective heat removal from the entire volume of a material. In addition, a superconducting foam can exhibit enhanced pinning due to a fractal structure [2], which also increases the critical current and the levitation force.

We have synthesized a low-density HTSC ceramics with a composition $Bi_{1.8}Pb_{0.3}Sr_2Ca_2Cu_3O_x$. The method of synthesis of this bismuth-containing ceramics was similar to that described in [3]. However, we modified the final stage of annealing, so that the growth of HTSC crystallites occurred predominantly in the *ab* plane. Because of a random orientation of grains in a polycrystal, such a growth leads to an increase in the material volume. In addition, calcium carbonate was completely decomposed during the final annealing stage. The excess pressure of carbon dioxide also favors an increase in the material volume. As a result, the density of the material was 0.38 of the theoretical value for $Bi_{1.8}Pb_{0.3}Sr_2Ca_2Cu_3O_x$. Figure 1 shows an image of the structure of a material under consideration, obtained by the method of scanning electron microscopy (SEM). The SEM measurements were performed on a REM-100U scanning electron microscope operating at an

accelerating voltage of 30 kV and a ×1000 magnification. The samples were coated by a layer of aluminum with a thickness of several nanometers, since otherwise the charge of the electron beam was accumulated on the specimen surface in the course of SEM measurements. The Al layer was formed by vacuum deposition. By comparing the images obtained from the Al-coated and uncoated samples, it was shown that the coating had no
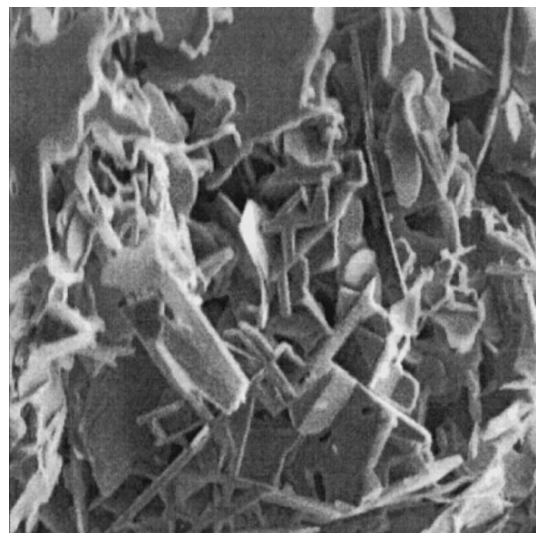
KSTU* REM-100U* 30 kV ×1000   20 μm

Fig. 1. SEM image of a $Bi_{1.8}Pb_{0.3}Sr_2Ca_2Cu_3O_x$ sample with a foam-like microstructure.

effect on the material structure. As can be seen from Fig. 1, the material possesses a porous structure. The size and morphology of pores do not significantly vary within the image field, the pore size changing from a few μm to several tens μm. The image exhibits scale-invariant elements which are arranged regularly and rather symmetrically. This conclusion is confirmed by an analysis of the Fourier transform performed for a large number of micrographs. The specific surface area of the samples measured using the thermal desorption of argon and calculated using the Brunauer–Emmet–Teller equation was 6.5 m^2/g.

Figure 2 shows the temperature dependence of electric resistivity $\rho(T)$ of a sample measured in a temperature range of 77–300 K. The superconducting transition temperature ("$R = 0$") is 107 K. Extrapolation of $\rho(T)$ from high temperatures to $T = 0$ gives a residual resistance of $\rho \approx 0$ that indicates that the effect of grain boundaries is negligible. Such a behavior of $\rho(T)$ is characteristic of single crystals [4]. This result is rather surprising, since the material represents a low-density polycrystal. The absolute value of the electric resistivity $\rho(T)$ has proved to be higher by one order of magnitude as compared to the values available in the literature for bismuth-containing HTSC single crystals [4]. However, we did not perform a correction of ρ with allowance for the actual cross section of our porous material. In our opinion, there is no sense in doing this unless the problem of fractal dimensionality of our samples is solved.

The temperature dependences of magnetization $M(T)$ of HTSC $Bi_{1.8}Pb_{0.3}Sr_2Ca_2Cu_3O_x$ samples with a foam microstructure, which were measured in zero-field-cooling (ZFC) and field-cooling (FC) regimes (at a magnetic field $H = 13$ Oe) are presented in Fig. 3 (circles) in comparison to the temperature dependences $M(T)$ of a powder-like bismuth-containing compound prepared from the original foam (solid lines). The comparison shows that the diamagnetic response and a difference between the ZFC and FC procedures are greater in the case of the sample with a foam-like structure. This confirms a significant enhancement of pinning in the porous quasi-low-dimensional material.

The levitation force (which depends directly on the critical current and pinning force) of a $Bi_{1.8}Pb_{0.3}Sr_2Ca_2Cu_3O_x$ HTSC sample with a foam-like structure was measured under the following conditions. A permanent Nd–Fe–B magnet (diameter $d = 9$ mm, height $h = 6$ mm, and mass $m = 2.97$ g) was mounted above the surface of a pellet made of $Bi_{1.8}Pb_{0.3}Sr_2Ca_2Cu_3O_x$ HTSC (diameter $D = 22$ mm and height $H = 6$ mm). As a reference sample, we used a $YBa_2Cu_3O_7$ pellet of high density (0.93 of the theoretical value) with the same dimensions, which was sintered by the standard ceramic technology. The measurements were performed at the liquid-nitrogen temperature. Repulsive force between the HTSC sample
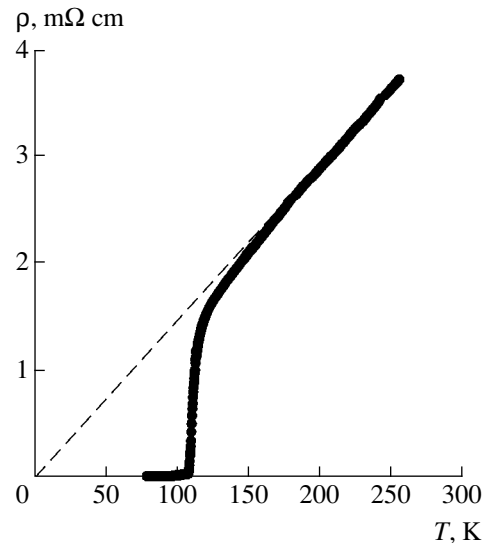

Fig. 2. The temperature dependence of electric resistivity $\rho(T)$ of a $Bi_{1.8}Pb_{0.3}Sr_2Ca_2Cu_3O_x$ HTSC sample with a foam-like microstructure.
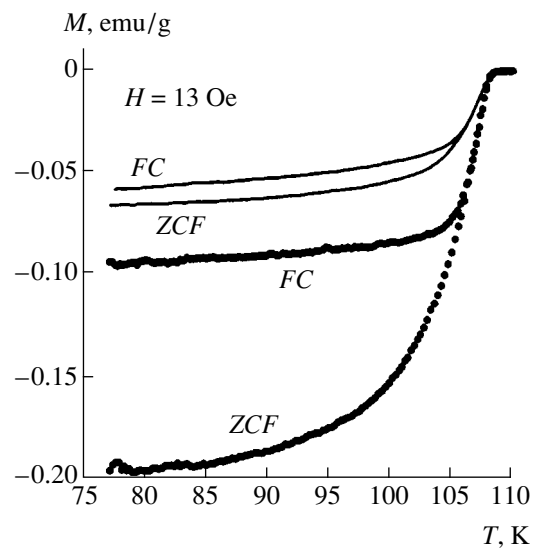
Fig. 3. The temperature dependences of magnetization $M(T)$ of a $Bi_{1.8}Pb_{0.3}Sr_2Ca_2Cu_3O_x$ HTSC sample with a foam-like microstructure and a powder-like $Bi_{1.8}Pb_{0.3}Sr_2Ca_2Cu_3O_x$ HTSC sample (filled circles and solid lines, respectively).

and the magnet, measured as a function of the superconductor–magnet distance, is shown in Fig. 4. It can be seen that, when interacting with the permanent magnet, the bismuth-containing superconductor with the foam-like microstructure (Fig. 4a) and the yttrium-containing ceramics (Fig. 4b) have practically the same levitation force, although it is known that the maximum levitation force is achieved in single-grain and single-crystal HTSC samples of 1–2–3 superconductors [5]. Thus, despite a relatively low critical current density in
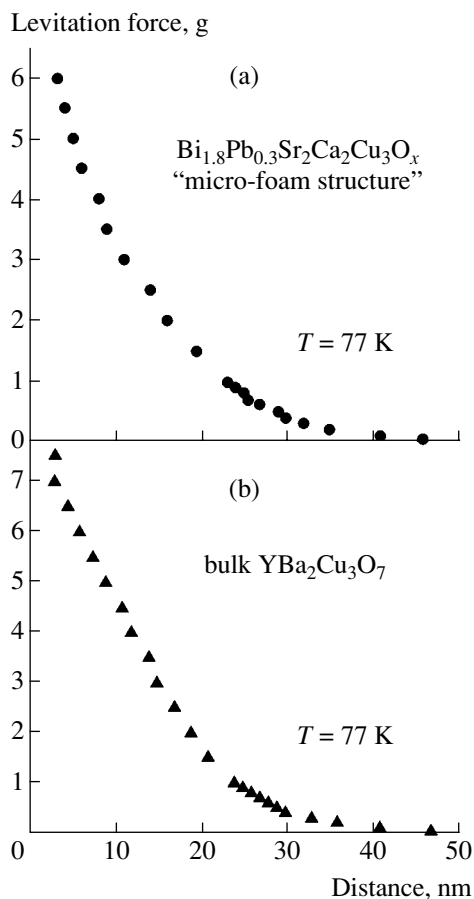
Levitation force, g

Fig. 4. Levitation force as a function of the distance between the Nd–Fe–B magnet and (a) a $Bi_{1.8}Pb_{0.3}Sr_2Ca_2Cu_3O_x$ HTSC pellet with a foam-like microstructure and (b) a $YBa_2Cu_3O_7$ HTSC sample of high density.

our HTSCs with the foam-like structure at the liquid nitrogen temperature (~50 A/cm^2) and a low "filling factor," the levitation force turns out to be sufficiently high due to strong pinning.

ACKNOWLEDGMENTS

REFERENCES

1. E. S. Reddy and G. J. Schmitz, Supercond. Sci. Technol. **15**, L21 (2002).

2. Yu. L. Kuz'min, Pis'ma Zh. Tekh. Fiz. **29** (10), 36 (2003) [Tech. Phys. Lett. **29**, 414 (2003)].

3. V. S. Kravchenko, M. A. Zhuravleva, E. M. Uskov, *et al.*, Neorg. Mater. **34**, 1274 (1998).

4. Y. Ando, J. Takeya, Y. Abe, *et al.*, Phys. Rev. B **62**, 626 (2000).

5. I.-G. Chen, J.-Ch. Hsu, and G. Janm, Chin. J. Phys. (Taipei) **36**, 420 (1998).

Translated by Yu. Vishnyakov

Atomic Relaxation at the Kinks of Steps on the {112} Tungsten Surface

T. I. Mazilova and I. M. Mikhailovskij

Kharkov Institute of Physics and Technology, National Scientific Center, Kharkov, Ukraine

Received May 6, 2003

Abstract—Low-temperature field evaporation from $\langle 111 \rangle$ steps on the {112} tungsten surface has been studied using the field ion microscopy techniques. It is established that the atoms at kinks of the steps exhibit anomalous stability with respect to field evaporation. This effect is related to the relaxation of atoms at the kinks. Using geometric analysis of the ion images, the relaxation displacement component normal to the surface was calculated for atoms at the kinks. © *2003 MAIK "Nauka/Interperiodica".*

In recent years, development of the technology of nanodimensional systems has led to extensive investigation of a fine structure of the surface atomic layers [1, 2]. Subatomic relaxational displacements of the surface atomic layers determine to a considerable extent the equilibrium shape of crystals. Investigations of the surface relaxation phenomena by low-energy electron diffraction (LEED) were mostly performed on flat close-packed crystal faces, whereas vicinal (stepped) surfaces were studied to a much less extent. Difficulties in determining the relaxation state of such surfaces by LEED are caused primarily by a relatively small number of the surface centers capable of scattering electrons. As a result, the structure and relaxation state of only a few vicinal surfaces formed by regular parallel rows of atomic steps have been experimentally studied so far [2, 3].

Experimental data characterizing the atomic relaxation at kinks of the steps are presently not available. However, these very features of the surface morphology control the kinetic processes on real surfaces including the surface self-diffusion and crystal growth. Atoms at the kinks also determine to a considerable extent the electron structure of real surfaces and their physicochemical properties in strong electric fields. In particular, kinks are effective concentrators of electric fields, so that atoms at the kinks account for the main contribution to the formation of images in a field ion microscope.

Field ion microscope (FIM) is the instrument capable, by means of field evaporation, of reproducing the configuration of surface steps with kinks and revealing their fine structure on an atomic resolution level [4, 5]. The local electric field strength determining the brightness and contrast of FIM images significantly depends on the mutual arrangement of atoms at the kinks and on the shape of the effective electron surface. However, information on the atomic displacement component normal to the surface cannot be presently extracted from FIM images because of the absence of calibration data concerning the relaxation of surface atoms at kinks of the surface steps.

Quantitative information about the relaxational displacements of atoms along the normal to the surface can be obtained from an analysis of the surface atomic topography formation in the course of the field evaporation process [6]. In this context, we have studied the kinetics of variation in the local atomic surface topography near kinks of the steps on the {211} tungsten surface. The results show that the atomic morphology of the surface significantly depends on the relaxational displacements of atoms at the kinks.

The study was performed on point samples prepared by means of electropolishing from tungsten of 99.98% purity. The measurements in FIMs were conducted at a residual gas pressure on the order of 10^{-10} Pa, a helium pressure of $\sim 2 \times 10^{-3}$ Pa, and a sample temperature within 40–78 K. The point tip surface was initially cleaned by low-temperature field evaporation. FIM images were interpreted within the framework of a geometric model known to satisfactory reproduce the atomic morphology of the crystal surface formed in the course of field evaporation [4].

Figure 1 presents FIM images of the {211}W face and shows schematically the corresponding arrangement of surface atoms. Here, the sample with a curvature radius of $R = 15$ nm was rounded by field evaporation at 40 K. The {211}W face comprises close-packed $\langle 111 \rangle$ atomic rows spaced by $a\sqrt{2}$. There are two possible geometries of kinks on the steps parallel to the $\langle 111 \rangle$ close-packed atomic chains on the {211}W face, representing kinks of the $(112)[\bar{1}\bar{1}1]$ and $(112)[11\bar{1}]$ types. These kinks are dissimilar because {111} plane is not a mirror-reflection plane. In the notation adopted, the vector $\langle 111 \rangle$ indicates the "step down" direction. Under the conditions studied, the FIM resolution is slightly below 0.27 nm. As a result, the images of separate atoms in close-packed chains partly overlap (Fig. 1c).
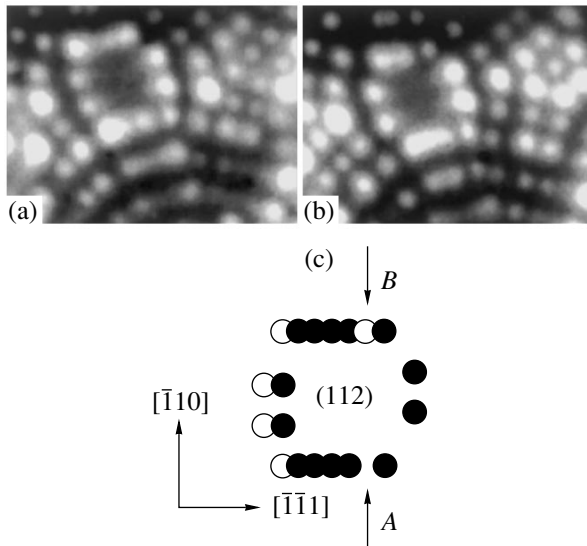
Fig. 1. FIM images (a) before and (b) after field evaporation from steps on the (112)W surface and (c) schematic diagram of the arrangement of surface atoms.

It was found that atoms at the (112)[$\bar{1}\bar{1}$1] kinks are anomalously stable with respect to field evaporation: the evaporation rate of such atoms is 5–7 times lower as compared to that for other atoms on the same $\langle 111 \rangle$ step. After removal of the previous {211} atomic layer, field evaporation from a close-packed chain never begins (as it might be expected based on the general theory of evaporation) at the (112)[$\bar{1}\bar{1}$1] kink: a new stage of the layer-by-layer field evaporation process usually begins with detachment of the next neighbor— the second atom counting from the kink edge. This is manifested by a dark gap on the previously unresolved atomic step. Such a gap is already present in the initial FIM image, as indicated by arrow A in Fig. 1c. Further exposure to the electric field with a strength of 57.5 V/nm led to the regular evaporation of four atoms at the kinks of steps on the (112) face and to anomalous evaporation of the next neighboring atom at the (112)[$\bar{1}\bar{1}$1] kink (indicated by arrow B in Fig. 1c).

In terms of the geometric model, the fact of anomalous field evaporation implies that atoms at the kinks and their nearest neighbors exhibit mutual displacement along the normal to the surface. Small relaxational displacements in the direction perpendicular to the surface, observed for atoms on a step, result in a tangential shift of the evaporation site. This effect is analogous to the so-called indirect magnification phenomenon that is widely used in interpretations of the FIM images of lattice defects [4]. The tangential shift of the coordinate of the evaporation site is minimum, amounting to $a/2\langle 111 \rangle$. In the vicinity of the crystallographic pole of a locally spherical sample, the mutual normal displacement U_z of neighboring atoms at the kink and on the step is $U_z^{ks} = d_{nn}L/2R$, where L is the length of

the step under consideration. In our experiments, the L/R ratio was within 0.075–0.120 and, accordingly, the average value of U_z^{ks} was 0.014 ± 0.005 nm.

An analysis of the arrangement of atoms before and after field evaporation (Figs 1a and 1b, respectively) shows that the appearance of a dark gap on the FIM image of the step is not related to a tangential displacement of end atoms in the (112)[$\bar{1}\bar{1}$1] chain. In these FIM images, the positions of all atoms near the kink remain unchanged. This excludes the possibility that the dark gap has been formed due to a displacement of the end atom of the step along the surface to a position stabilized by the electric field.

The process of relaxation of atoms at the kinks has never been studied by any experimental methods. Recent investigations of the stepped surfaces of fcc metals [3] showed that atomic relaxation on the steps is significantly higher as compared to that on relatively close-packed smooth surfaces. A difference between the relaxed and unrelaxed electron densities leads to an additional potential difference, resulting in displacement of a surface atom inward the metal. This phenomenon is directly related to "smoothening" of the electron surface [7]. The effect has to be more pronounced for the open surface configurations, such as the kinks of steps on a close-packed {211} surface studied in our case.

To summarize, we have observed anomalies in the low-temperature field evaporation from {211}W surface, related to the displacement of atoms at the kinks of steps in the direction of normal to the surface. It was demonstrated that this effect can be used for quantitatively estimating the differential atomic displacements.

REFERENCES

1. K. Swamy, E. Bertel, and I. Vilfan, Surf. Sci. **425**, L369 (1999).
2. S. Kiriukhin, L. Sutcu, and E. H. Conrad, Phys. Rev. B **59**, 6736 (1999).
3. M. Hirsimäki, T. Pitkänen, M. Valden, *et al.*, Surf. Sci. **454–456** (1), 6 (2000).
4. M. K. Miller, A. Cerezo, M. G. Hetherington, and G. D. W. Smith, *Atom-Probe Field Ion Microscopy* (Oxford Univ. Press, Oxford, 1996).
5. A. L. Syvorov, T. L. Razinkova, and A. G. Sokolov, Phys. Status Solidi A **61**, 11 (1980).
6. I. M. Mikhailovskij, G. D. W. Smith, N. Wanderka, and T. I. Mazilova, Ultramicroscopy **95**, 157 (2003).
7. D. L. Adams and C. S. Sorensen, Surf. Sci. **166**, 495 (1986).

Translated by P. Pozdeev

Lasing on the Erbium Atomic Transitions
in an Er–Tm–He Mixture

V. A. Gerasimov* and A. V. Pavlinskii

Institute of the Optics of Atmosphere, Siberian Division, Russian Academy of Sciences, Tomsk, Russia
* e-mail: vag@iao.ru
Received April 4, 2003

Abstract—We report for the first time on the laser radiation generated in erbium vapor, whereby the upper laser level in Er atom is populated due to collisional excitation transfer from the resonance levels of Tm atom. © 2003 MAIK "Nauka/Interperiodica".

The possibility of creating lasers employing the energy exchange between the upper levels of two different atoms was originally pointed out by Petrash [1], who proposed using a mixture of sodium and potassium vapors, but a laser implementing this scheme has not been created so far. We have attempted to realize this idea. For solving this problem, most promising atoms are metals of the lanthanide group possessing a rich structure of atomic levels. This circumstance increases the probability that collisional transfer of the excitation energy between different metal atoms will involve acceptor levels with a small energy difference ($\Delta E < kTg$) relative to the donor level.

For this experiment, we have selected thulium (Tm) and erbium (Er). As is known, a thulium vapor laser [2] has 17 lasing transitions, in 16 of which the upper laser levels are populated due to collisional excitation transfer from close-lying resonance levels with energy differences within $\Delta E = 27$–700 cm^{-1}. This is the first report on laser radiation generated in erbium vapor.

Since the temperatures of equal saturated vapor pressures in thulium and erbium vapors in the region of pressures about 1 Torr differ by ~500 K, the necessary temperature profile in a gas discharge tube (GDT) was provided by an external heater. The GDT was made of alundum and had a diameter of 12 mm and a total active region length of 500 mm. The aliquots of thulium were placed in a 250-mm-long central zone of the GDT, while erbium occupied two 125-mm long zones at the tube ends. The buffer gas was helium at a pressure of 3 Torr. The temperature in the discharge channel was monitored by an optical pyrometer of the "Promin" type.

The pumping source was based on a hydrogen thyratron of the TGI1-1000/25 type featuring direct discharge of a 14-kV storage capacitor with $C_s = 2.35$ nF to the GDT. The pulse repetition rate was 5 kHz. The laser cavity was formed by two plane Al-coated dense mirrors. The laser radiation was extracted through a glass plate arranged in the cavity at an angle of 45° to

the optical axis. The output radiation was monitored using a system comprising a monochromator (MDR-23), a photomultiplier (FEU-62), and oscillographs (S1-75 and Tektronix TDS 3032).

The experiment was carried out as follows. First, the GDT was charged over the entire length with erbium only. The external heater was switched so as to provide for a uniform GDT heating and the possibility of lasing in erbium vapor was studied at an erbium atomic density of up to 5×10^{15} cm^{-3}. However, our attempts to generate laser radiation under these conditions were
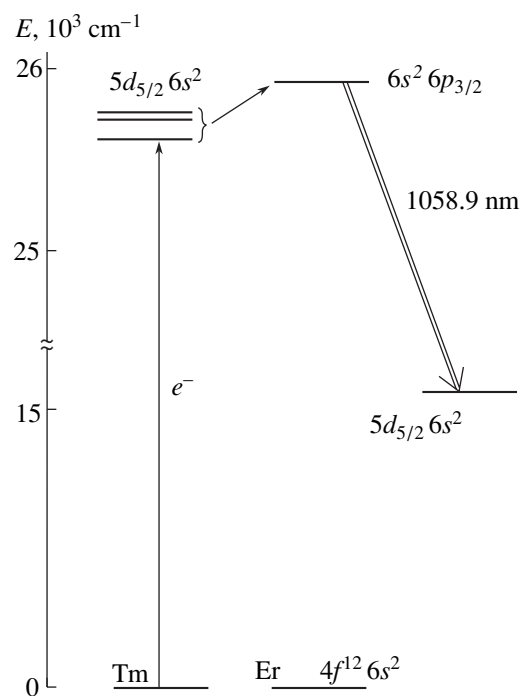
Fig. 1. Schematic diagram illustrating population of the upper laser level in erbium atom. The double arrow indicates the lasing transition.
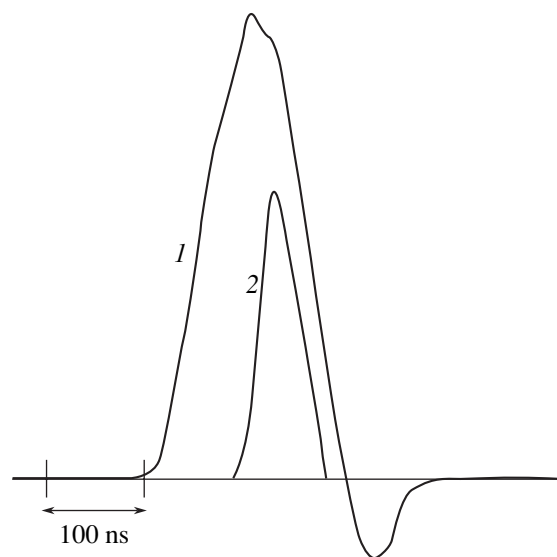
Fig. 2. Oscillograms of the (*1*) current and (*2*) laser radiation pulses.

unsuccessful. Then, thulium was placed in the central zone as described above, while erbium was placed at the tube ends. The external heater maintained a temperature of 1100°C in the central zone (that corresponded to the density of thulium atoms $n_{Tm} = 5 \times 10^{15}$ cm^{-3}) and 1530°C in the end zones (the corresponding density of erbium atoms being $n_{Er} = 2.7 \times 10^{15}$ cm^{-3}).

The results of our experiments showed the generation of four emission lines corresponding to thulium atoms (with the wavelengths of $\lambda = 1069, 1101, 1310,$ and 1338 nm) and one more line with $\lambda = 1058.9$ nm, which did not belong to thulium and was observed only in the presence of erbium vapor.

An analysis of the published data [3–5] showed that the observed line belongs to the atomic transition in erbium between a level of the configuration $4f^{11}(^4I^0_{13/2})6s^26p_{3/2}$ with an energy of 25942.577 cm^{-1} and a level of the configuration $4f^{11}(^4I^0_{13/2})5d_{5/2}6s^2$ with

an energy of 16501.416 cm^{-1}. The upper laser level attributed to erbium has the same parity as the ground level. Figure 1 shows the proposed scheme of occupation for this upper level. Apparently, the upper laser level is populated from three resonance levels of thulium with the energies $E = 25745, 25717,$ and 25656 cm^{-1} via the reaction of collisional excitation transfer,

$$\text{Tm}^* + \text{Er}_0 \longrightarrow \text{Tm}_0 + \text{Er}^* \pm \Delta E,$$
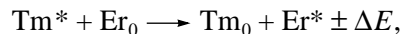
where Tm_0, Tm^*, Er_0, and Er^* are the atoms of thulium and erbium in the ground and excited states, respectively.

The efficiency of this lasing process is determined by the following factors: (i) relatively small energy differences, $\Delta E = 200$–300 cm^{-1}; (ii) a high rate of population of the indicated resonance levels from the ground state by electron impact in the gas discharge. The laser pulse position, corresponding to the trailing front of the pumping pulse (Fig. 2), indicates that the upper laser level is populated via collisions with heavy (metal) atoms [2].

Thus, we have realized an original scheme of pumping with the excitation transfer between atoms of different components of the active medium.

REFERENCES

1. G. G. Petrash, Izv. Akad. Nauk SSSR, Ser. Fiz. **42**, 2507 (1978).

2. V. A. Gerasimov and B. N. Yunzhakov, Kvantovaya Élektron. (Moscow) **16**, 2386 (1989).

3. N. Spector and S. Held, *The First Spectrum of Erbium: Description and Classification* (Israel Atomic Energy Commission, Soreq, 1980).

4. P. Gamus, G. Guelachvili, and J. Verges, Spectrochim. Acta B **24**, 373 (1969).

5. J. Sugar and W. F. Meggers, J. Res. Natl. Bur. Stand., Sect. A **77**, 1 (1973).

Translated by P. Pozdeev

Impact-Ionization Autosolitons in Silicon with Deep Impurity Levels

A. M. Musaev

Institute of Physics, Dagestan Scientific Center, Russian Academy of Sciences, Makhachkala, Dagestan, Russia
e-mail: akhmed-musaev@yandex.ru
Received May 6, 2003

Abstract—Autosolitons with the charge carriers self-reproduced by impact ionization of the deep acceptor levels of indium in silicon in a strong electric field at 77 K have been experimentally detected and studied. A model describing the excitation of such impact-ionization autosolitons is proposed, in which the activating factor is the free charge carrier density and the inhibiting factor is the carrier temperature. The existence of such autosolitons is determined by the condition that the region of high carrier density at the autosoliton center does not expand because the outdiffusion of carriers is equilibrated by their supply through thermodiffusion. © *2003 MAIK "Nauka/Interperiodica".*

Semiconductors and semiconductor structures are the most convenient model systems with an active kinetic medium (nonequilibrium electron–hole plasma) for investigation of the mechanisms of formation and evolution of spatially isolated (solitary) dissipative structures—autosolitons [1]. Autosolitons of the ionization nature have been experimentally studied in [2–4]. It was demonstrated [2] that the electron–hole plasma generated by impact ionization in *n*-GaAs films exhibits separation into current columns (high-density plasma) and electric field striations (low-density plasma). Autosolitons of the spike type excited by localized light pulses were detected in silicon *p–i–n* structures [3]. Pulsed autosolitons with the charge carriers self-reproduced by impact ionization of excitons in a strong electric field were studied in silicon [4].

This Letter reports the results of experimental detection and investigation of autosolitons with the charge carriers self-reproduced by impact ionization of the deep acceptor levels of indium ($\varepsilon_h = 0.16$ eV) in silicon in a strong electric field at 77 K.

The investigation was performed on the samples of compensated *p*-Si⟨In⟩ with an impurity concentration of $N_A - N_D = 6.0 \times 10^{12}$ cm^{-3}. The sampled had the shape of rectangular plates of dimensions $5.4 \times 1.8 \times 0.4$ mm with the large (5.4×1.8 mm) face oriented perpendicular to the [111] direction. The antiblocking ($p^+–p$) contacts were created by depositing and fusing aluminum (or aluminum foil) into the large faces. These contacts exclude the influence of the transition contact characteristics on the current kinetics during charge carrier generation–recombination processes in the bulk [5]. A necessary condition is that $\tau < \tau_t$ (τ and τ_t are the characteristic time of the generation–recombination process development and the carrier flight through the sample, respectively). In order to exclude the surface effects, the contacts were applied onto the opposite sample faces with 0.25-mm-wide edge margins. The dynamical current–voltage characteristics were studied by applying single saw-tooth-shaped pulses of various slope in the regime of voltage generator. The current instability development was studied by applying rectangular pulses with a duration of up to 50 μs. Inhomogeneous current density distribution in the sample was studied using a sectioned cathode contact.

At low temperatures, the main mechanism responsible for an increase in the conductivity of silicon with deep impurity levels in a strong electric field is the impact ionization observed at an electric field strength of 10^3–10^4 V/cm [5]. In addition to this, there are several other mechanisms also capable of increasing the charge carrier density in response to increasing field strength. These are the injection of minority carriers and the generation of majority carriers in the case of a space-charge-limited current. Another important factor is an increase in the hole density during thermal-field carrier production, which also grows with the field strength (the Poole–Frenkel effect). In this case, the electric field changes the maximum energy barrier height by

$$\Delta\varepsilon = -e(eE/\pi\varepsilon)^{1/2}, \tag{1}$$

where E is the electric field strength and ε is the dielectric permittivity of silicon. Dependence of the thermal-field carrier generation rate on the electric field strength is described by an exponential function of the quantity $\Delta\varepsilon/kT_0$. In the case of an attractive center under consideration, this quantity can be expressed as follows [5]:

$$\Delta\varepsilon/kT_0 = -0.84(E/10^4)^{1/2}(300 \text{ K}/T_0), \tag{2}$$

where T_0 is the lattice temperature.
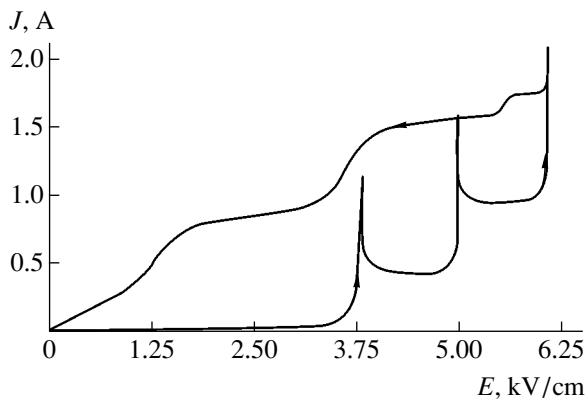
Fig. 1. Dynamical current–voltage characteristic of the sample (arrows indicate the forward and reverse branches).
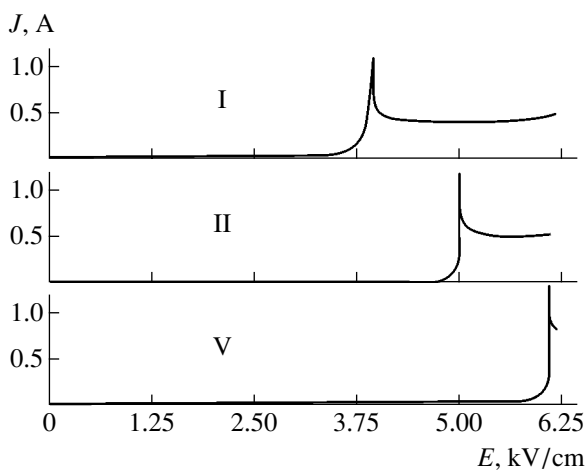
Fig. 2. Dynamical current–voltage characteristics (I, II, V) measured using various parts of a sectioned cathode contact.

An analysis of the character of the charge carrier density variation at various rates of increase of the electric field strength showed that the Poole–Frenkel effect is insignificant when the applied voltage grows at a rate of not less than 40 V/μs. This is related to the fact that the sample temperature cannot significantly increase within a short time under adiabatic conditions; at the same time, the role of this effect grows with the liberated Joule's power. The main mechanism accounting for an increase in the majority carrier density in this case is the impact ionization of impurities. At a field strength sufficient for the effective impact ionization, the density of free carriers is determined by a balance between the rates of trapping, impact ionization, and thermal-field generation.

Figure 1 shows the typical dynamical current–voltage characteristic measured at a ramp voltage slope of 50 V/μs. A characteristic feature of this curve is that an increase in the applied voltage is accompanied by current spikes formed in a threshold manner. The number

of current spikes in the system increases with the electric field strength. Investigation of the current–voltage characteristics in various regions of the sample (using a sectioned cathode contact) showed that the threshold-like current spikes arise in various regions of the sample (Fig. 2), despite being quite similar in shape and electrical characteristics.

As the ramp voltage slope decreases, the current–voltage characteristics exhibit a change. The impurity ionization voltage drops and the $J(E)$ curve exhibits no sharp features, which is explained by Joule's heating of the lattice and by thermal-field ionization of impurities. This suggests that, as the lattice temperature increases, the regime of impact ionization is replaced by the thermal-field ionization. This factor may also explain the shape of the reverse current–voltage characteristics exhibiting a hysteresis when the electric field strength is decreased. The results of these measurements showed that the higher the power of ionization losses, the lower voltages correspond to a drop in the hole density. At an electric field strength below the impact ionization threshold, the role of the Poole–Frenkel effect is still significant but not as large. As was demonstrated in [6], the hole density at low temperatures in indium-doped silicon increased no more than three times when the electric field strength was increased from 10^2 to 4×10^3 V/cm.

The decay of current in the regions of ionization during the field growth is explained by the scattering of holes on phonons and by a decrease in the carrier mobility due to Joule's heating of the ionization region. In silicon exposed to an electric field at $T > 77$ K, a dominating factor is the scattering on the acoustic-strain and optical potentials, whereby the carrier mobility decreases with increasing field strength. This is confirmed by the temperature dependence of the conductivity measured at various values of the applied field strength.

The above results can be consistently interpreted based on the model of a static autosoliton with local self-reproduction of charge carriers [1]. The autosolitons can be spontaneously excited on inhomogeneities in the impurity distribution or on some other inhomogeneities leading to the impact ionization in local regions. According to this plasma separation mechanism, the activating factor is the free charge carrier density (p), while the inhibiting factor is the carrier temperature. The positive feedback with respect to the activator is related to increasing dependence of the rate of ionization of the deep impurity levels, since the ionization rate is a sharply increasing function of the carrier density. The damping role of the inhibitor is related to a decrease in the charge carrier temperature during their scattering on phonons, which limits the impact ionization rate. An increase in the temperature in the regions

of lattice autosolitons additionally decreases the charge carrier energy.

Distributions of the density and the energy flux of carriers for autosolitons in the system studied are described by the diffusion equations. In the model under consideration, a bifurcation parameter is the electric field strength, $\alpha = \tau_p/\tau_T \ll 1$, and the ratio $\varepsilon = l/L$ can be either greater or smaller than unity, depending on the system parameters (τ_p and l are the characteristic time and length of the carrier density variations, respectively; τ_T and L are the characteristic time and length of variations in the average temperature of the charge carriers).

REFERENCES

1. B. S. Kerner and V. V. Osipov, *Autosolitons* (Nauka, Moscow, 1991).

2. B. S. Kerner and V. F. Sinkevich, Pis'ma Zh. Éksp. Teor. Fiz. **36**, 359 (1982) [JETP Lett. **36**, 436 (1982)].

3. V. N. Vashchenko, B. S. Kerner, V. V. Osipov, and V. F. Sinkevich, Fiz. Tekh. Poluprovodn. (Leningrad) **24**, 1705 (1990) [Sov. Phys. Semicond. **24**, 1065 (1990)].

4. A. M. Musaev, Fiz. Tekh. Poluprovodn. (St. Petersburg) **33**, 1183 (1999) [Semiconductors **33**, 1076 (1999)].

5. A. G. Milnes, *Deep Impurities in Semiconductors* (Wiley, New York, 1973; Mir, Moscow, 1977).

6. A. E. McCombs, Int. J. Electron. **32**, 361 (1972).

Translated by P. Pozdeev

Dynamical Properties of Nematic Liquid Crystal Solutions in Pulsed Magnetic Fields

D. L. Bogdanov, É. V. Gevorkyan, A. A. Romanov, and M. V. Shevchuk*

Moscow State Regional University, Moscow oblast, Russia
* e-mail: shevchukmv@rambler.ru
Received April 25, 2003

Abstract—Behavior of the rotational viscosity coefficient of a nematic liquid crystal of the N8 type and its solution in a nonmesogenic solvent (benzene) has been studied under the conditions of variable thermodynamic state parameters (p, T). © 2003 MAIK "Nauka/Interperiodica".

Investigations of the dissipative properties of liquid crystals (LCs) and their solutions in the region of existence of a mesophase are of interest from the standpoint of both basic and applied research. While the molecular-kinetic, thermodynamic, hydrodynamic, and other physicochemical properties of various LCs have been rather exhaustively studied and extensively reported in the literature, the number of publications devoted to LC solutions is very restricted.

Below we present the results of experimental measurements of the ratio of the rotational viscosity coefficient to the diamagnetic susceptibility ($\gamma_1/\Delta\chi$) for a nematic liquid crystal (NLC) of the N8 type and a solution of this liquid crystal in benzene (N8–C_6H_6, 7 : 1, w/w) in a temperature interval from 292 to 343 K at pressures of up to 110 MPa. The N8 liquid crystal composition represents a eutectic 2 : 1 (w/w) mixture of H-1-*n*-*p*-methoxybenzylidene-*p*-butylaniline (MBBA) and H-3-*n*-*p*-ethoxybenzylidene-*p*-butylaniline (EBBA) components.

The thermodynamic properties of N8 have been quite exhaustively studied [1, 2]. This NLC has a broad temperature interval of existence of a mesophase (from 263 to 326 K at atmospheric pressure). According to the optical data, adding a nonmesogenic solvent to N8 leads to a decrease in the temperature of the phase transition from NLC to an isotropic liquid.

The regions of existence of a mesophase for both N8 and its solution under pressure were determined from the experimentally measured values of acoustic parameters. In the pressure range studied, the behavior of the NLC–isotropic liquid transition temperature $T_c(P)$ for both pure N8 and its benzene solution can be quite adequately described by the linear relation

$$T_c(P) = T_c + \frac{dT}{dP}P, \tag{1}$$

where $dT/dP = 0.29$ K/MPa.

Under the action of an external magnetic field, NLCs acquire an ordered oriented structure. In initially unoriented relatively large ($l \geq 10^{-3}$ m) NLC samples with dimensions exceeding the magnetic coherence length, application of a magnetic field leads to reorientation of the LC director **n** along the field. This motion of the director is hindered by the presence of viscosity and defects, but with time the director is aligned in the field direction and the NLC acquires a monodomain structure.

The relation between a change in the coefficient of ultrasound absorption in an applied magnetic field and the LC director orientation in the nematic phase is as follows [4]:

$$\frac{\alpha_\parallel(t)}{f^2} = c^* + a\frac{1 - \sqrt{\dfrac{e^-}{1-e^-}}\arccos\sqrt{e^-}}{1-e^-}$$
$$+ b\frac{1 + \dfrac{e^-}{2} - \dfrac{3}{2}\sqrt{\dfrac{e^-}{1-e^-}}\arccos\sqrt{e^-}}{\left(1-e^-\right)^2}, \tag{2}$$

where $e^- = \exp[-2t/\tau_n]$; $\tau_n = 2/\omega_0$ is the director relaxation time; and c^*, a, and b are the parameters of angular dependence of the absorption coefficient (per square frequency). The value of this parameter is $\alpha_\parallel/f^2 = c^* + a + b$ for an NLC oriented along the wave vector, and $\alpha_0/f^2 = c^* + 1/3a + 1/5b$ for an unoriented NLC.

The measurements were performed using a fixed-distance pulse technique described in [3]. The experimental time variation of the $\alpha_\parallel/f^2$ value (Fig. 1) correspond to a model underlying formula (2). Using the relaxation times τ_n calculated from these data ($\tau_n = \gamma_1/\Delta\chi\mu_0H^2$), we determined the $\gamma_1/\Delta\chi$ ratios for various values of the state parameters (P, T). The results of
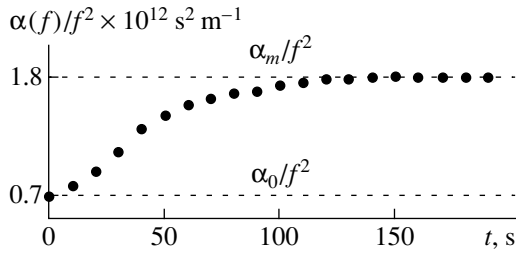
Fig. 1. Time variation of $\alpha_\parallel(t)/f^2$ for N8 at $B = 0.052$ T, $P = 0.1$ MPa, $T = 315$ K, and $f = 6.5$ MHz.
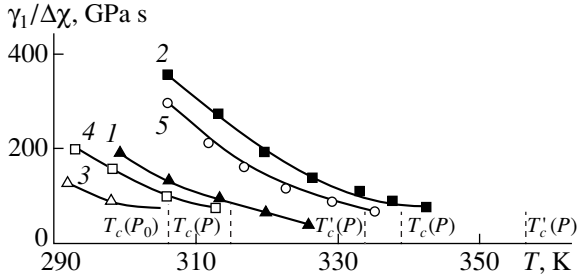
Fig. 2. The plots of $\gamma_1/\Delta\chi$ versus temperature for N8 at $P = 30$ (*1*) and 110 MPa (*2*) and for the N8 solution in benzene at $P = 0.1$ (*3*), 30 (*4*), and 110 MPa (*5*).

these calculations for some pressures and temperatures are presented in Fig. 2. The temperature dependences of the $\gamma_1/\Delta\chi$ ratio at various pressures are exponential,

$$\frac{\gamma_1}{\Delta\chi} = A \exp\frac{E}{RT}, \qquad (3)$$

where A is the constant factor representing the individual characteristic of a given NLC (for N8 and its solution, this quantity is independent of the pressure and

The activation energies for N8 and its benzene solution at various pressures

P, MPa	N8 E, kJ/mol	N8 solution E, kJ/mol
0.1	35.8	–
10	36.1	–
30	36.8	38.3
50	37.4	38.8
70	38.1	39.5
90	38.8	40.1
110	39.4	40.8

temperature), E is the molar activation energy, and R is the universal gas constant. The values of activation energies for N8 and its benzene solution at various pressures are given in the table.

The activation energy can be represented as a linear function of the pressure, $E = E_0 + dE/dP(p - p_0)$, where $E_0 = E(p_0)$ is the activation energy at normal pressure and dE/dP is the activation volume. In the interval of temperatures and pressures studied, the latter parameter for N8 and its solution is 33 and 32 cm^3/mol, respectively, which amounts to approximately 11% of the molar volume.

A successful semiphenomenological theory of the rotational viscosity has been developed by Diogo and Martins [5] based on the Mayer–Saupe mean field approximation. This theory gives the following expression for γ_1:

$$\gamma_1 = qS^2\exp\left(\frac{\varepsilon S}{kT} + \frac{\theta S^2}{T - T^*}\right), \qquad (4)$$

where q and θ are constant coefficients; $S = \langle 3/2\cos^2\psi - 1/2\rangle$ is the Tsvetkov orientational order parameter (degree of orientation); and T^* is the temperature of "freezing" of the director rotation. In formula (4), the product qS^2 corresponds to quantity $A\Delta\chi$ in our notations. Since A is constant for a given NLC, the degree of orientation far from the phase transition is $S \sim \Delta\chi$. The temperature dependence of γ_1 is determined by two exponential terms containing three fitting parameters (ε, θ, and T^*), which cannot be determined in independent ways.

REFERENCES

1. D. L. Bogdanov, *Acoustical Methods for Investigation of the Alignment of Liquid Crystals in Variable Fields* (Vses. Zaochn. Mashinostr. Inst., Moscow, 1980).

2. A. N. Zuev, Candidate's Dissertation (Moscow, 1992).

3. D. L. Bogdanov, A. V. Osipov, *et al.*, *Supersound and Thermodynamic Properties of Materials* (Kursk, 1997), pp. 109–115.

4. E. V. Gevorkyan, *Ultra-Acoustics: Application to Material Studies* (Vses. Zaochn. Mashinostr. Inst., Moscow, 1980), Issue 32, pp. 48–58.

5. A. C. Diogo and A. F. Martins, Mol. Cryst. Liq. Cryst. **66**, 133 (1981).

Translated by P. Pozdeev

Chaos Control in an Electron Beam with Supercritical Current in a Hydrodynamical Model of the Pierce Diode

A. A. Koronovskiĭ, I. S. Rempen, and A. E. Khramov*

Saratov State University, Saratov, Russia
* e-mail: aeh@cas.ssu.runnet.ru
Received May 27, 2003

Abstract—The possibility of a continuous feedback control of chaos in an electron beam with supercritical current is considered within the framework of a hydrodynamical model of the Pierce diode. A method for controlling chaotic dynamics through stabilization of an unstable equilibrium state in a distributed active medium is proposed. © *2003 MAIK "Nauka/Interperiodica".*

The Pierce diode [1, 2] is one of the simplest electron beam–plasma systems possessing a complicated chaotic dynamics [2–6]. This device comprises two infinite plane-parallel grids, spaced by a distance L_0, penetrated by an initially monoenergetic electron beam. The grids bounding the system are grounded; the beam charge density ρ_0 and velocity v_0 at the system input are maintained constant. The space between grids is filled by a homogeneous neutralizing background of immobile ions with a charge density $|\rho_i/\rho_0| = 1$. The system dynamics is determined by the only control parameter $\alpha = \omega_p L/v_0$, called the Pierce parameter (ω_p is the plasma frequency of the electron beam).

As is known, instabilities arise in the Pierce diode at $\alpha > \pi$ [1–3]. In this case, a virtual cathode is formed in the system that reflects a part of the electron beam back toward the plane of injection. However, a complete transmission of the electron beam is possible for $\alpha \sim 3\pi$ [2]. In this case, the growth of the Pierce instability is restricted to the appearance of a nonlinearity, the diode operates in the complete beam transmission regime, and the electron beam with supercritical current in the flight gap can be described within the framework of a hydrodynamical approach.

Previously [2, 4–6], complicated dynamics of the electron beam in the Pierce diode was studied using the hydrodynamical model. In particular, it was found that, as the Pierce parameter decreases in the interval $\alpha \in (2.85, 2.90)$, the system exhibits a cascade of period doubling bifurcations leading eventually to the establishment of a regime of developed chaotic oscillations [2, 4, 5]. It was very interesting to study the possibility of controlling the chaotic oscillatory regimes in the electron beam with supercritical current in the Pierce diode [7–9].

We propose an effective means of controlling the chaotic dynamics of a distributed autooscillatory system (the Pierce diode) based on stabilization of unstable equilibrium states by introducing a continuous

delay feedback into the system. Use of such schemes for the control of chaos has been extensively studied in the case of nonlinear systems with a small number of degrees of freedom [10–14]. Much less attention has been devoted to the control of chaos and the stabilization of unstable equilibrium states in distributed systems. The schemes proposed for stabilization of a spatiotemporal chaos in distributed active media are very difficult to implement in practice (see, e.g., [15, 16]), which is a significant disadvantage hindering experimental investigations into the control of chaotic dynamics in electron beam–plasma systems.

A continuous feedback control scheme proposed in this paper for application to a distributed autooscillatory beam–plasma system possesses several advantages over the classical schemes of chaos control based on the rapid variation of the control parameter (the Ott–Grebogi–Yorke algorithm [10]). First, because rapid determination and change of the control parameter is impossible at ultrahigh frequencies. Another important factor is the distributed character of the system, which does not allow any parameter to be rapidly varied over the entire system length.

Within the framework of the hydrodynamical approximation, the electron beam dynamics in the Pierce diode is described by a self-consistent system including the equation of motion, the equation of continuity, and the Poisson equation in dimensionless variables [2]

$$\frac{\partial v}{\partial t} + v\frac{\partial v}{\partial x} = -\frac{\partial \varphi}{\partial x}, \quad \frac{\partial \rho}{\partial t} + v\frac{\partial \rho}{\partial x} + \rho\frac{\partial v}{\partial x} = 0,$$

$$\frac{\partial^2 \varphi}{\partial x^2} = \alpha^2(\rho - 1), \tag{1}$$

with the boundary conditions $v(0, t) = 1$, $\rho(0, t) = 1$, $\varphi(0, t) = \varphi(1, t) = 0$. Equations (1) for the hydrodynamical theory of the Pierce diode are written in the dimen-
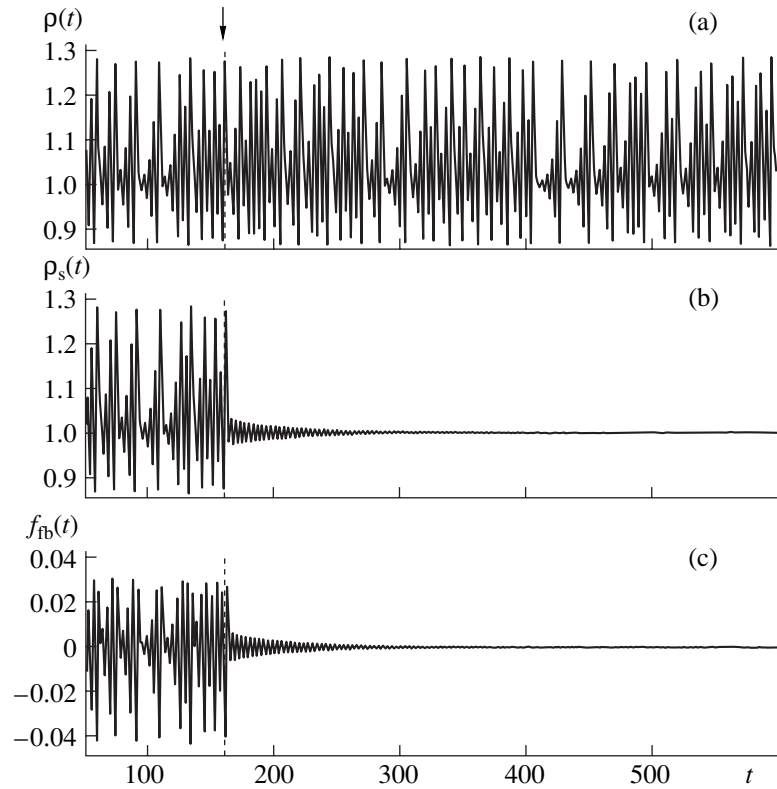
Fig. 1. Time series of (a, b) the space charge density oscillations in a regime of chaotic oscillations ($\alpha = 2.857\pi$) in a nonstabilized system and in the same system stabilized by a feedback circuit, respectively, and (c) the control signal $f_{\text{fb}}(t)$ in the continuous feedback circuit. The arrow and dashed line indicate the moment of feedback switching.

sionless variables of the space charge field potential φ, charge density ρ, electron beam velocity v, spatial coordinate x, and time t, which are related to the corresponding dimensional (primed) variables as $\varphi' = (v_0^2/\eta)\varphi$, $\rho' = \rho_0\rho$, $v' = v_0 v$, $x' = Lx$, and $t' = (L/v_0)t$ (η is the specific charge of electron).

System (1) possesses an unstable homogeneous equilibrium state corresponding to the following distributions: $\bar{v}(x) = 1.0$, $\bar{\rho}(x) = 1.0$, $\bar{\varphi}(x) = 0.0$. In order to stabilize the unstable equilibrium state in the regime of chaotic dynamics, we have used the following scheme of control of the spatiotemporal chaos by means of a continuous external feedback. The continuous feedback was provided by changing the potential at the right-hand boundary of the system:

$$\varphi(x = 1.0, t) = f_{\text{fb}}(t) = K(\rho(x_{\text{fix}}, t) - \rho(x_{\text{fix}}, t - d)),\quad(2)$$

where K is the feedback coefficient and d is the feedback delay. In relation (2), the quantity $\rho(x_{\text{fix}}, t)$ represents oscillations in the space charge density at a fixed point $x = 0.2L$. When the regime of stabilization of the unstable state is established and the system occurs precisely in the unstable state, the feedback signal f_{fb} is comparable to the background noise level.

Figure 1 illustrates the control of chaos (by stabilization of an unstable equilibrium state in the regime of developed chaotic oscillations) in a distributed autooscillatory beam–plasma system (1) by means of the scheme with continuous feedback (2) described above. The figure shows time series of the space charge density in a nonstabilized system without feedback, $\rho(x_{\text{fix}}, t)$, and in the same system upon switching on the feedback, $\rho_s(x_{\text{fix}}, t)$, and the control signal $f_{\text{fb}}(t)$ in the continuous feedback system with the parameters $K = 0.8$ and $d = 0.15$. The arrow and the dashed line indicate the moment of the feedback switching. Prior to this moment, the system exhibits chaotic oscillations of considerable amplitude. Switching on the feedback in the distributed system leads to a rapid decrease in the amplitude of these oscillations and to stabilization of an unstable equilibrium state. After a short transient process, the control signal in the feedback system becomes very small (below 0.01%) as compared to the signal observed prior to stabilization. This implies that the proposed system demonstrates the control of chaos (stabilization of an unstable equilibrium state) by means of feedback with very small control signal amplitude.

An important point is to determine the region of feedback parameters K and d, in which chaos in a given beam–plasma system can be controlled. This region is
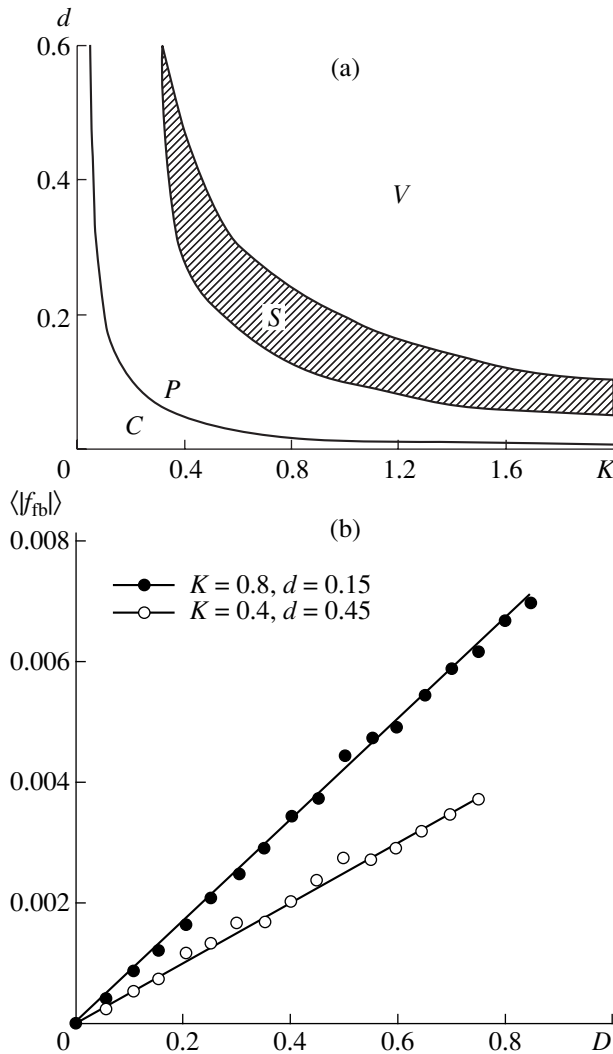
Fig. 2. (a) The map of oscillation regimes on the plane of control parameters (K, d) for a distributed system in the regime of chaotic oscillations ($\alpha = 2.857\pi$) stabilized by an external continuous feedback (cross-hatched region corresponds to stabilization of an unstable equilibrium state); (b) plots of the average feedback signal amplitude $\langle |f_{\mathrm{fb}}(t)| \rangle$ versus noise amplitude D for two sets of the feedback circuit parameters.

shown in Fig. 2a for the regime of developed chaotic oscillations ($\alpha = 2.857\pi$). As can be seen from this map, small values of the feedback coefficient K allow the system to perform chaotic oscillations analogous to those observed in the system without feedback (region C). When the K value increases, the chaotic oscillations are broken and periodic autooscillations are established (region P). However, the control signal is not small and this dynamical regime cannot be considered as the control of chaos. Indeed, the amplitude of oscillations in the feedback circuit f_{fb} in this regime is on the same order of magnitude as that before switching the feedback.

As the coefficient K grows further, a regime of controlled chaos is established (region S), whereby an unstable equilibrium state is stabilized and the system behaves as illustrated in Fig. 1. The width of the chaos control region S (Fig. 2a) strongly depends on the delay parameter d. There are threshold delay values d_1 and d_2, so that stabilization of an unstable equilibrium state is possible only within the interval $d \in (d_1, d_2)$. For the greater values of d and K, reflection of electrons from a virtual cathode in the beam takes place (region V). In this region, the initial equations of the hydrodynamical theory of the Pierce diode fail to be valid [2].

Another question is related to the possibility of stabilization of an unstable equilibrium state in the system in the presence of fluctuations. In order to study the influence of fluctuations on the control of chaos, let us phenomenologically replace the equation of motion in system (1) by a stochastic differential equation with a distributed source of white noise:

$$\frac{\partial v}{\partial t} + v\frac{\partial v}{\partial x} = -\frac{\partial \varphi}{\partial x} + D\xi(x, t), \qquad (3)$$

where $\langle \xi(x, t) \rangle = 0$, $\langle \xi(x, t)\xi(x', t') \rangle = \delta(x - x')\delta(t - t')$ and D is the white noise amplitude.

Figure 2b shows plots of the average feedback signal amplitude $\langle |f_{\mathrm{fb}}(t)| \rangle$ versus noise amplitude D for two sets of the feedback coefficient K and delay time d (angle brackets denote time average). These plots were constructed for a regime of developed chaotic oscillations corresponding to the Pierce parameter $\alpha = 2.857\pi$. The control feedback signal drives the system to the required stabilized state even in the presence of a significant noise with an amplitude comparable with that of the signal $\rho(x_{\mathrm{fix}}, t)$. The noise leads to an increase in the control signal amplitude $\langle |f_{\mathrm{fb}}(t)| \rangle$ in the feedback circuit and to the appearance of fluctuations about the equilibrium state (with an amplitude on the order of D). As can be seen from Fig. 2b, the control signal amplitude $\langle |f_{\mathrm{fb}}(t)| \rangle$ in the feedback circuit linearly increases with the noise amplitude D, the slope being proportional to the feedback coefficient K. The value of delay in the circuit of continuous stabilizing feedback influences the $\langle |f_{\mathrm{fb}}(t)| \rangle$ value rather weakly.

To summarize, we have proposed using a continuous feedback circuit for controlling chaos in a distributed active medium with supercritical current described by a hydrodynamical model of the Pierce diode. According to this method, an unstable equilibrium state in the distributed system is stabilized by an external delay feedback circuit that requires only a very small perturbation to provide for the stabilization.

REFERENCES

1. J. Pierce, J. Appl. Phys. **15**, 721 (1944).

2. D. I. Trubetskov and A. E. Khramov, *Lectures on Microwave Electronics for Physicists* (Fizmatlit, Moscow, 2003), Vol. 1.

3. M. V. Kuzelev and A. A. Rukhadze, *Electrodynamics of Dense Electron Beams in a Plasma* (Nauka, Moscow, 1990).

4. B. B. Godfrey, Phys. Fluids **30**, 1553 (1987).

5. V. G. Anfinogentov and D. I. Trubetskov, Radiotekh. Élektron. (Moscow) **37**, 2251 (1992).

6. H. Matsumoto and H. Yokoyama, Phys. Plasmas **3**, 177 (1996).

7. I. S. Rempen and A. E. Khramov, Izv. Ross. Akad. Nauk, Ser. Fiz. **65**, 1689 (2001).

8. A. E. Khramov and I. S. Rempen, Radiotekh. Élektron. (Moscow) **47**, 732 (2002).

9. H. Friedel, R. Grauer, and K. H. Spatchek, Phys. Plasmas **5**, 3187 (1998).

10. E. Ott, C. Grebogi, and J. A. Yorke, Phys. Rev. Lett. **64**, 1196 (1990).

11. K. Pyragas, Phys. Lett. A **181**, 203 (1992).

12. Y. H. Chen and M. Y. Chou, Phys. Rev. E **50**, 2331 (1994).

13. S. Kaart, J. C. Schouten, and C. M. van der Bleek, Phys. Rev. E **59**, 5303 (1999).

14. Y. C. Kouomou and P. Woafo, Phys. Rev. E **66**, 036205 (2002).

15. Hu Gang and Q. Zhilin, Phys. Rev. Lett. **72**, 68 (1994).

16. S. Boccaletti, J. Bragard, and F. T. Arecchi, Phys. Rev. E **59**, 6574 (1999).

17. G. Benettin, L. Galgani, and J. M. Strelcyn, Phys. Rev. A **14**, 2338 (1976).

Translated by P. Pozdeev